# Fizyka Procesów Klimatycznych
# Wykład 11 – Aktualne zmiany klimatu: atmosfera, hydrosfera, kriosfera

prof. dr hab. Szymon Malinowski
Instytut Geofizyki, Wydział Fizyki
Uniwersytet Warszawski
malina@igf.fuw.edu.pl

dr hab. Krzysztof Markowicz
Instytut Geofizyki, Wydział Fizyki
Uniwersytet Warszawski
kmark@igf.fuw.edu.pl


Badania klimatu
monitoring zmienności
wymuszanie
odpowiedz
konsekwencje
predykcja

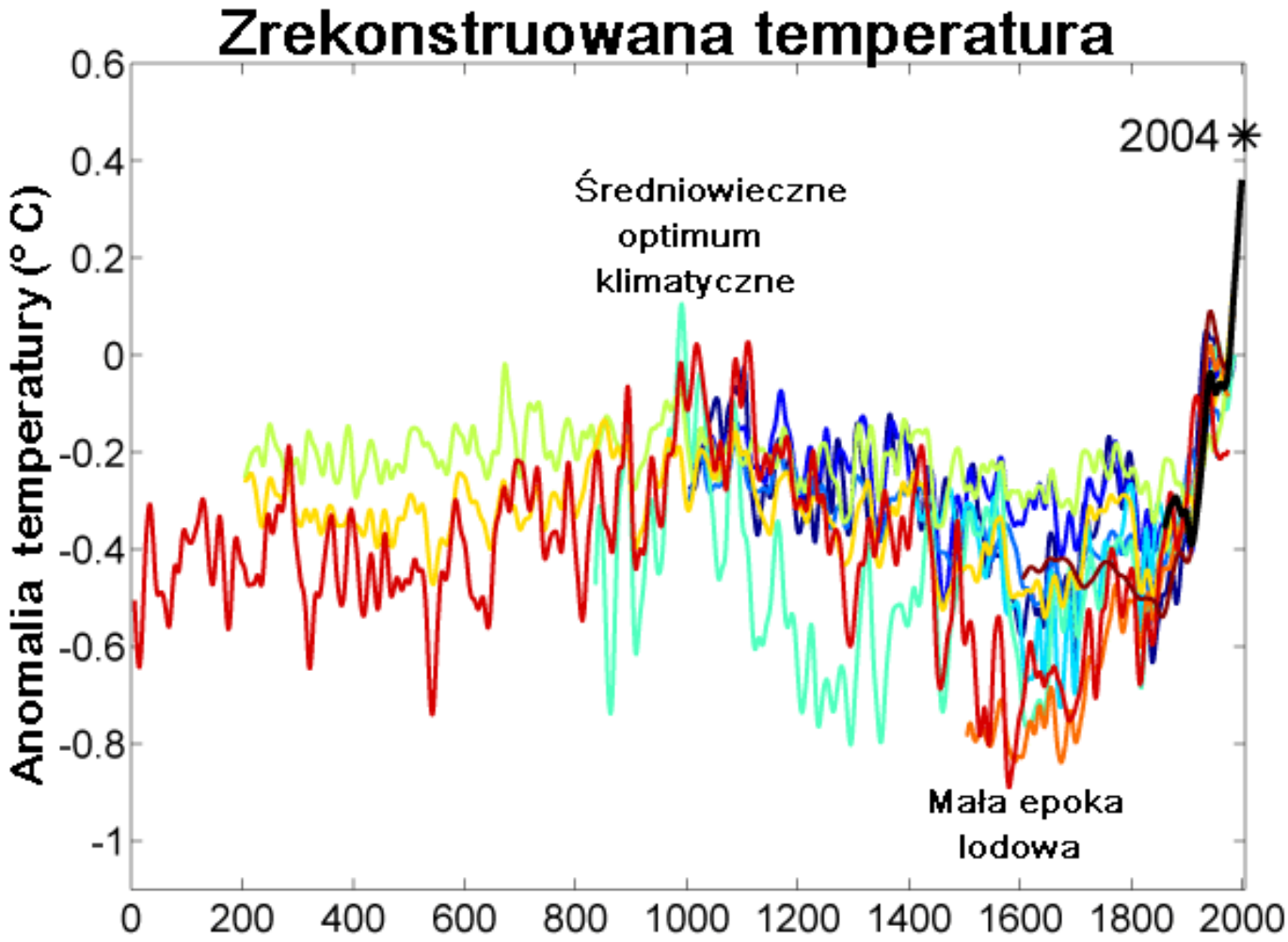


Na postawie 10-ciu rekonstrukcji opublikowanych w latach 1998-2005

# Zmiany klimatu

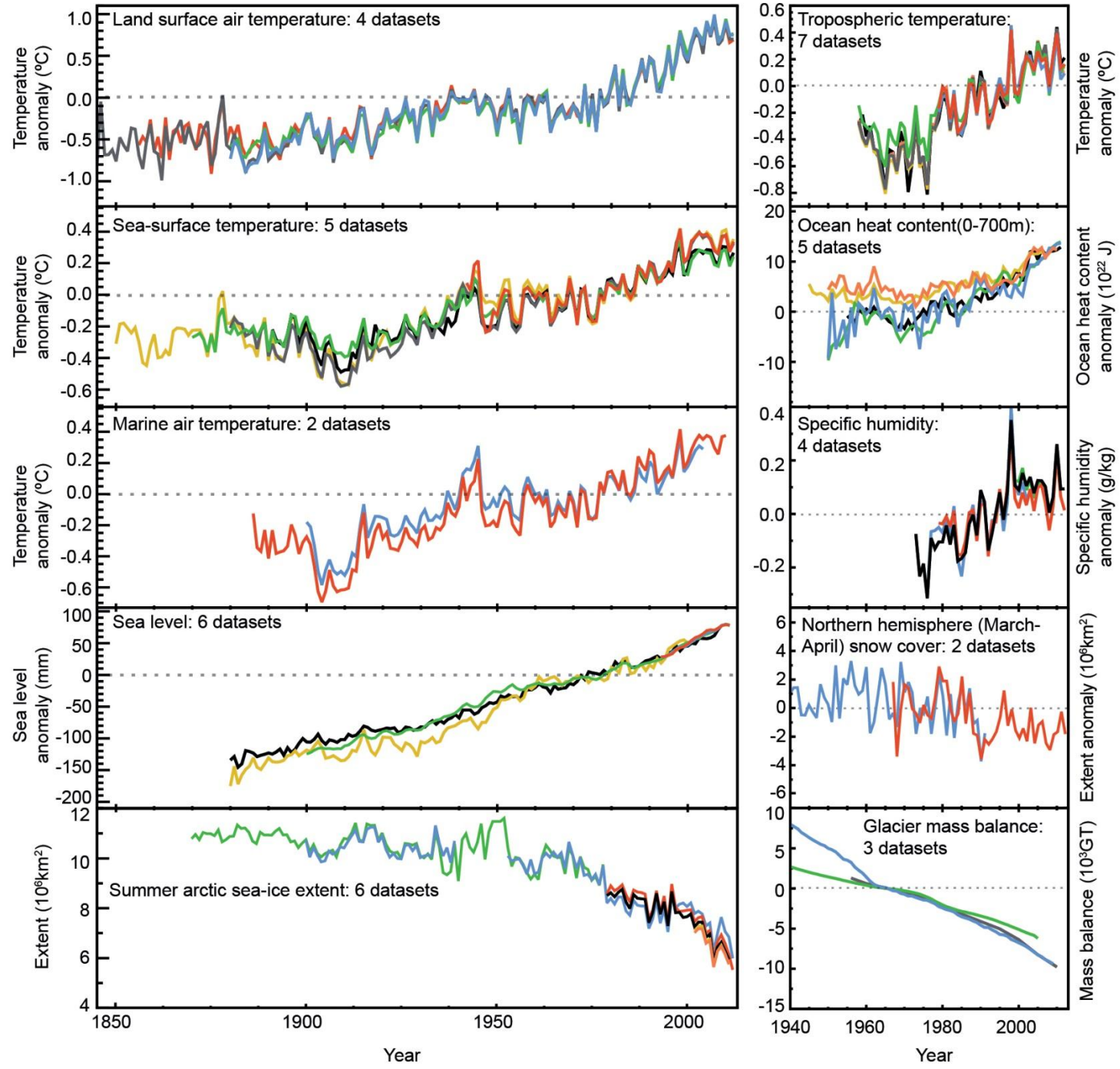


IPCC, 2013

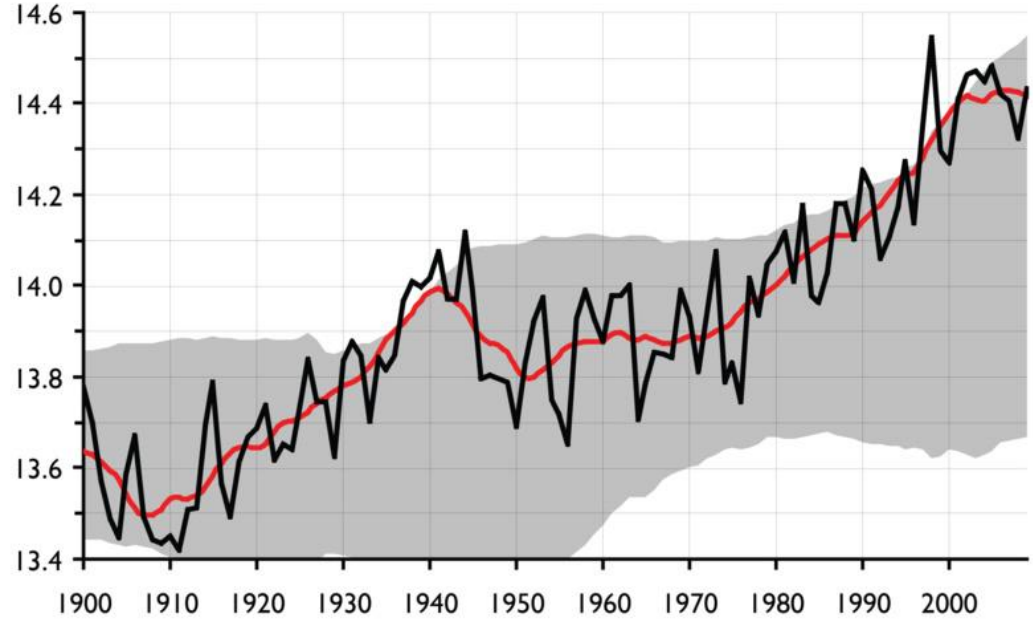


Zmiany średniej temperatury powietrza przy powierzchni Ziemi w ostatnich 100-150 latach

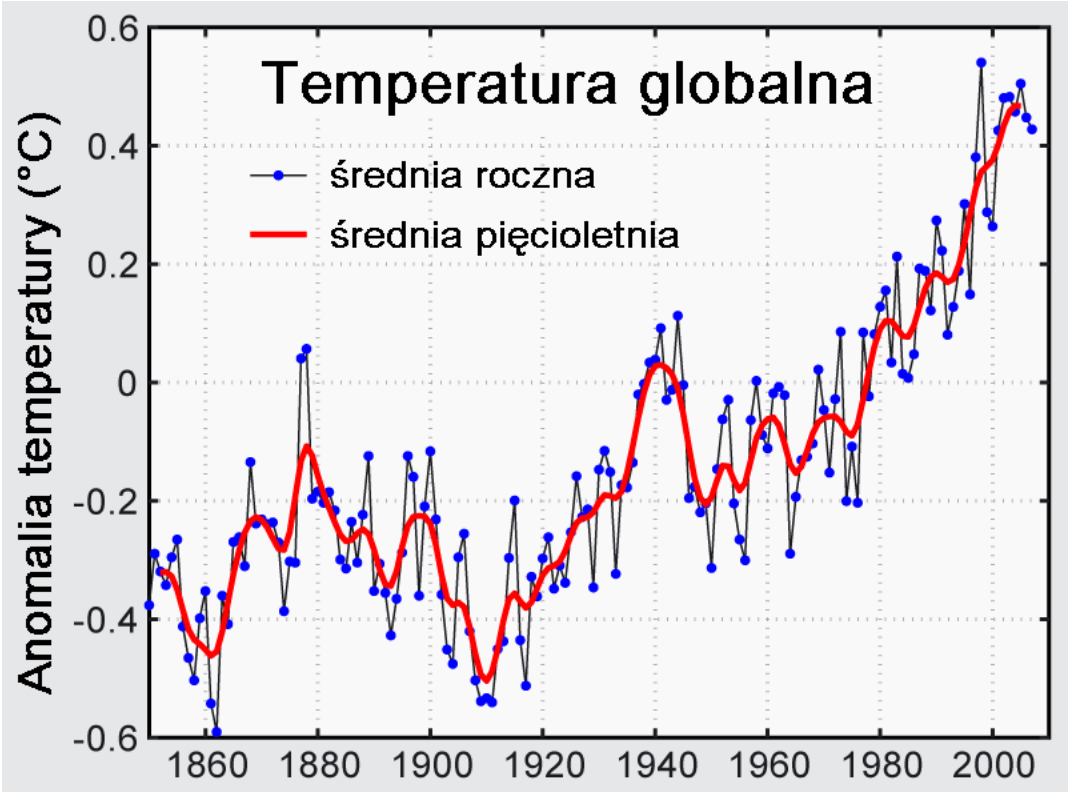


"HadCRUT3". Met Office Hadley Centre for Climate Change, U.K.

# Porównanie różnych serii temperatury

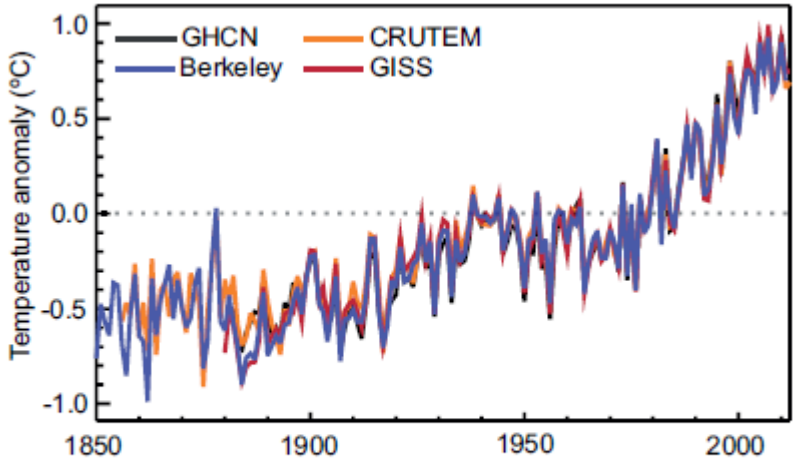


**Figure 2.14 |** Global annual average land-surface air temperature (LSAT) anomalies relative to a 1961–1990 climatology from the latest versions of four different data sets (Berkeley, CRUTEM, GHCN and GISS).

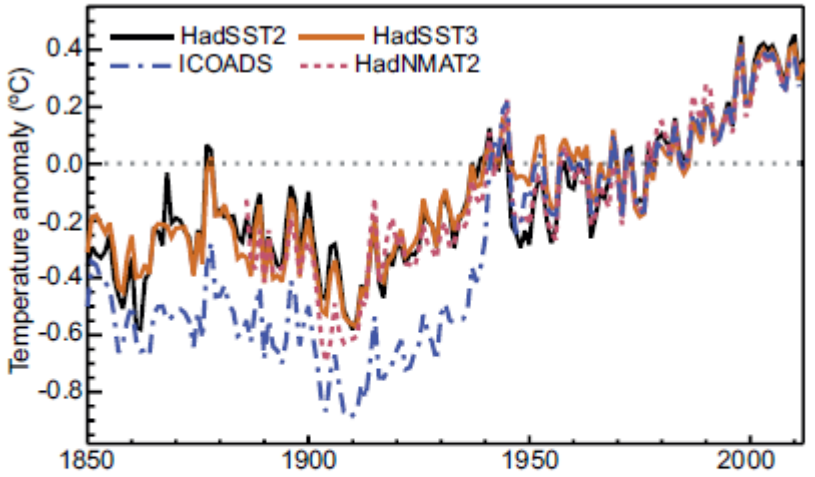


**Figure 2.16 |** Global annual average sea surface temperature (SST) and Night Marine Air Temperature (NMAT) relative to a 1961–1990 climatology from gridded data sets of SST observations (HadSST2 and its successor HadSST3), the raw SST measurement archive (ICOADS, v2.5) and night marine air temperatures data set HadNMAT2 (Kent et al., 2013). HadSST2 and HadSST3 both are based on SST observations from versions of the ICOADS data set, but differ in degree of measurement bias correction.

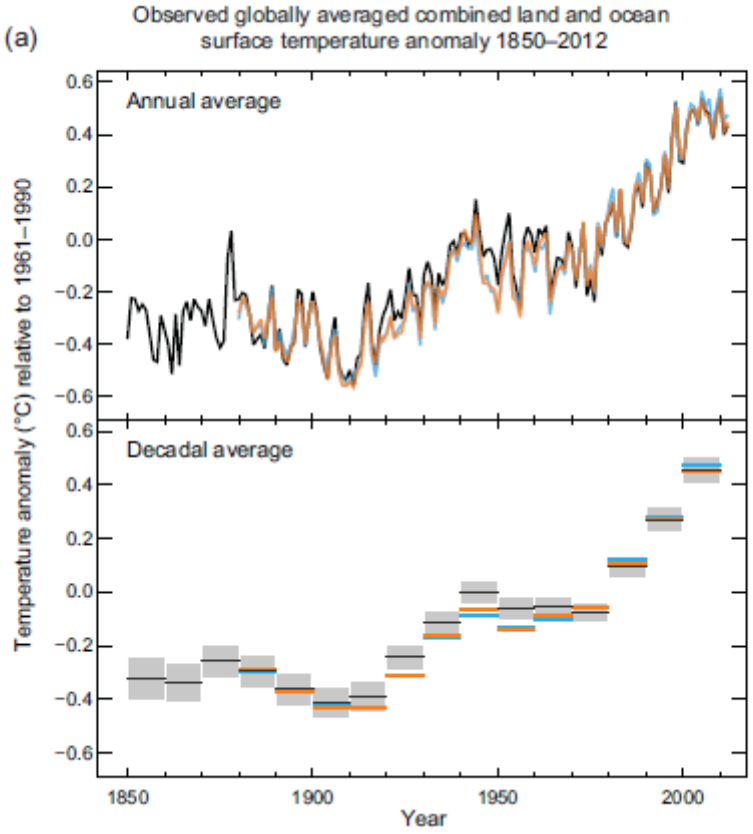
(a)
Observed globally averaged combined land and ocean surface temperature anomaly 1850–2012
Annual average
Decadal average
Temperature anomaly (°C) relative to 1961–1990
0.6
0.4
0.2
0.0
−0.2
−0.4
−0.6
1850
1900
1950
2000
Year

IPCC, 2013

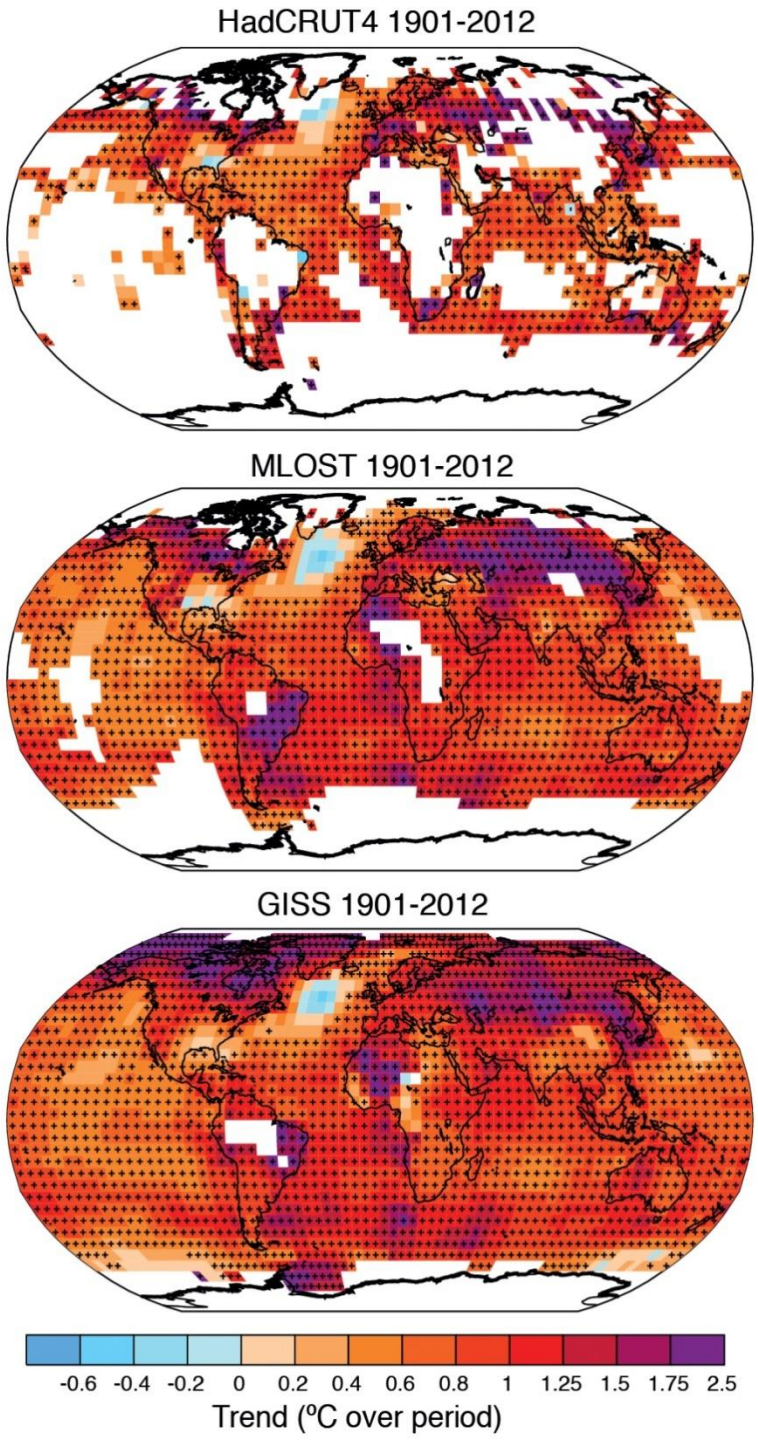
HadCRUT4 1901-2012
MLOST 1901-2012
GISS 1901-2012
-0.6 -0.4 -0.2 0 0.2 0.4 0.6 0.8 1 1.25 1.5 1.75 2.5
Trend (ºC over period)

# Porównanie trendów temperatury dla obszarów lądów, oceanów oraz dla całej ziemi

**Table 2.4:** | Trend estimates and 90% confidence intervals (Box 2.2) for LSAT global average values over five common periods.

| Data Set | Trends in °C per decade | | | | |
|---|---|---|---|---|---|
| | 1880–2012 | 1901–2012 | 1901–1950 | 1951–2012 | 1979–2012 |
| CRUTEM4.1.1.0 (Jones et al., 2012) | 0.086 ± 0.015 | 0.095 ± 0.020 | 0.097 ± 0.029 | 0.175 ± 0.037 | 0.254 ± 0.050 |
| GHCNv3.2.0 (Lawrimore et al., 2011) | 0.094 ± 0.016 | 0.107 ± 0.020 | 0.100 ± 0.033 | 0.197 ± 0.031 | 0.273 ± 0.047 |
| GISS (Hansen et al., 2010) | 0.095 ± 0.015 | 0.099 ± 0.020 | 0.098 ± 0.032 | 0.188 ± 0.032 | 0.267 ± 0.054 |
| Berkeley (Rohde et al., 2013) | 0.094 ± 0.013 | 0.101 ± 0.017 | 0.111 ± 0.034 | 0.175 ± 0.029 | 0.254 ± 0.049 |

**Table 2.6 |** Trend estimates and 90% confidence intervals (Box 2.2) for interpolated SST data sets (uninterpolated state-of-the-art HadSST3 data set is included for comparison). Dash indicates not enough data available for trend calculation.

| Data Set | Trends in °C per decade | | | | |
|---|---|---|---|---|---|
| | 1880–2012 | 1901–2012 | 1901–1950 | 1951–2012 | 1979–2012 |
| HadISST (Rayner et al., 2003) | 0.042 ± 0.007 | 0.052 ± 0.007 | 0.067 ± 0.024 | 0.064 ± 0.015 | 0.072 ± 0.024 |
| COBE-SST (Ishii et al., 2005) | – | 0.058 ± 0.007 | 0.066 ± 0.032 | 0.071 ± 0.014 | 0.073 ± 0.020 |
| ERSSTv3b (Smith et al., 2008) | 0.054 ± 0.015 | 0.071 ± 0.011 | 0.097 ± 0.050 | 0.088 ± 0.017 | 0.105 ± 0.031 |
| HadSST3 (Kennedy et al., 2011a) | 0.054 ± 0.012 | 0.067 ± 0.013 | 0.117 ± 0.028 | 0.074 ± 0.027 | 0.124 ± 0.030 |

**Table 2.7 |** Same as Table 2.4, but for global mean surface temperature (GMST) over five common periods.

| Data Set | Trends in °C per decade | | | | |
|---|---|---|---|---|---|
| | 1880–2012 | 1901–2012 | 1901–1950 | 1951–2012 | 1979–2012 |
| HadCRUT4 (Morice et al., 2012) | 0.062 ± 0.012 | 0.075 ± 0.013 | 0.107 ± 0.026 | 0.106 ± 0.027 | 0.155 ± 0.033 |
| NCDC MLOST (Vose et al., 2012b) | 0.064 ± 0.015 | 0.081 ± 0.013 | 0.097 ± 0.040 | 0.118 ± 0.021 | 0.151 ± 0.037 |
| GISS (Hansen et al., 2010) | 0.065 ± 0.015 | 0.083 ± 0.013 | 0.090 ± 0.034 | 0.124 ± 0.020 | 0.161 ± 0.033 |

# Temperatury w latach 1999-2008

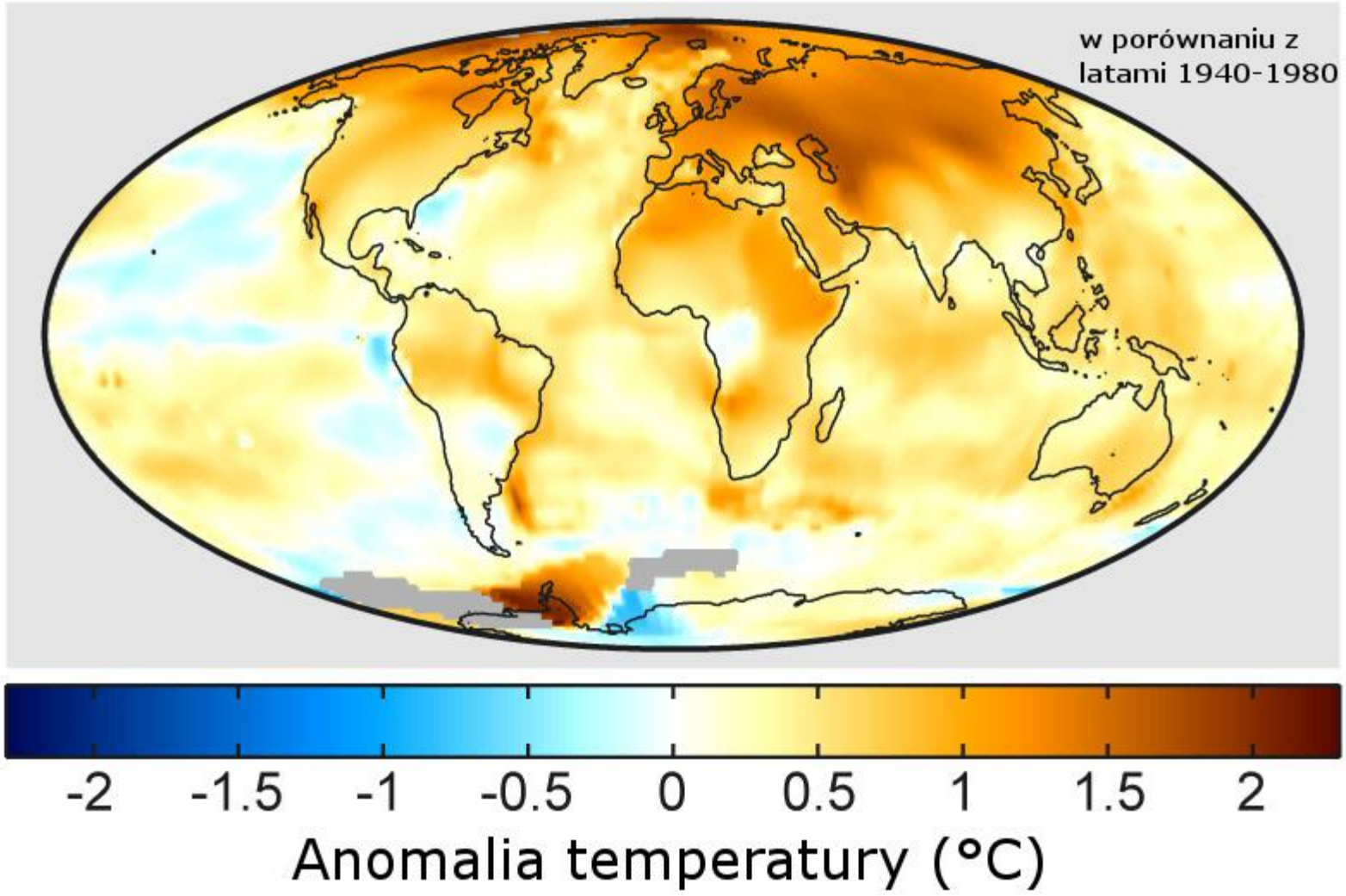

Półwysep Antarktyczny jest jednym z najszybciej ogrzewających się miejsc na Ziemi.

Długości obserwacji meteorologicznych, obserwowane trendy temperatury [ºC/stulecie] błędem oraz istotność trendu.

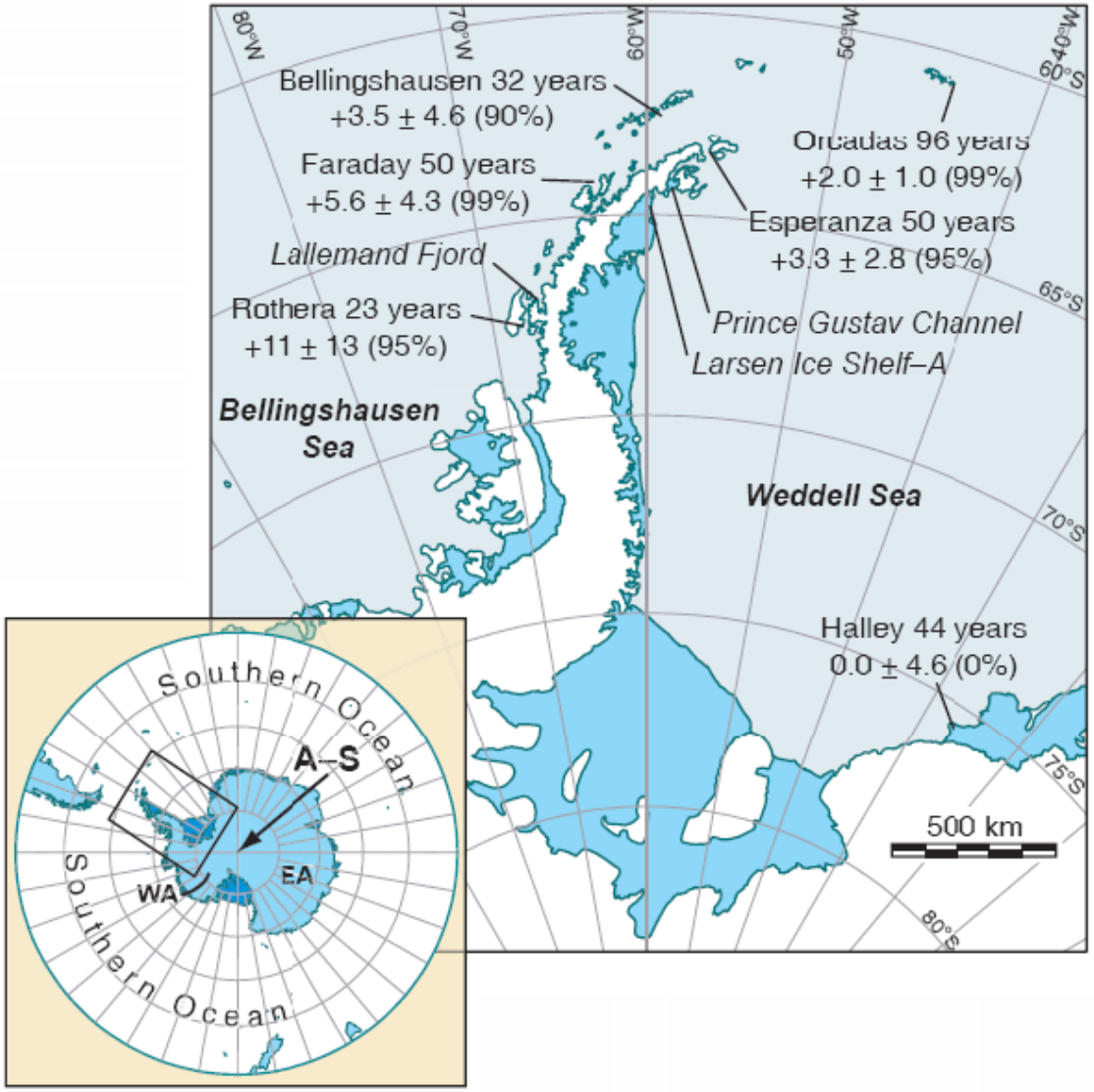

# Globalne zmiany temperatury w stratosferze i troposferze

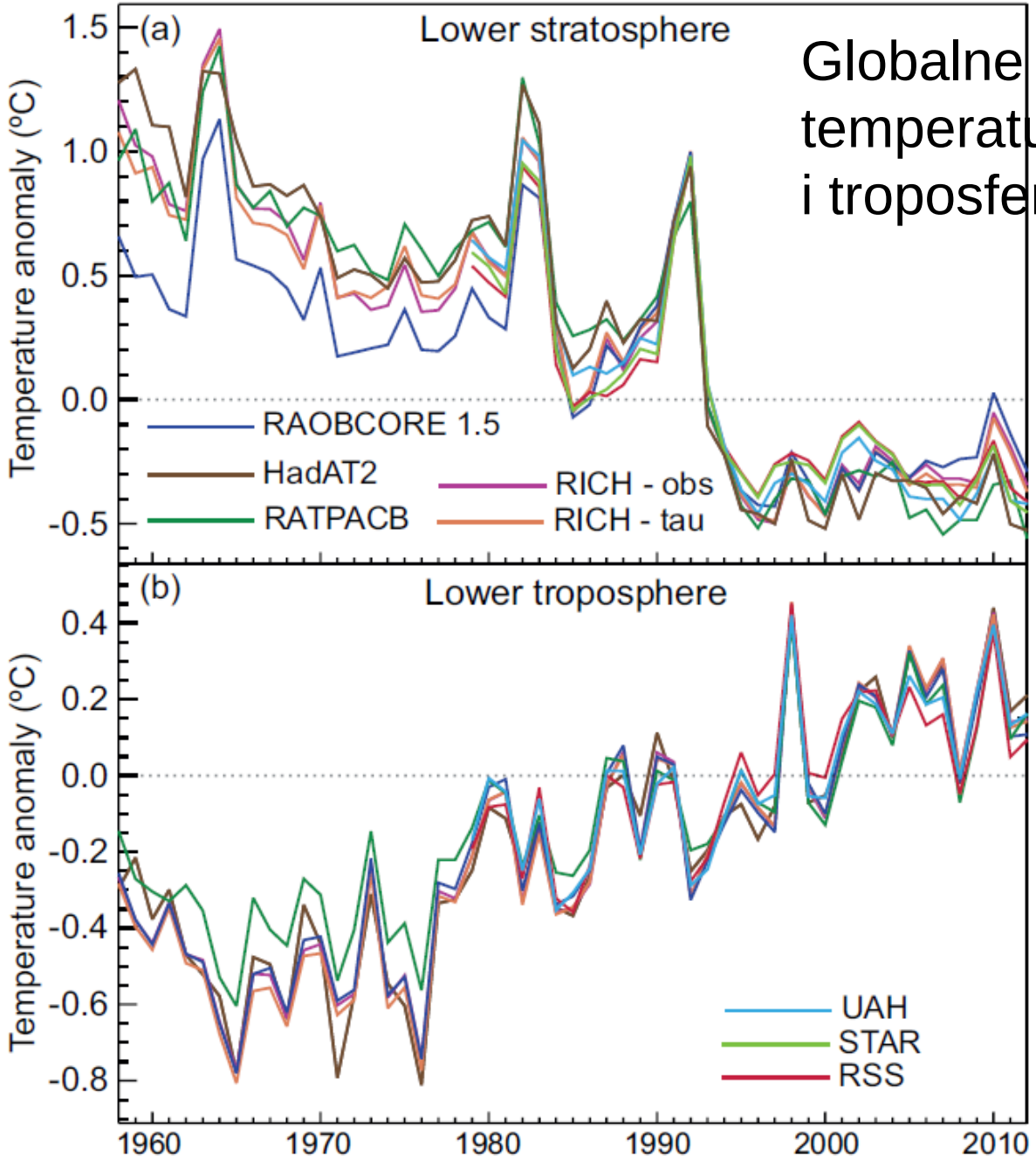


**Figure 2.24 |** Global annual average lower stratospheric (top) and lower tropospheric (bottom) temperature anomalies relative to a 1981–2010 climatology from different data sets. STAR does not produce a lower tropospheric temperature product. Note that the *y*-axis resolution differs between the two panels.

# Porównanie trendów w troposferze i stratosferze

**Table 2.8 |** Trend estimates and 90% confidence intervals (Box 2.2) for radiosonde and MSU data set global average values over the radiosonde (1958–2012) and satellite periods (1979–2012). LT indicates Lower Troposphere, MT indicates Mid Troposphere and LS indicates Lower Stratosphere (Figure 2.23. Satellite records start only in 1979 and STAR do not produce an LT product.

| Data Set | Trends in °C per decade | | | | | |
|---|---|---|---|---|---|---|
| | 1958–2012 | | | 1979–2012 | | |
| | LT | MT | LS | LT | MT | LS |
| HadAT2 (Thorne et al., 2005) | 0.159 ± 0.038 | 0.095 ± 0.034 | –0.339 ± 0.086 | 0.162 ± 0.047 | 0.079 ± 0.057 | –0.436 ± 0.204 |
| RAOBCORE 1.5 (Haimberger et al., 2012) | 0.156 ± 0.031 | 0.109 ± 0.029 | –0.186 ± 0.087 | 0.139 ± 0.049 | 0.079 ± 0.054 | –0.266 ± 0.227 |
| RICH-obs (Haimberger et al., 2012) | 0.162 ± 0.031 | 0.102 ± 0.029 | –0.285 ± 0.087 | 0.158 ± 0.046 | 0.081 ± 0.052 | –0.331 ± 0.241 |
| RICH-tau (Haimberger et al., 2012) | 0.168 ± 0.032 | 0.111 ± 0.030 | –0.280 ± 0.085 | 0.160 ± 0.046 | 0.083 ± 0.052 | –0.345 ± 0.238 |
| RATPAC (Free et al., 2005) | 0.136 ± 0.028 | 0.076 ± 0.028 | –0.338 ± 0.092 | 0.128 ± 0.044 | 0.039 ± 0.051 | –0.468 ± 0.225 |
| UAH (Christy et al., 2003) | | | | 0.138 ± 0.043 | 0.043 ± 0.042 | –0.372 ± 0.201 |
| RSS (Mears and Wentz, 2009a, 2009b) | | | | 0.131 ± 0.045 | 0.079 ± 0.043 | –0.268 ± 0.177 |
| STAR (Zou and Wang, 2011) | | | | | 0.123 ± 0.047 | –0.320 ± 0.175 |

# Trendy temperatury powietrza w dolnej troposferze i stratosferze

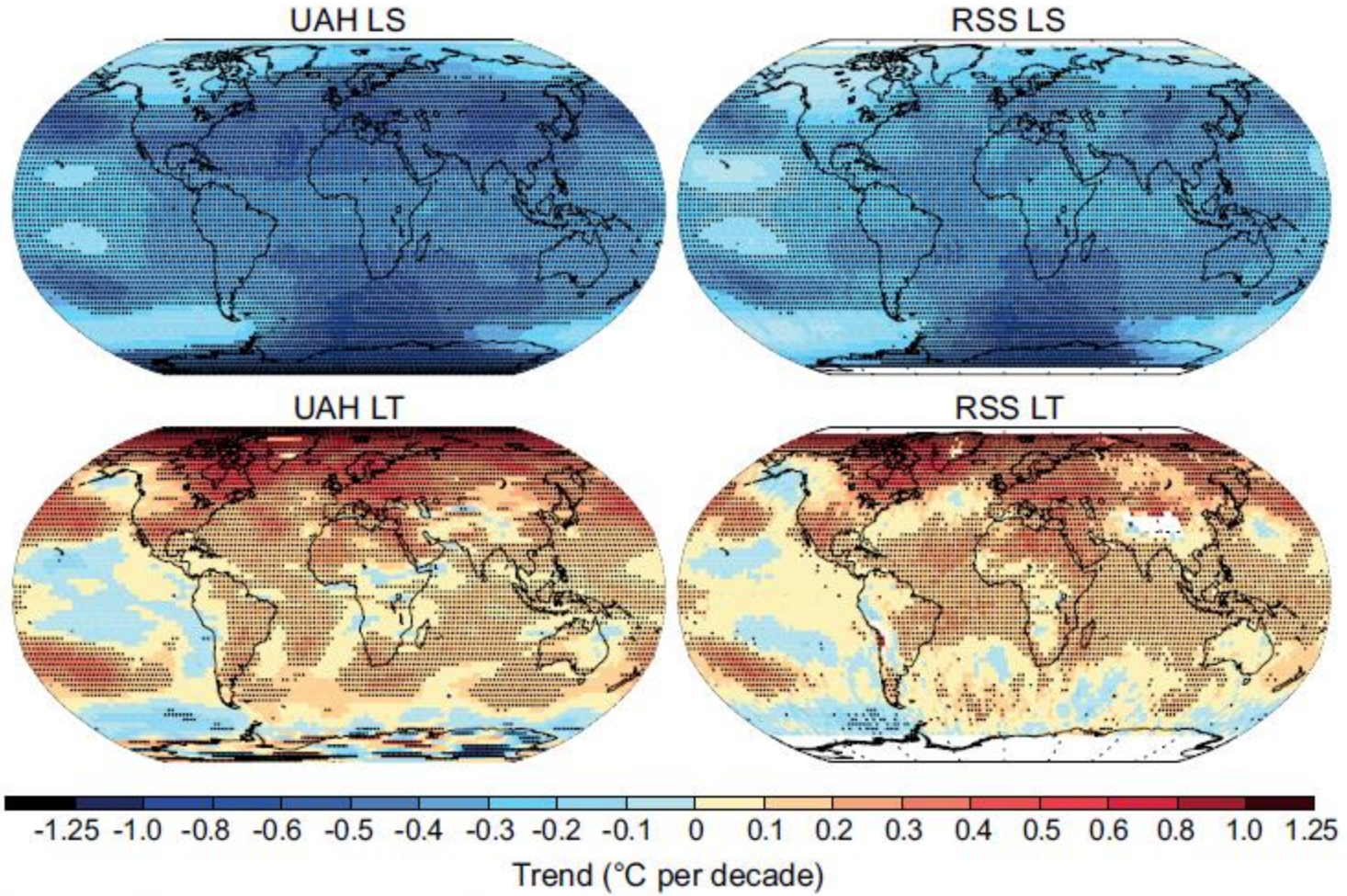


**Figure 2.25 |** Trends in MSU upper air temperature over 1979–2012 from UAH (left-hand panels) and RSS (right-hand panels) and for LS (top row) and LT (bottom row). Data are temporally complete within the sampled domains for each data set. White areas indicate incomplete or missing data. Black plus signs (+) indicate grid boxes where trends are significant (i.e., a trend of zero lies outside the 90% confidence interval).

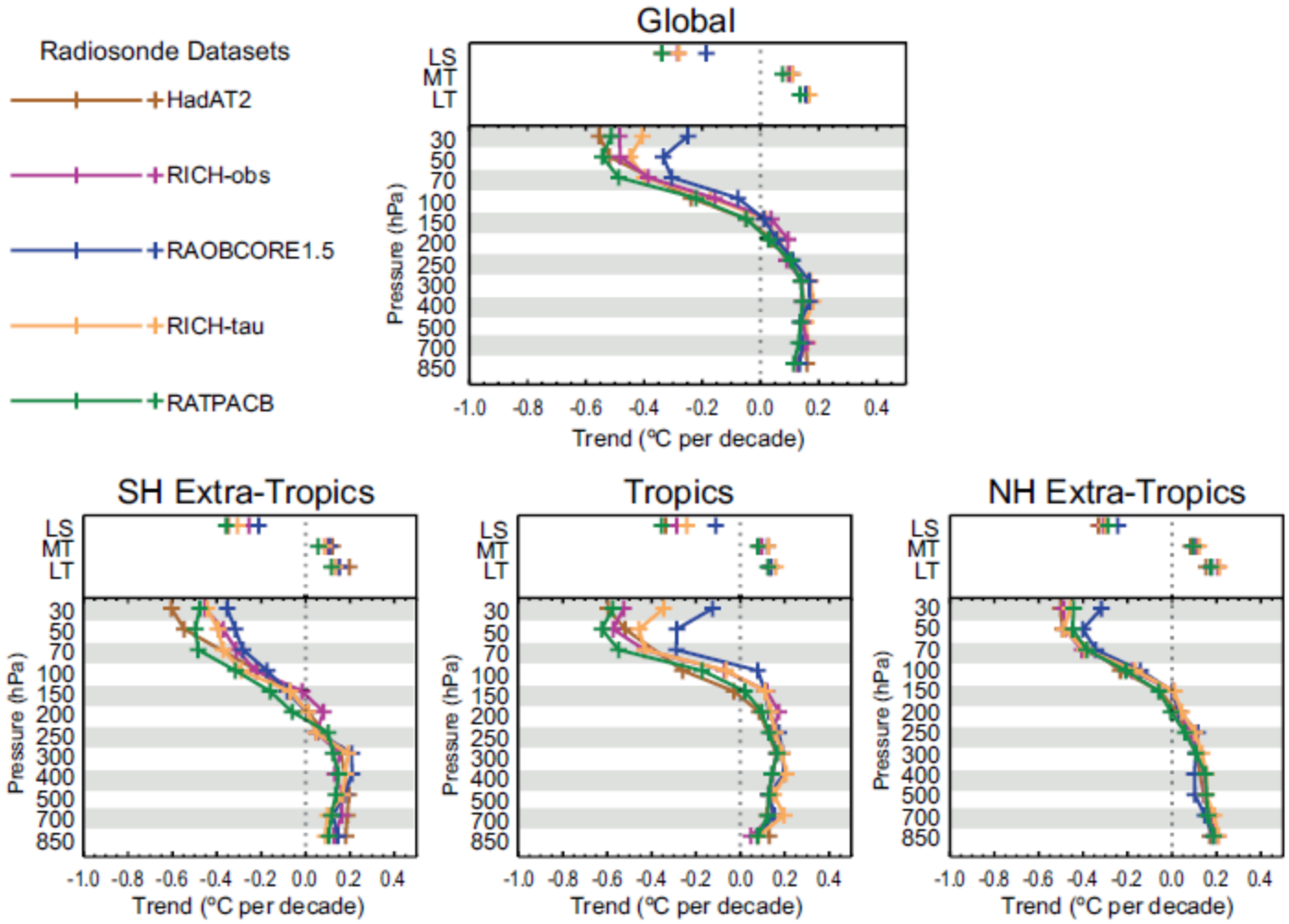


**Figure 2.26 |** Trends in upper air temperature for all available radiosonde data products that contain records for 1958–2012 for the globe (top) and tropics (20°N to 20°S) and extra-tropics (bottom). The bottom panel trace in each case is for trends on distinct pressure levels. Note that the pressure axis is not linear. The top panel points show MSU layer equivalent measure trends. MSU layer equivalents have been processed using the method of Thorne et al. (2005). No attempts have been made to sub-sample to a common data mask.

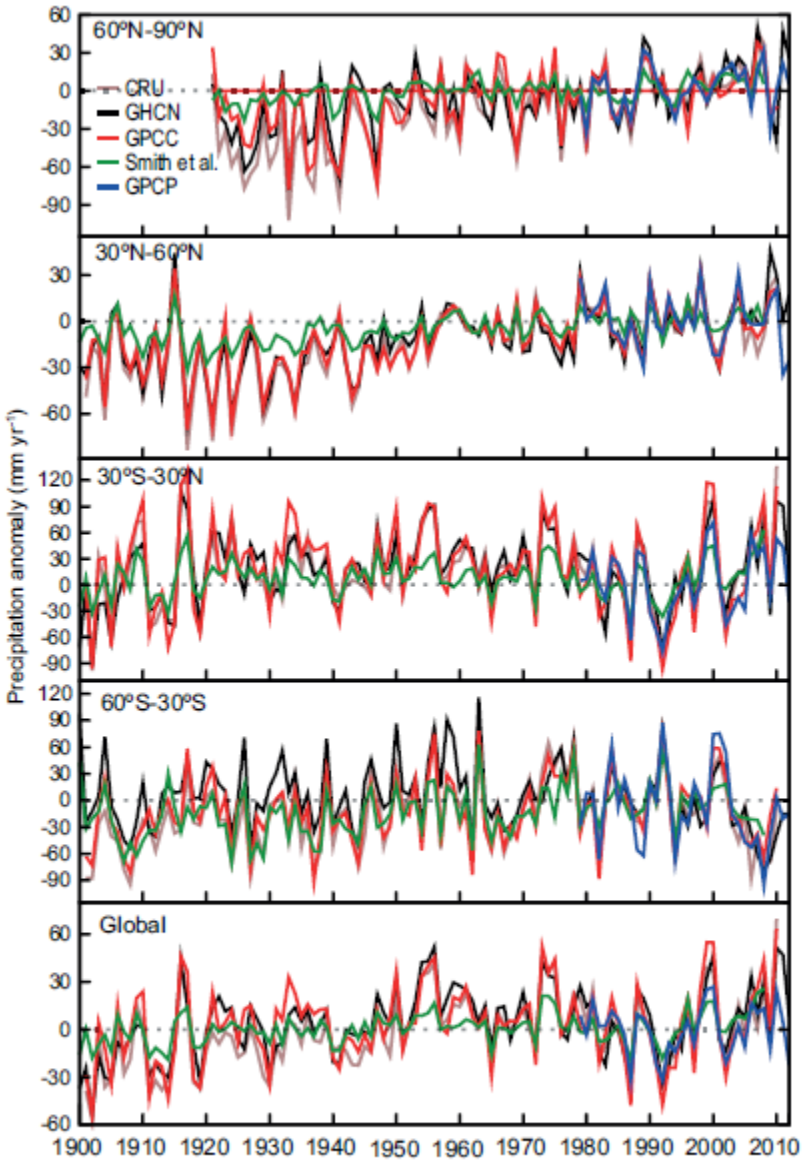


**Figure 2.28 |** Annual precipitation anomalies averaged over land areas for four latitudinal bands and the globe from five global precipitation data sets relative to a 1981–2000 climatology.

# Zmiany w cyklu hydrologicznym: opady

**Table 2.9 |** Trend estimates and 90% confidence intervals (Box 2.2) for annual precipitation for each time series in Figure 2.28 over two common periods of record.

| Data Set | Area | Trends in mm $yr^{-1}$ per decade | |
|---|---|---|---|
| | | 1901–2008 | 1951–2008 |
| CRU TS 3.10.01 (updated from Mitchell and Jones, 2005) | Global | 2.77 ± 1.46 | –2.12 ± 3.52 |
| GHCN V2 (updated through 2011; Vose et al., 1992) | Global | 2.08 ± 1.66 | –2.77 ± 3.92 |
| GPCC V6 (Becker et al., 2013) | Global | 1.48 ± 1.65 | –1.54 ± 4.50 |
| Smith et al. (2012) | Global | 1.01 ± 0.64 | 0.68 ± 2.07 |

**Table 2.10 |** Trend estimates and 90% confidence intervals (Box 2.2) for annual precipitation for each time series in Figure 2.28 over two periods. Dashes indicate not enough data available for trend calculation. For the latitudinal band 90°S to 60°S not enough data exist for each product in either period.

| Data Set | Area | Trends in mm $yr^{-1}$ per decade | |
|---|---|---|---|
| | | 1901–2008 | 1951–2008 |
| **CRU TS 3.10.01 (updated from Mitchell and Jones, 2005)** | 60°N–90°N | – | 5.82 ± 2.72 |
| | 30°N–60°N | 3.82 ± 1.14 | 1.13 ± 2.01 |
| | 30°S–30°N | 0.89 ± 2.89 | –4.22 ± 8.27 |
| | 60°S–30°S | 3.88 ± 2.28 | –3.73 ± 5.94 |
| **GHCN V2 (updated through 2011; Vose et al., 1992)** | 60°N–90°N | – | 4.52 ± 2.64 |
| | 30°N–60°N | 3.23 ± 1.10 | 1.39 ± 1.98 |
| | 30°S–30°N | 1.01 ± 3.00 | –5.15 ± 7.28 |
| | 60°S–30°S | –0.57 ± 2.27 | –8.01 ± 5.63 |
| **GPCC V6 (Becker et al., 2013)** | 60°N–90°N | – | 2.69 ± 2.54 |
| | 30°N–60°N | 3.14 ± 1.05 | 1.50 ± 1.93 |
| | 30°S–30°N | –0.48 ± 3.35 | –4.16 ± 9.65 |
| | 60°S–30°S | 2.40 ± 2.01 | –0.51 ± 5.45 |
| **Smith et al. (2012)** | 60°N–90°N | – | 0.63 ± 1.27 |
| | 30°N–60°N | 1.44 ± 0.50 | 0.97 ± 0.88 |
| | 30°S–30°N | 0.43 ± 1.48 | 0.67 ± 4.75 |
| | 60°S–30°S | 2.94 ± 1.40 | 0.78 ± 3.31 |

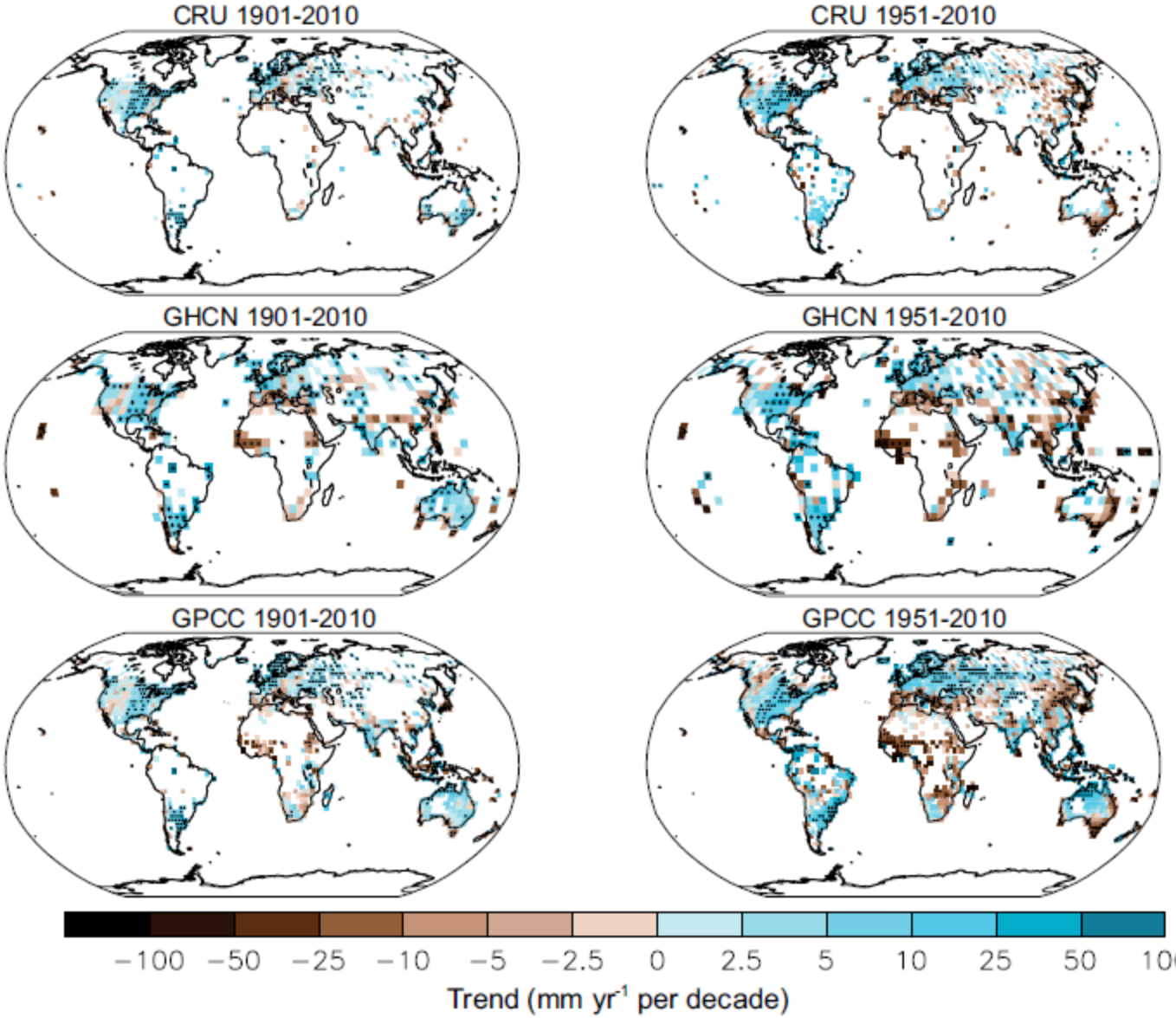


**Figure 2.29 |** Trends in annual precipitation over land from the CRU, GHCN and GPCC data sets for 1901–2010 (left-hand panels) and 1951–2010 (right-hand panels). Trends have been calculated only for those grid boxes with greater than 70% complete records and more than 20% data availability in first and last decile of the period. White areas indicate incomplete or missing data. Black plus signs (+) indicate grid boxes where trends are significant (i.e., a trend of zero lies outside the 90% confidence interval).

# Zmiany zawartości pary wodnej w atmosferze

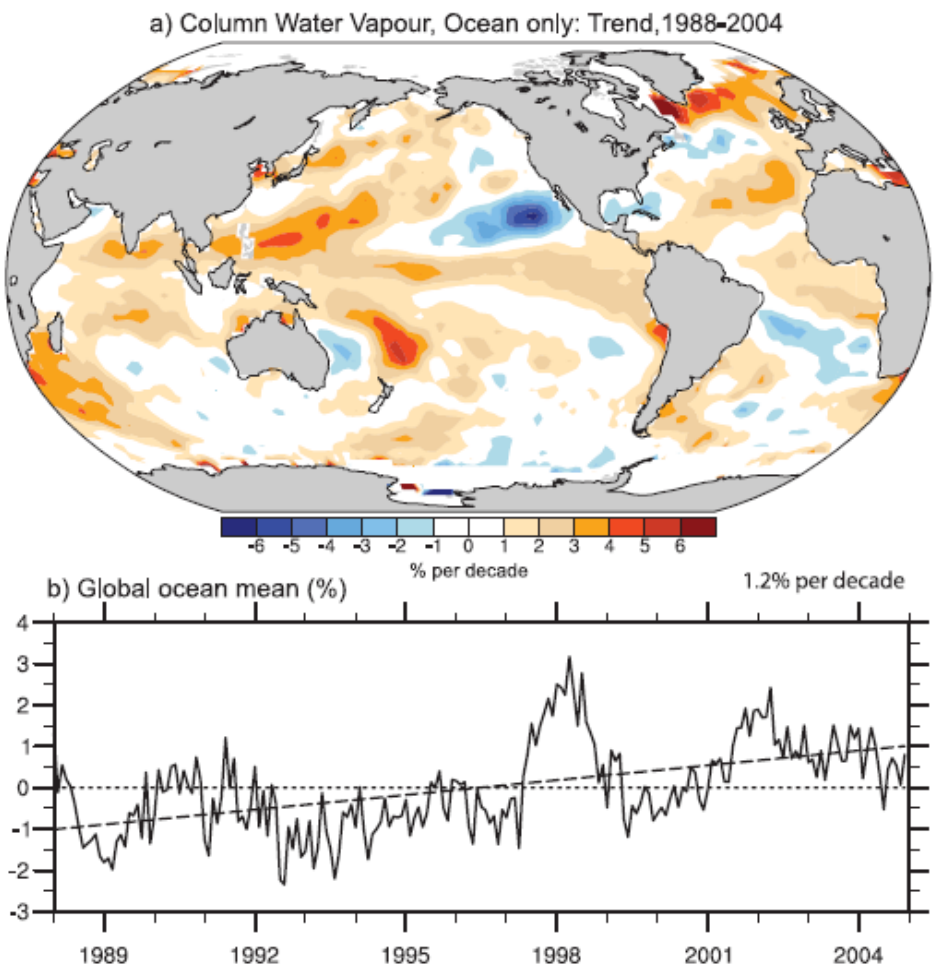


**Figure 3.20.** *Linear trends in precipitable water (total column water vapour) in % per decade (top) and monthly time series of anomalies relative to the 1988 to 2004 period in % over the global ocean plus linear trend (bottom), from RSS SSM/I (updated from Trenberth et al., 2005a).*

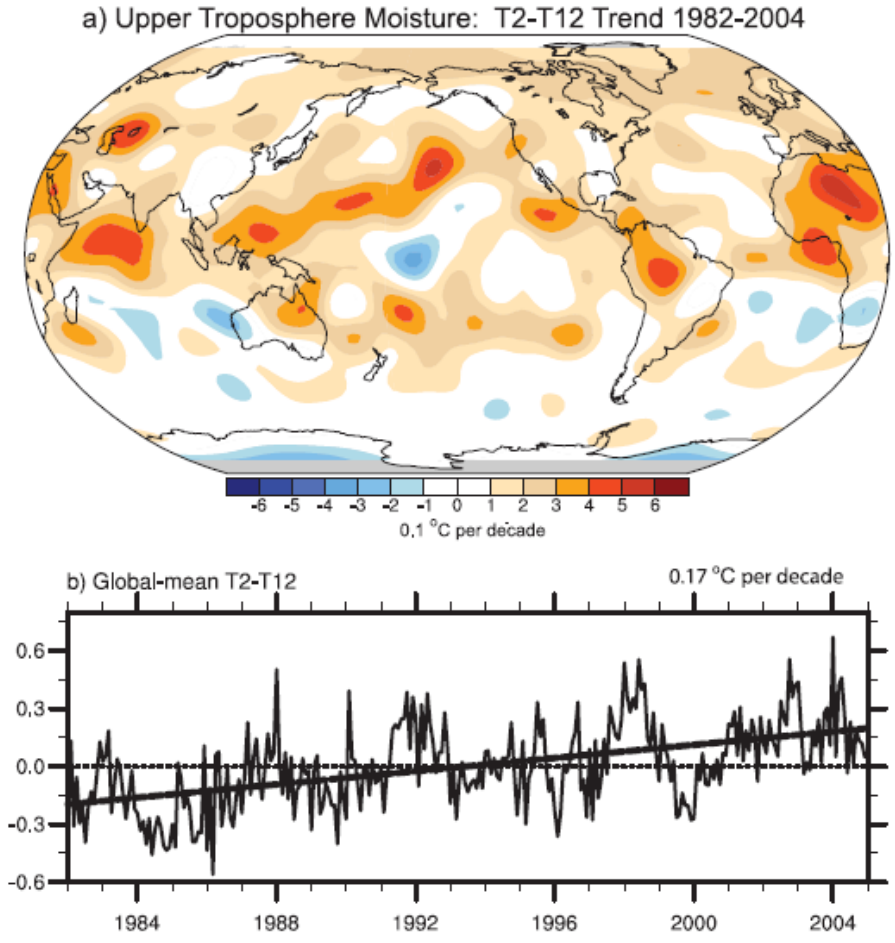


**Figure 3.21.** *The radiative signature of upper-tropospheric moistening is given by upward linear trends in T2–T12 for 1982 to 2004 (0.1 °C per decade; top) and monthly time series of the global-mean (80°N to 80°S) anomalies relative to 1982 to 2004 (°C) and linear trend (dashed; bottom). Data are from the RSS T2 and HIRS T12 (Soden et al., 2005). The map is smoothed to spectral truncation T31 resolution.*

# Zmiany wilgotności: wilgotność właściwa i całkowita zawartość pary wodnej

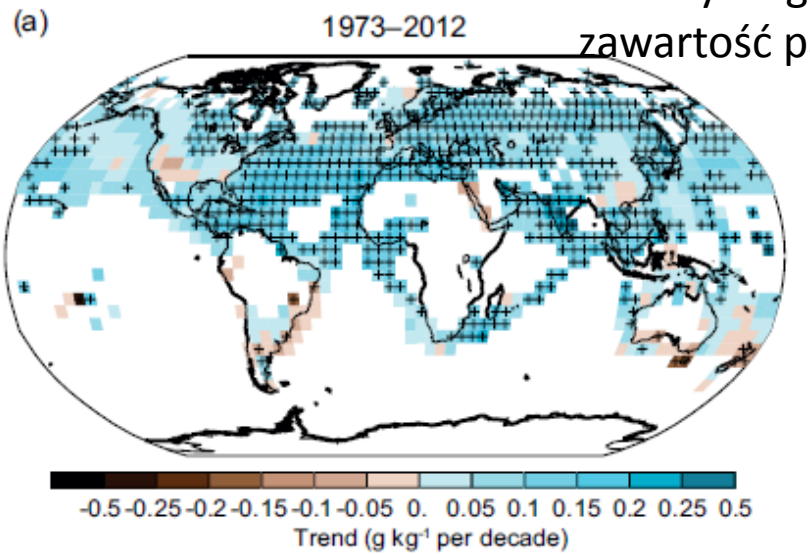


**Figure 2.30 |** (a) Trends in surface specific humidity from HadISDH and NOCS over 1973–2012. Trends have been calculated only for those grid boxes with greater than 70% complete records and more than 20% data availability in first and last decile of the period. White areas indicate incomplete or missing data. Black plus signs (+) indicate grid boxes where trends are significant (i.e., a trend of zero lies outside the 90% confidence interval). (b) Global annual average anomalies in land surface specific humidity from Dai (2006; red), HadCRUH (Willett et al., 2013; orange), HadISDH (Willett et al., 2013; black), and ERA-Interim (Simmons et al., 2010; blue). Anomalies are relative to the 1979–2003 climatology.

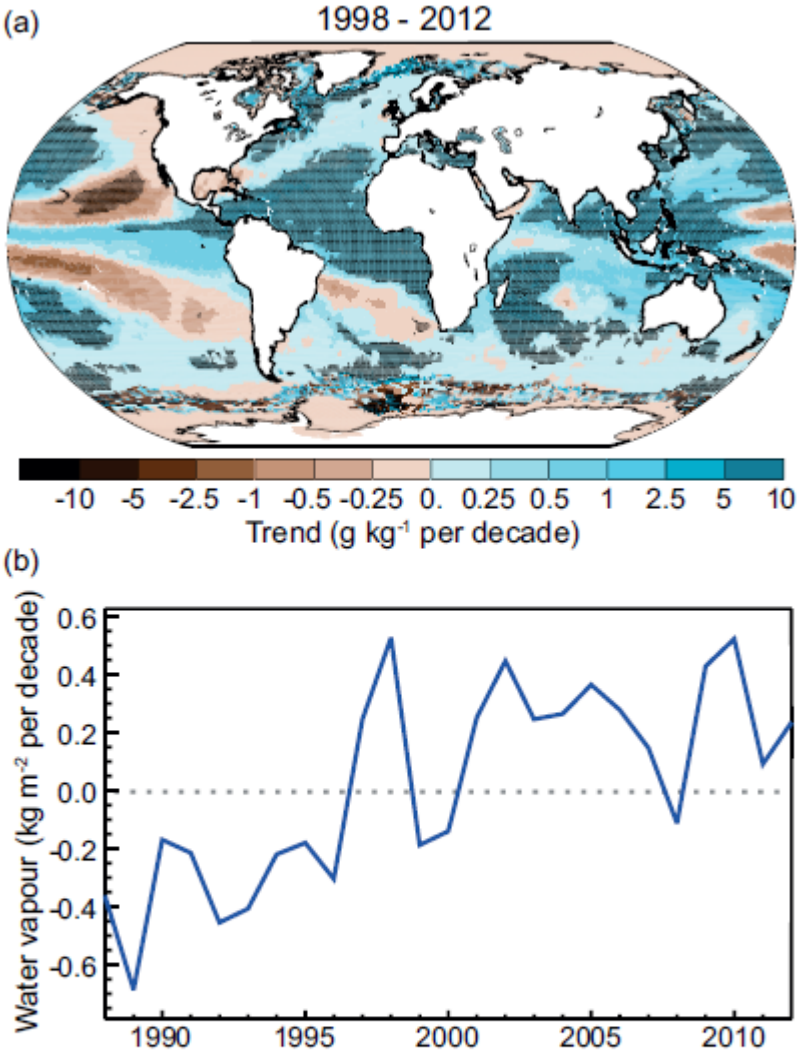


**Figure 2.31 |** (a) Trends in column integrated water vapour over ocean surfaces from Special Sensor Microwave Imager (Wentz et al., 2007) for the period 1988–2010. Trends have been calculated only for those grid boxes with greater than 70% complete records and more than 20% data availability in first and last decile of the period. Black plus signs (+) indicate grid boxes where trends are significant (i.e., a trend of zero lies outside the 90% confidence interval). (b) Global annual average anomalies in column integrated water vapour averaged over ocean surfaces. Anomalies are relative to the 1988–2007 average.

# Trendy wilgotności właściwej przy powierzchni ziemi

**Table 2.11 |** Trend estimates and 90% confidence intervals (Box 2.2) for surface humidity over two periods.

| | Data Set | Trends in % per decade | |
|---|---|---|---|
| | | 1976–2003 | 1973–2012 |
| Land | HadISDH (Willett et al., 2008) | 0.127 ± 0.037 | 0.091 ± 0.023 |
| | HadCRUH_land (Willett et al., 2008) | 0.128 ± 0.043 | |
| | Dai_land (Dai, 2006) | 0.099 ± 0.046 | |
| Ocean | NOCS (Berry and Kent, 2009) | 0.114 ± 0.064 | 0.090 ± 0.033 |
| | HadCRUH_marine (Willett et al., 2008) | 0.065 ± 0.049 | |
| | Dai_marine (Dai, 2006) | 0.058 ± 0.044 | |

# Zmiany częstotliwości występowania wysokich i niskich temperatur powietrza

**Table 2.12 |** Trend estimates and 90% confidence intervals (Box 2.2) for global values of cold nights (TN10p), cold days (TX10p), warm nights (TN90p) and warm days (TX90p) over the periods 1951–2010 and 1979–2010 (see Box 2.4, Table 1 for more information on indices).

| Data Set | Trends in % per decade | | | | | | | |
|---|---|---|---|---|---|---|---|---|
| | TN10p | | TX10p | | TN90p | | TX90p | |
| | 1951–2010 | 1979–2010 | 1951–2010 | 1979–2010 | 1951–2010 | 1979–2010 | 1951–2010 | 1979–2010 |
| HadEX2 (Donat et al., 2013c) | −3.9 ± 0.6 | −4.2 ± 1.2 | −2.5 ± 0.7 | −4.1 ± 1.4 | 4.5 ± 0.9 | 6.8 ± 1.8 | 2.9 ± 1.2 | 6.3 ± 2.2 |
| HadGHCND (Caesar et al., 2006) | −4.5 ± 0.7 | −4.0 ± 1.5 | −3.3 ± 0.8 | −5.0 ± 1.6 | 5.8 ± 1.3 | 8.6 ± 2.3 | 4.2 ± 1.8 | 9.4 ± 2.7 |
| GHCNDEX (Donat et al., 2013a) | −3.9 ± 0.6 | −3.9 ± 1.3 | −2.6 ± 0.7 | −3.9 ± 1.4 | 4.3 ± 0.9 | 6.3 ± 1.8 | 2.9 ± 1.2 | 6.1 ± 2.2 |

(a) Cold Nights

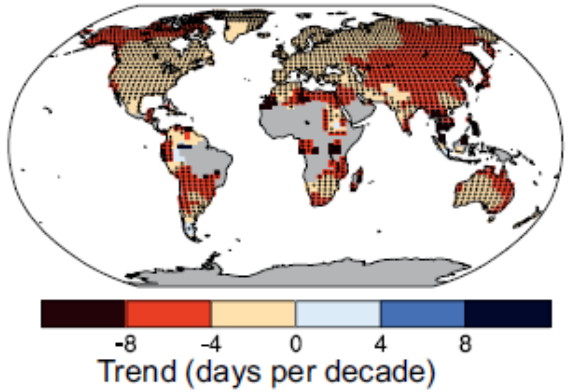


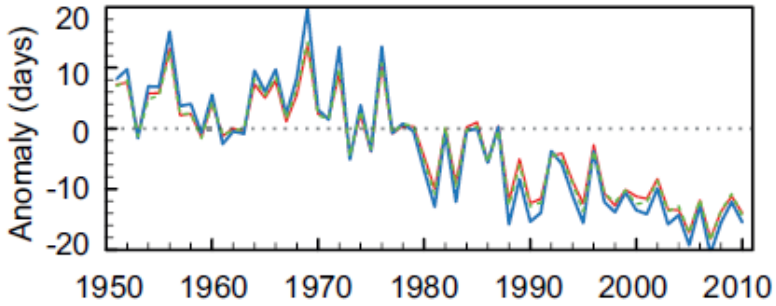


(b) Cold Days

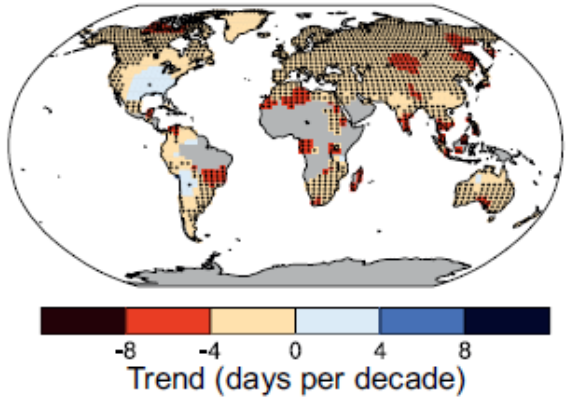


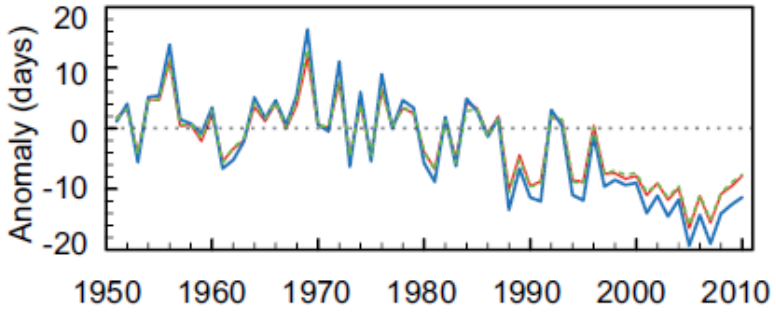

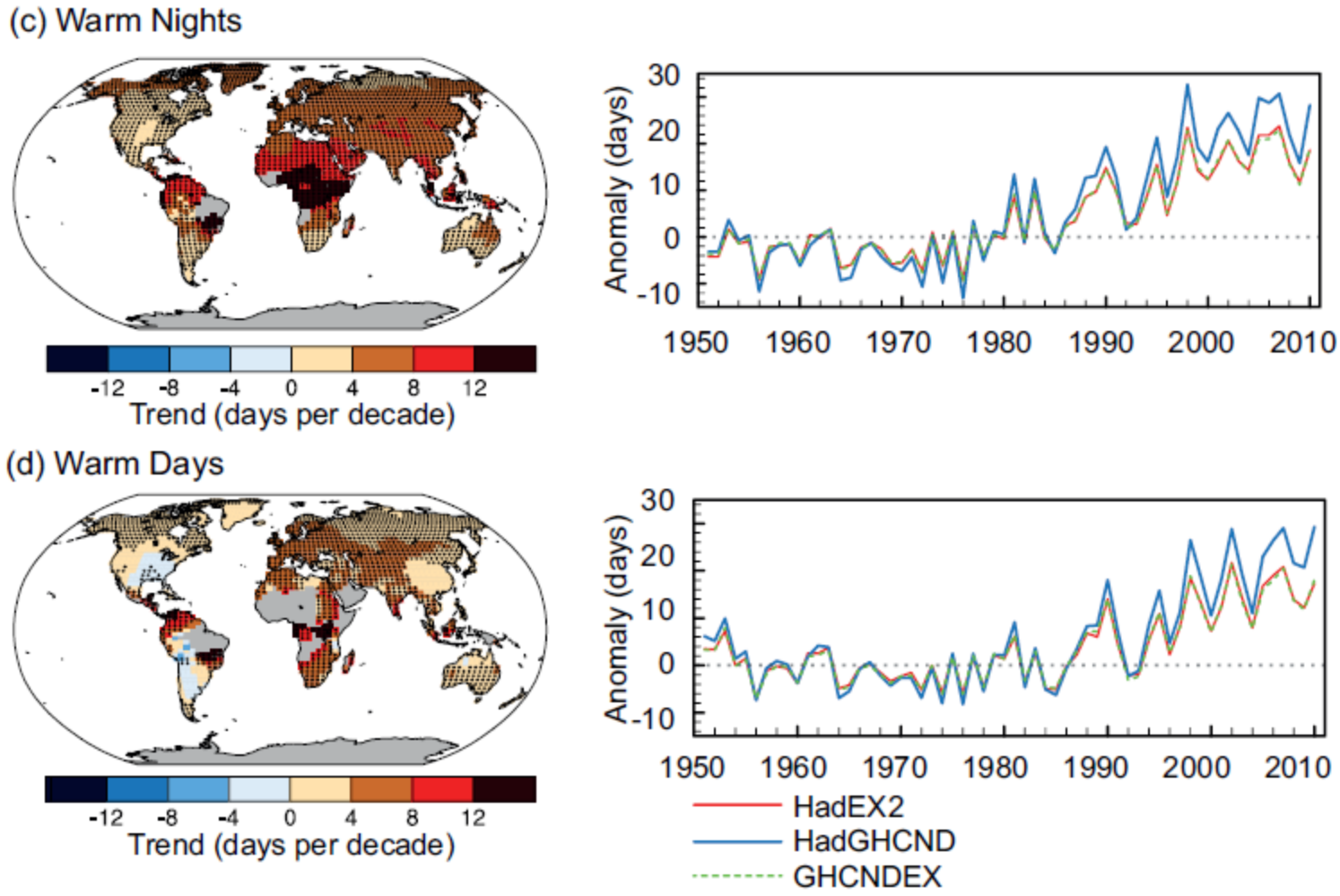


**Figure 2.32 |** Trends in annual frequency of extreme temperatures over the period 1951–2010, for (a) cold nights (TN10p), (b) cold days (TX10p), (c) warm nights (TN90p) and (d) warm days (TX90p) (Box 2.4, Table 1). Trends were calculated only for grid boxes that had at least 40 years of data during this period and where data ended no earlier than 2003. Grey areas indicate incomplete or missing data. Black plus signs (+) indicate grid boxes where trends are significant (i.e., a trend of zero lies outside the 90% confidence interval). The data source for trend maps is HadEX2 (Donat et al., 2013c) updated to include the latest version of the European Climate Assessment data set (Klok and Tank, 2009). Beside each map are the near-global time series of annual anomalies of these indices with respect to 1961–1990 for three global indices data sets: HadEX2 (red); HadGHCND (Caesar et al., 2006; blue) and updated to 2010 and GHCNDEX (Donat et al., 2013a; green). Global averages are only calculated using grid boxes where all three data sets have at least 90% of data over the time period. Trends are significant (i.e., a trend of zero lies outside the 90% confidence interval) for all the global indices shown.

# Trendy w występowaniu ekstremalnych opadów

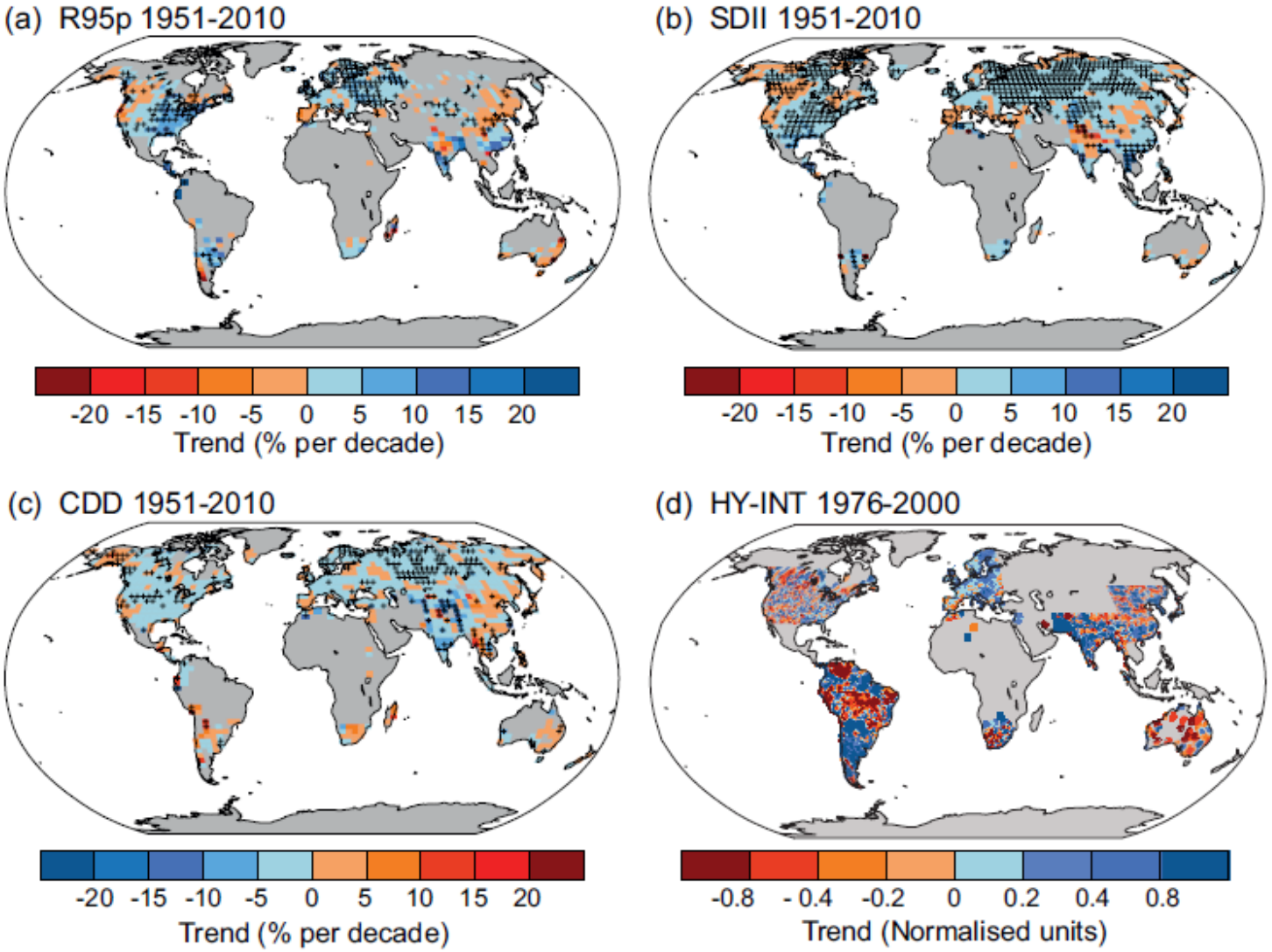


**Figure 2.33 |** Trends in (a) annual amount of precipitation from days >95th percentile (R95p), (b) daily precipitation intensity (SDII) and (c) frequency of the annual maximum number of consecutive dry days (CDD) (Box 2.4, Table 1). Trends are shown as relative values for better comparison across different climatic regions. Trends were calculated only for grid boxes that had at least 40 years of data during this period and where data ended no earlier than 2003. Grey areas indicate incomplete or missing data. Black plus signs (+) indicate grid boxes where trends are significant (i.e., a trend of zero lies outside the 90% confidence interval). The data source for trend maps is HadEX2 (Donat et al., 2013a) updated to include the latest version of the European Climate Assessment data set (Klok and Tank, 2009). (d) Trends (normalized units) in hydroclimatic intensity (HY-INT: a multiplicative measure of length of dry spell and precipitation intensity) over the period 1976–2000 (adapted from Giorgi et al., 2011). An increase (decrease) in HY-INT reflects an increase (decrease) in the length of drought and /or extreme precipitation events.

Zmiany ilości cyklonów tropikalnych

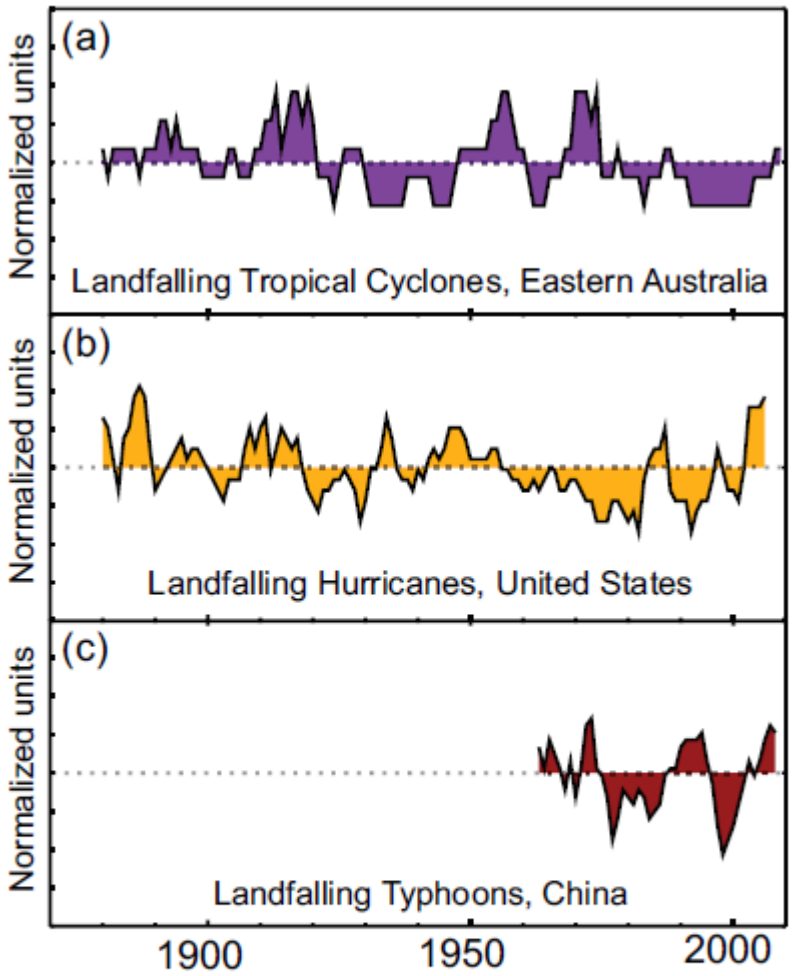


**Figure 2.34 |** Normalized 5-year running means of the number of (a) adjusted land falling eastern Australian tropical cyclones (adapted from Callaghan and Power (2011) and updated to include 2010//2011 season) and (b) unadjusted land falling U.S. hurricanes (adapted from Vecchi and Knutson (2011) and (c) land-falling typhoons in China (adapted from CMA, 2011). Vertical axis ticks represent one standard deviation, with all series normalized to unit standard deviation after a 5-year running mean was applied.

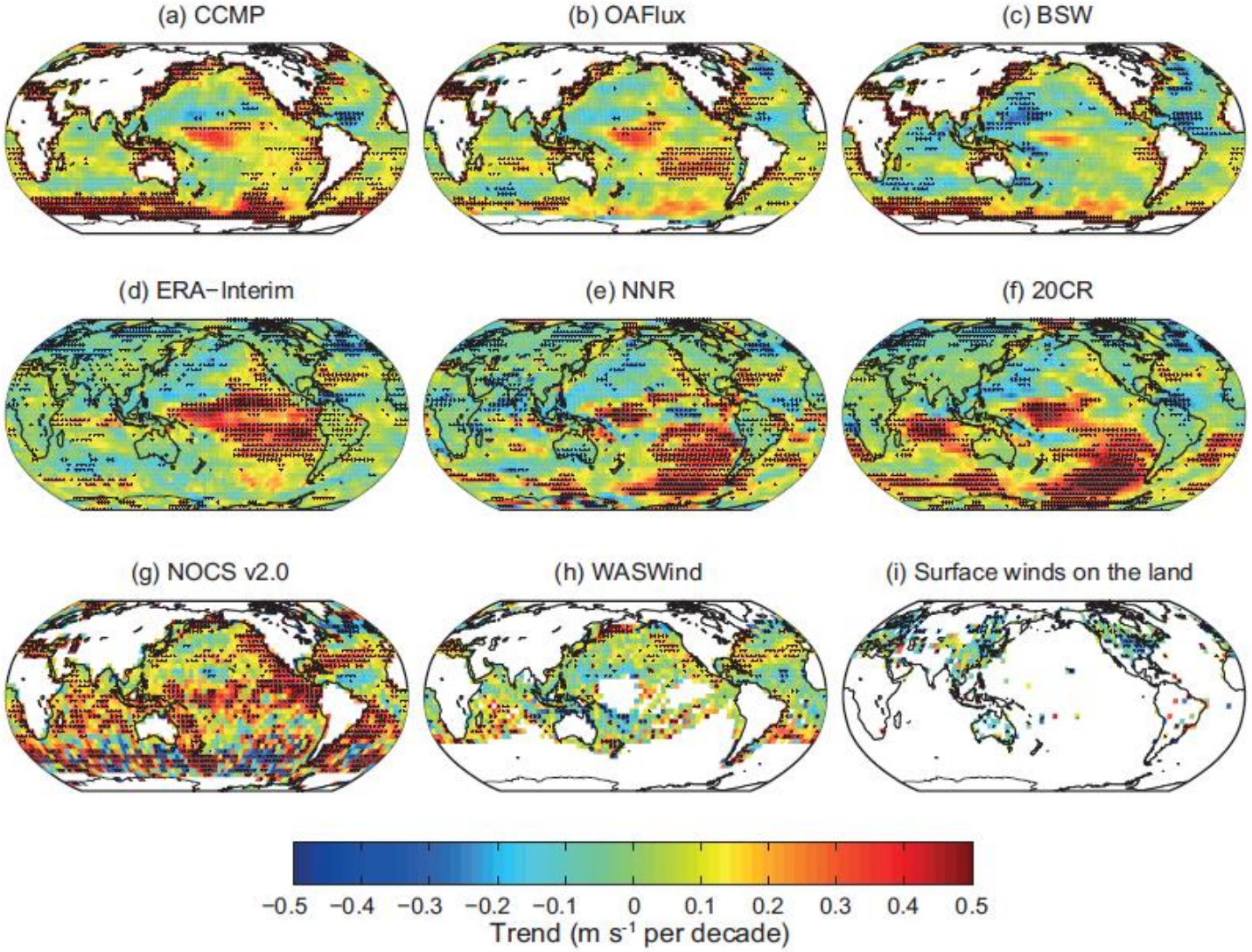


**Figure 2.38 |** Trends in surface wind speed for 1988–2010. Shown in the top row are data sets based on the satellite wind observations: (a) Cross-Calibrated Multi-Platform wind product (CCMP; Atlas et al., 2011); (b) wind speed from the Objectively Analyzed Air-Sea Heat Fluxes data set, release 3 (OAFlux); (c) Blended Sea Winds (BSW; Zhang et al., 2006); in the middle row are data sets based on surface observations: (d) ERA-Interim; (e) NCEP-NCAR, v.1 (NNR); (f) 20th Century Reanalysis (20CR, Compo et al., 2011), and in the bottom row are surface wind speeds from atmospheric reanalyses: (g) wind speed from the Surface Flux Data set, v.2, from NOC, Southampton, UK (Berry and Kent, 2009); (h) Wave- and Anemometer-based Sea Surface Wind (WASWind; Tokinaga and Xie, 2011a)); and (i) Surface Winds on the Land (Vautard et al., 2010). Wind speeds correspond to 10 m heights in all products. Land station winds (panel f) are also for 10 m (but anemometer height is not always reported) except for the Australian data where they correspond to 2 m height. To improve readability of plots, all data sets (including land station data) were averaged to the 4° × 4° uniform longitude-latitude grid. Trends were computed for the annually averaged timeseries of 4° × 4° cells. For all data sets except land station data, an annual mean was considered available only if monthly means for no less than eight months were available in that calendar year. Trend values were computed only if no less than 17 years had values and at least 1 year was available among the first and last 3 years of the period. White areas indicate incomplete or missing data. Black plus signs (+) indicate grid boxes where trends are significant (i.e., a trend of zero lies outside the 90% confidence interval).

# Zmiany w oceanach

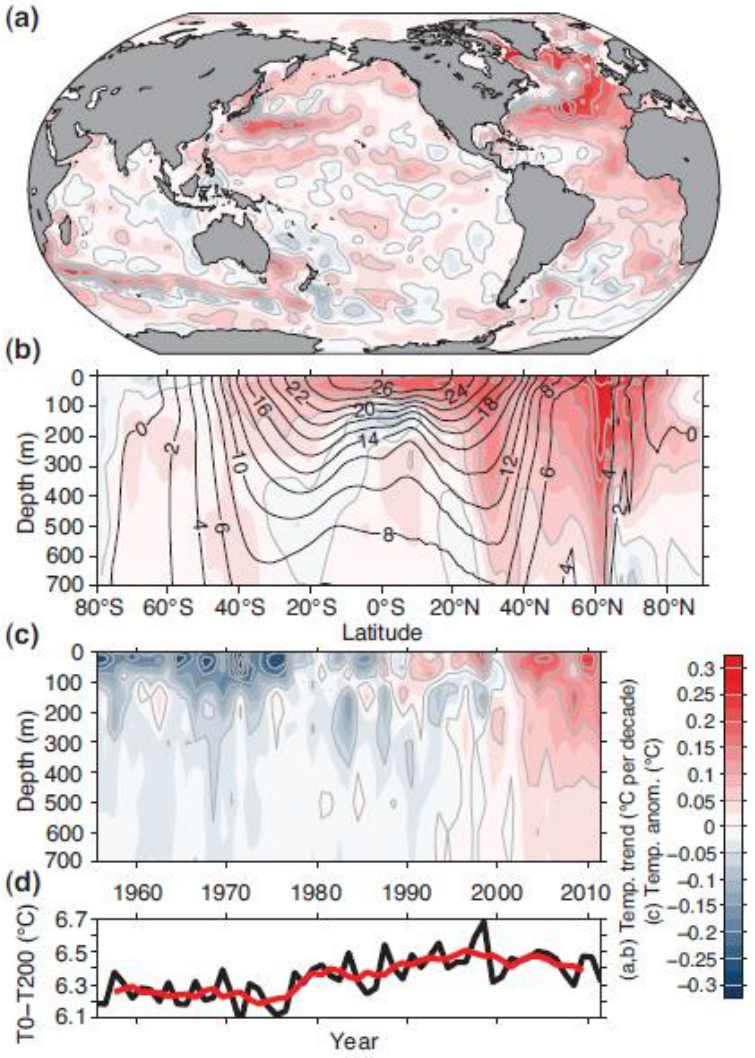


**Figure 3.1 |** (a) Depth-averaged 0 to 700 m temperature trend for 1971–2010 (longitude vs. latitude, colours and grey contours in degrees Celsius per decade). (b) Zonally averaged temperature trends (latitude vs. depth, colours and grey contours in degrees Celsius per decade) for 1971–2010 with zonally averaged mean temperature over-plotted (black contours in degrees Celsius). (c) Globally averaged temperature anomaly (time vs. depth, colours and grey contours in degrees Celsius) relative to the 1971–2010 mean. (d) Globally averaged temperature difference between the ocean surface and 200 m depth (black: annual values, red: 5-year running mean). All panels are constructed from an update of the annual analysis of Levitus et al. (2009).

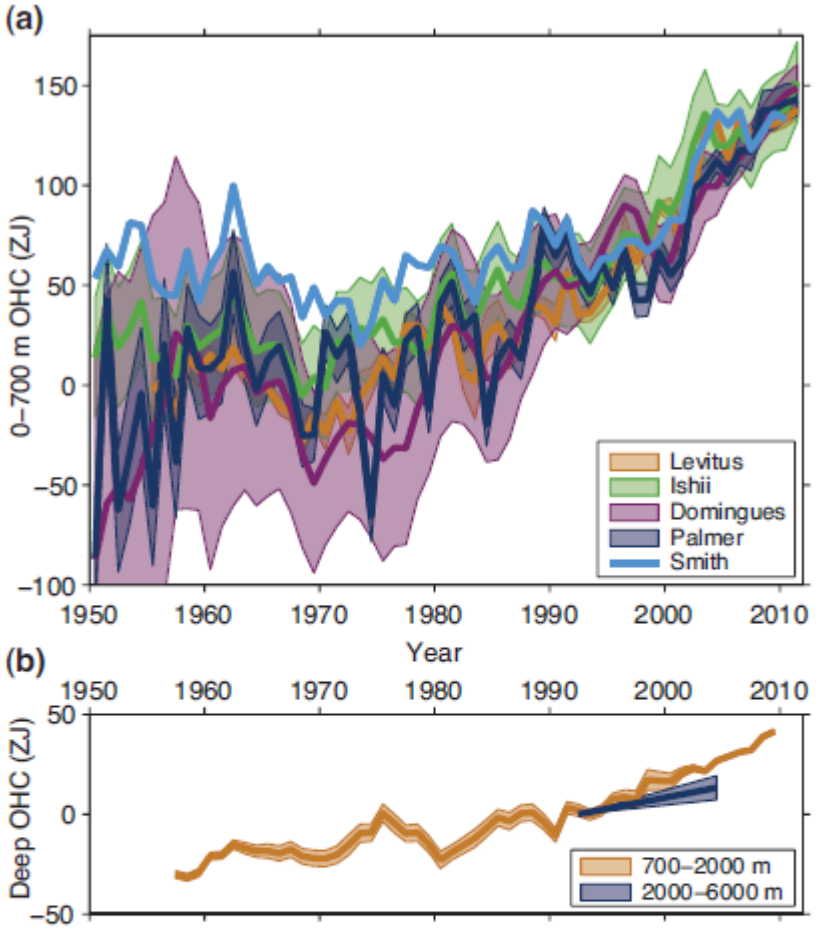


**Figure 3.2: |** (a) Observation-based estimates of annual global mean upper (0 to 700 m) ocean heat content in ZJ (1 ZJ = $10^{21}$ Joules) updated from (see legend): Levitus et al. (2012), Ishii and Kimoto (2009), Domingues et al. (2008), Palmer et al. (2007) and Smith and Murphy (2007). Uncertainties are shaded and plotted as published (at the one standard error level, except one standard deviation for Levitus, with no uncertainties provided for Smith). Estimates are shifted to align for 2006–2010, 5 years that are well measured by Argo, and then plotted relative to the resulting mean of all curves for 1971, the starting year for trend calculations. (b) Observation-based estimates of annual 5-year running mean global mean mid-depth (700 to 2000 m) ocean heat content in ZJ (Levitus et al., 2012) and the deep (2000 to 6000 m) global ocean heat content trend from 1992 to 2005 (Purkey and Johnson, 2010), both with one standard error uncertainties shaded (see legend).

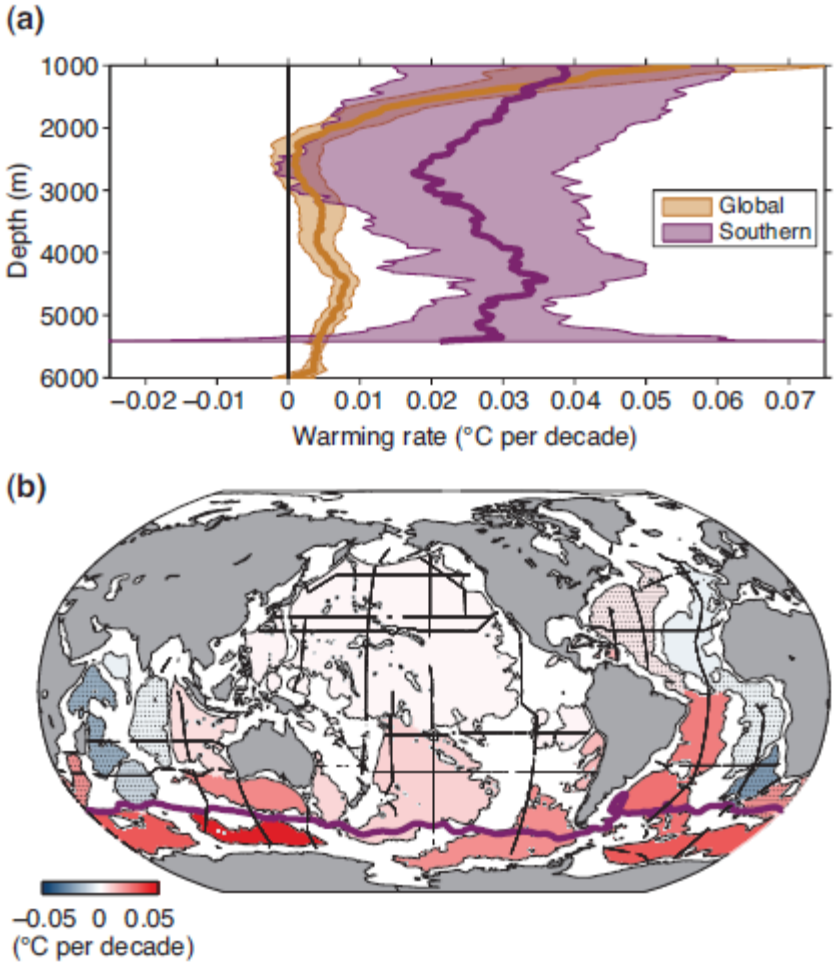


**Figure 3.3 |** (a) Areal mean warming rates (ºC per decade) versus depth (thick lines) with 5 to 95% confidence limits (shading), both global (orange) and south of the Sub-Antarctic Front (purple), centred on 1992–2005. (b) Mean warming rates (ºC per decade) below 4000 m (colour bar) estimated for deep ocean basins (thin black outlines), centred on 1992–2005. Stippled basin warming rates are not significantly different from zero at 95% confidence. The positions of the Sub-Antarctic Front (purple line) and the repeat oceanographic transects from which these warming rates are estimated (thick black lines) also shown. (Data from Purkey and Johnson, 2010.)

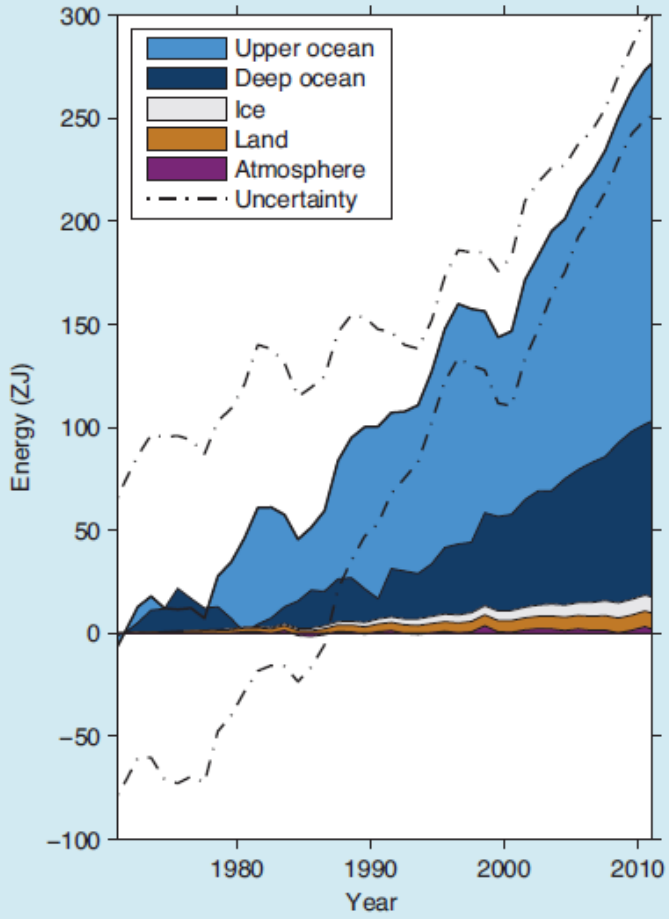


**Box 3.1, Figure 1 |** Plot of energy accumulation in ZJ (1 ZJ = $10^{21}$ J) within distinct components of the Earth's climate system relative to 1971 and from 1971 to 2010 unless otherwise indicated. See text for data sources. Ocean warming (heat content change) dominates, with the upper ocean (light blue, above 700 m) contributing more than the mid-depth and deep ocean (dark blue, below 700 m; including below 2000 m estimates starting from 1992). Ice melt (light grey; for glaciers and ice caps, Greenland and Antarctic ice sheet estimates starting from 1992, and Arctic sea ice estimate from 1979 to 2008); continental (land) warming (orange); and atmospheric warming (purple; estimate starting from 1979) make smaller contributions. Uncertainty in the ocean estimate also dominates the total uncertainty (dot-dashed lines about the error from all five components at 90% confidence intervals).

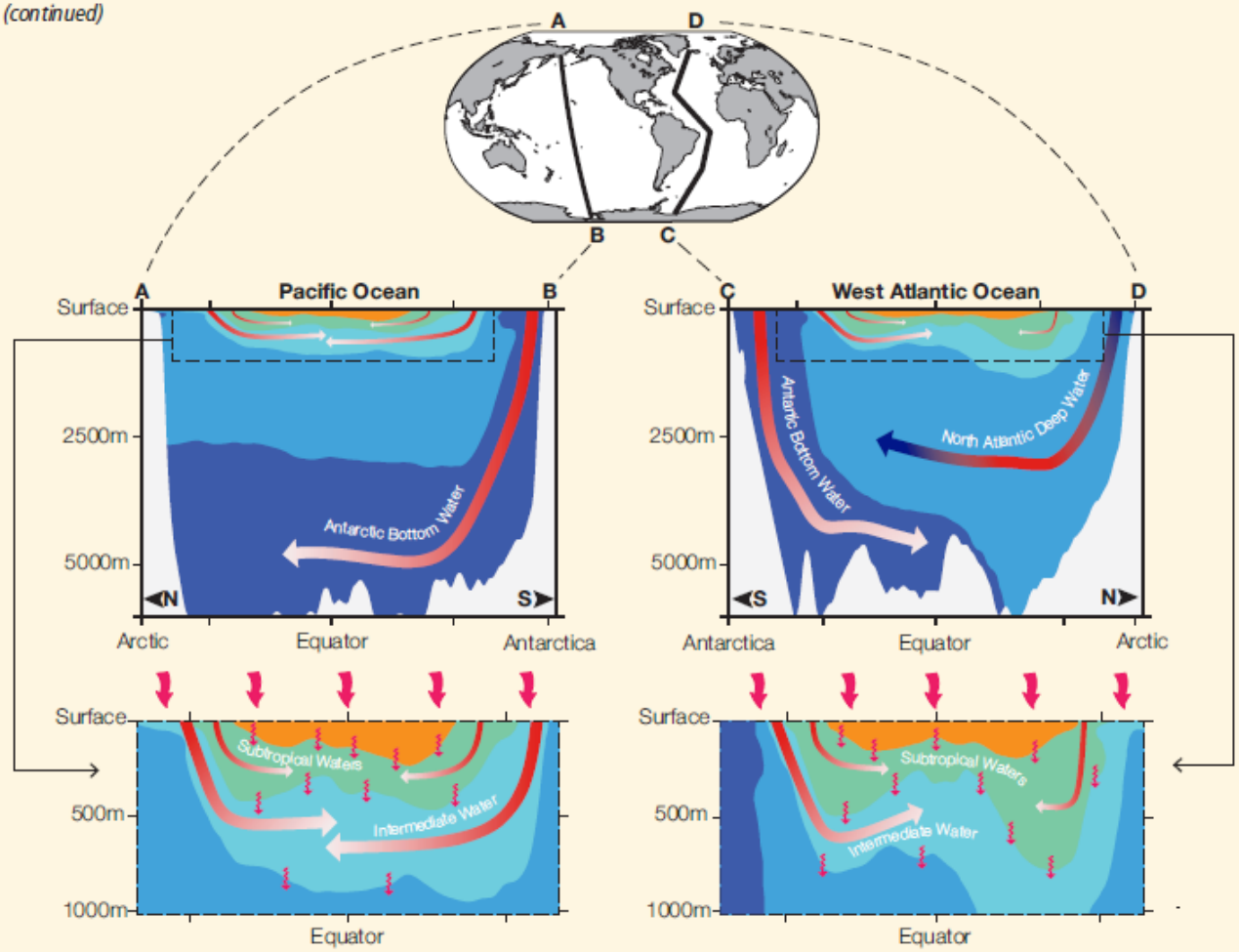


**FAQ 3.1, Figure 1 |** Ocean heat uptake pathways. The ocean is stratified, with the coldest, densest water in the deep ocean (upper panels: use map at top for orientation). Cold Antarctic Bottom Water (dark blue) sinks around Antarctica then spreads northward along the ocean floor into the central Pacific (upper left panel: red arrows fading to white indicate stronger warming of the bottom water most recently in contact with the ocean surface) and western Atlantic oceans (upper right panel), as well as the Indian Ocean (not shown). Less cold, hence lighter, North Atlantic Deep Water (lighter blue) sinks in the northern North Atlantic Ocean (upper right panel: red and blue arrow in the deep water indicates decadal warming and cooling), then spreads south above the Antarctic Bottom Water. Similarly, in the upper ocean (lower left panel shows Pacific Ocean detail, lower right panel the Atlantic), cool Intermediate Waters (cyan) sink in sub-polar regions (red arrows fading to white indicating warming with time), before spreading toward the equator under warmer Subtropical Waters (green), which in turn sink (red arrows fading to white indicate stronger warming of the intermediate and subtropical waters most recently in contact with the surface) and spread toward the equator under tropical waters, the warmest and lightest (orange) in all three oceans. Excess heat or cold entering at the ocean surface (top curvy red arrows) also mixes slowly downward (sub-surface wavy red arrows).

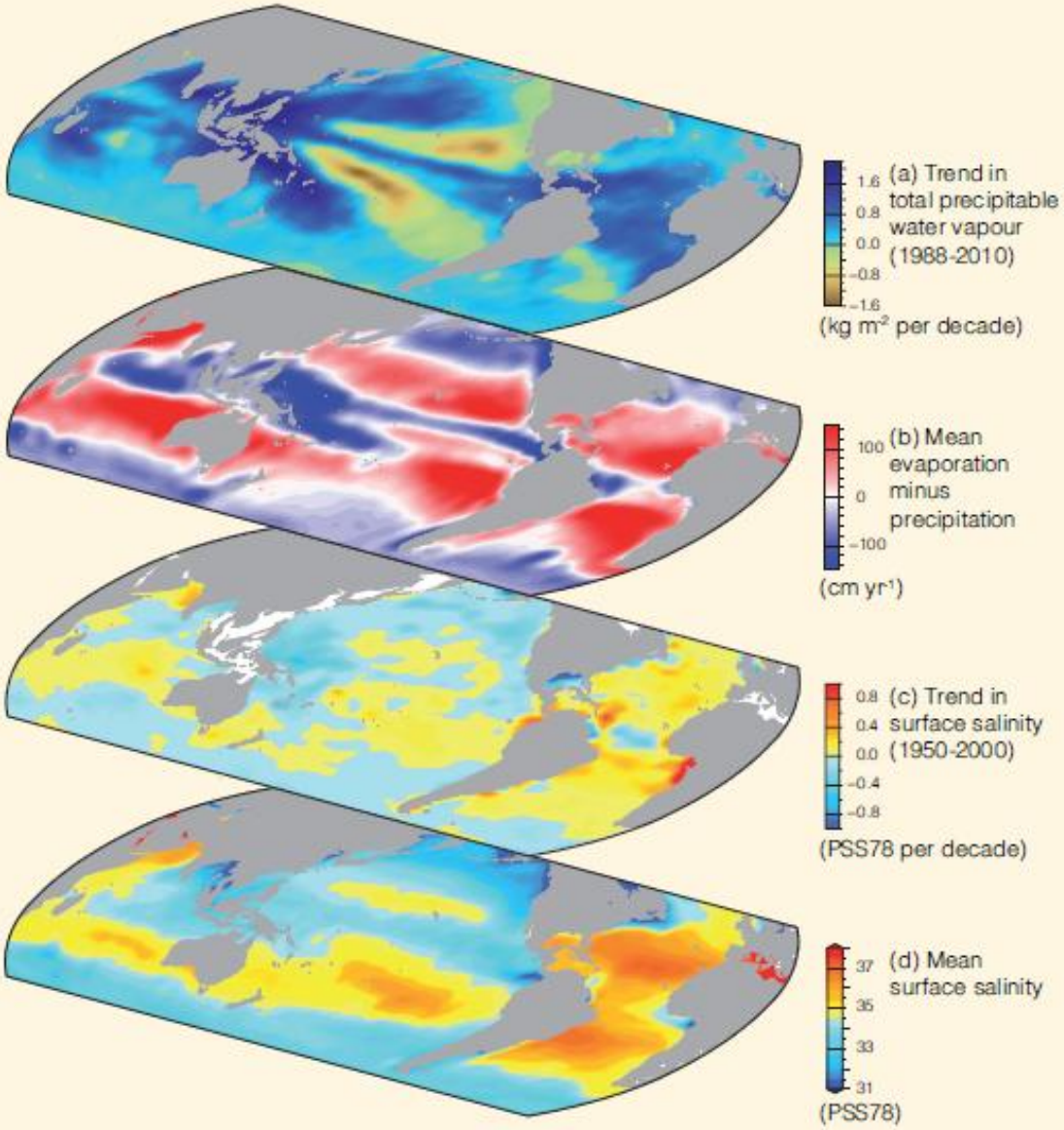


**FAQ 3.2, Figure 1 |** Changes in sea surface salinity are related to the atmospheric patterns of evaporation minus precipitation (E − P) and trends in total precipitable water: (a) Linear trend (1988–2010) in total precipitable water (water vapor integrated from the Earth's surface up through the entire atmosphere) (kg m$^{-2}$ per decade) from satellite observations (Special Sensor Microwave Imager) (after Wentz et al., 2007) (blues: wetter; yellows: drier). (b) The 1979–2005 climatological mean net E −P (cm yr$^{-1}$) from meteorological reanalysis (National Centers for Environmental Prediction/National Center for Atmospheric Research; Kalnay et al., 1996) (reds: net evaporation; blues: net precipitation). (c) Trend (1950–2000) in surface salinity (PSS78 per 50 years) (after Durack and Wijffels, 2010) (blues freshening; yellows-reds saltier). (d) The climatological-mean surface salinity (PSS78) (blues: <35; yellows–reds: >35).

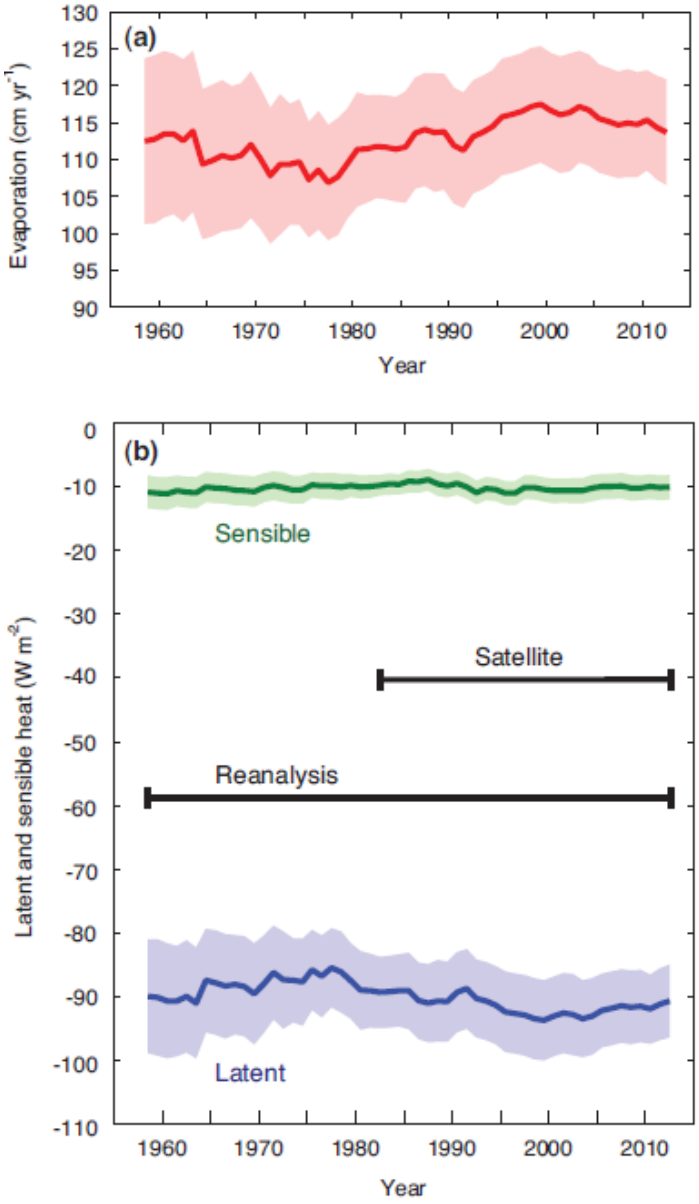


**Figure 3.6 |** Time series of annual mean global ocean average evaporation (red line, a), sensible heat flux (green line, b) and latent heat flux (blue line, b) from 1958 to 2012 determined by Yu from a revised and updated version of the original OAFlux data set Yu and Weller (2007). Shaded bands show uncertainty estimates and the black horizontal bars in (b) show the time periods for which reanalysis output and satellite observations were employed in the OAFlux analysis; they apply to both panels.

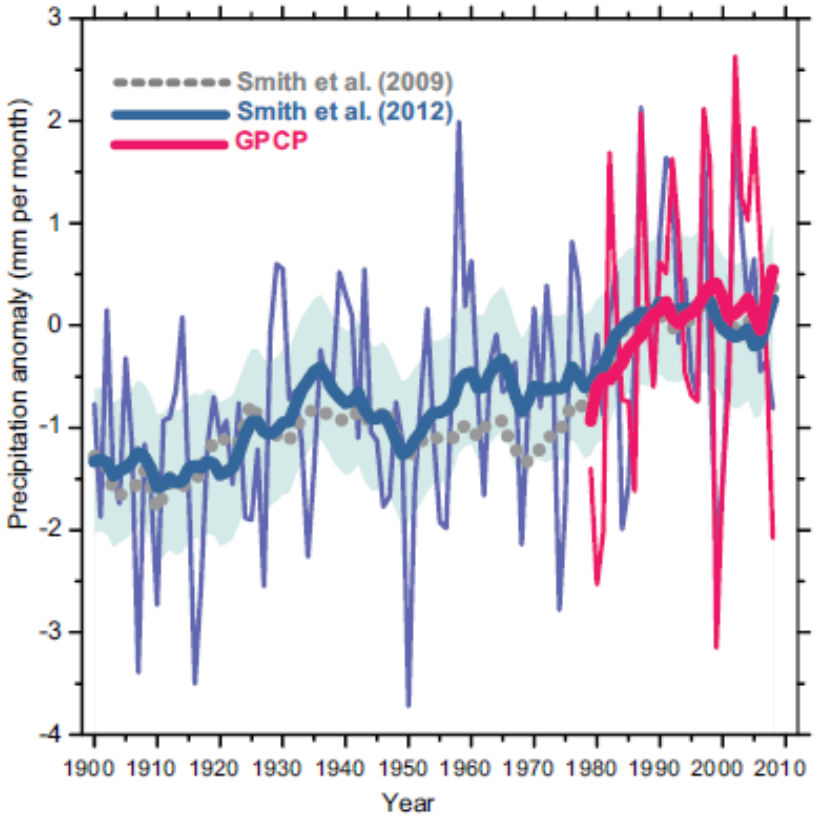


**Figure 3.7 |** Long-term reconstruction of ocean precipitation anomaly averaged over 75°S to 75°N from Smith et al. (2012): Annual values, thin blue line; low-pass filtered (15-year running mean) values, bold blue line with uncertainty estimates (shading). Smith et al. (2009) low-pass filtered values, dotted grey line. Also shown is the corresponding GPCPv2.2 derived ocean precipitation anomaly time series averaged over the same latitudinal range (annual values, thin magenta line; low-pass filtered values, bold magenta line); note Smith et al. (2012) employed an earlier version of the GPCP data set leading to minor differences relative to the published time series in their paper. Precipitation anomalies were taken relative to the 1979–2008 period.

# Zmiany poziomu oceanu, wybrane regiony

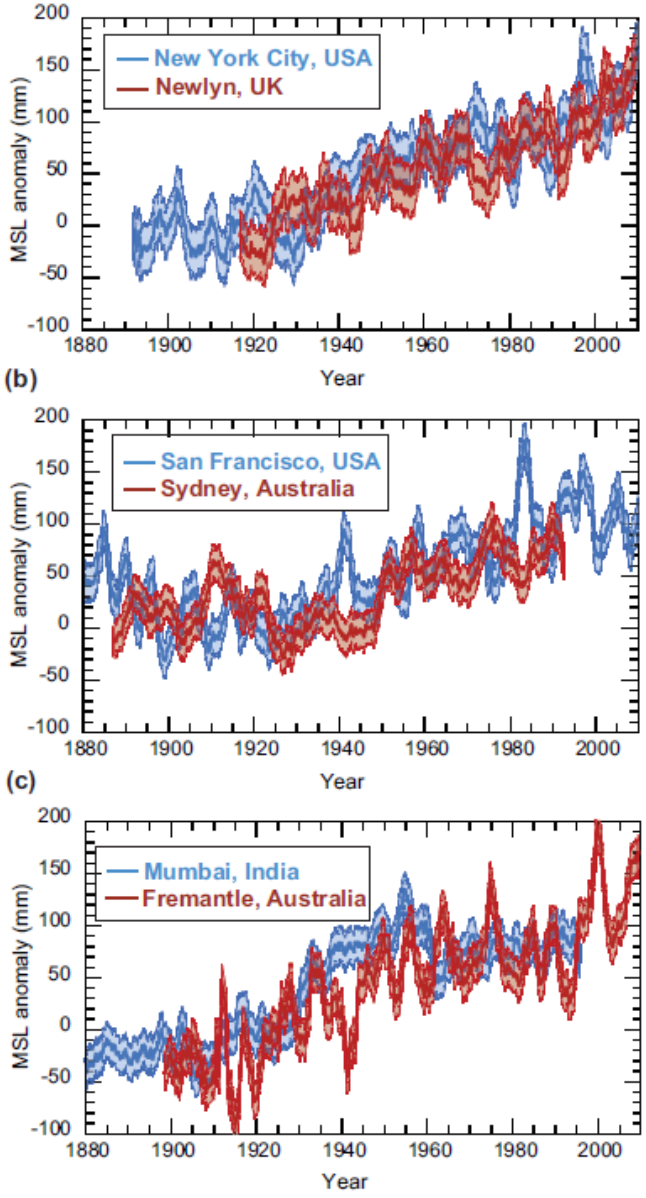


**Figure 3.12** | 3-year running mean sea level anomalies (in millimeters) relative to 1900–1905 from long tide gauge records representing each ocean basin from the Permanent Service for Mean Sea Level (PSMSL) (http://www.psmsl.org), obtained May 2011. Data have been corrected for Glacial Isostatic Adjustment (GIA) (Peltier, 2004), using values available from http://www.psmsl.org/train_and_info/geo_signals/gia/peltier/. Error bars reflect the 5 to 95% confidence interval, based on the residual monthly variability about the 3-year running mean.

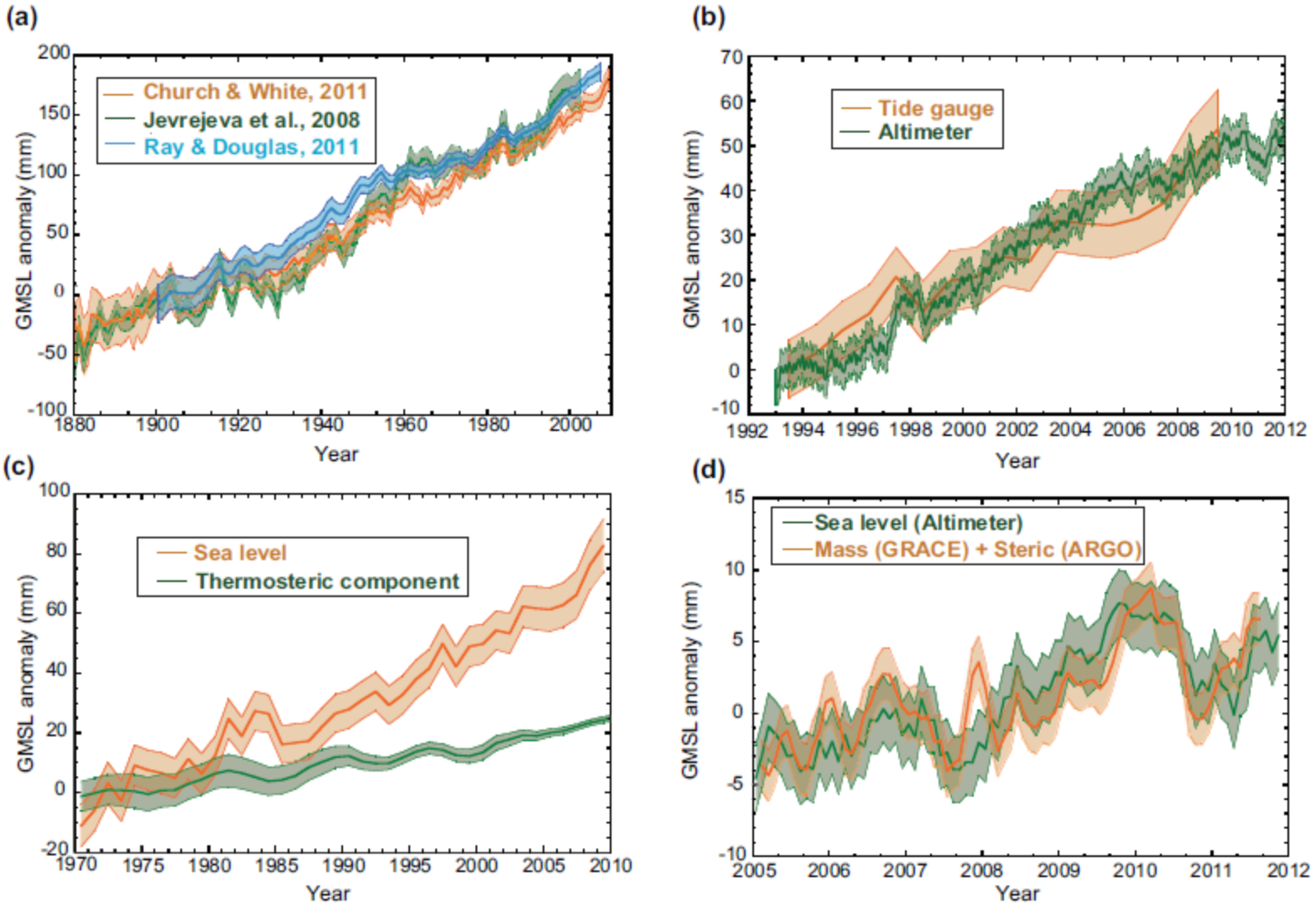


**Figure 3.13 |** Global mean sea level anomalies (in mm) from the different measuring systems as they have evolved in time, plotted relative to 5-year mean values that start at (a) 1900, (b) 1993, (c) 1970 and (d) 2005. (a) Yearly average GMSL reconstructed from tide gauges (1900–2010) by three different approaches (Jevrejeva et al., 2008; Church and White, 2011; Ray and Douglas, 2011). (b) GMSL (1993–2010) from tide gauges and altimetry (Nerem et al., 2010) with seasonal variations removed and smoothed with a 60-day running mean. (c) GMSL (1970–2010) from tide gauges along with the thermosteric component to 700 m (3-year running mean) estimated from in situ temperature profiles (updated from Domingues et al., 2008). (d) The GMSL (nonseasonal) from altimetry and that computed from the mass component (GRACE) and steric component (Argo) from 2005 to 2010 (Leuliette and Willis, 2011), all with a 3-month running mean filter. All uncertainty bars are one standard error as reported by the authors. The thermosteric component is just a portion of total sea level, and is not expected to agree with total sea level.

**Table 3.1 |** Estimated trends in GMSL and components over different periods from representative time-series. Trends and uncertainty have been estimated from a time series provided by the authors using ordinary least squares with the uncertainty representing the 90% confidence interval. The model fit for yearly averaged time series was a bias + trend; the model fit for monthly and 10-day averaged data was a bias + trend + seasonal sinusoids. Uncertainty accounts for correlations in the residuals.

| Quantity | Period | Trend (mm $yr^{-1}$) | Source | Resolution |
|---|---|---|---|---|
| GMSL | 1901–2010 | 1.7 [1.5 to 1.9] | Tide Gauge Reconstruction (Church and White, 2011) | Yearly |
| | 1901–1990 | 1.5 [1.3 to 1.7] | Tide Gauge Reconstruction (Church and White, 2011) | Yearly |
| | 1971–2010 | 2.0 [1.7 to 2.3] | Tide Gauge Reconstruction (Church and White, 2011) | Yearly |
| | 1993–2010 | 2.8 [2.3 to 3.3] | Tide Gauge Reconstruction (Church and White, 2011) | Yearly |
| | 1993–2010 | 3.2 [2.8 to 3.6][a] | Altimetry (Nerem et al., 2010) time-series | 10-Day |
| Thermosteric Component (upper 700 m) | 1971–2010 | 0.6 [0.4 to 0.8] | XBT Reconstruction (updated from Domingues et al., 2008) | 3-Year running means |
| | 1993–2010 | 0.8 [0.5 to 1.1] | XBT Reconstruction (updated from Domingues et al., 2008) | 3-Year running means |
| Thermosteric Component (700 to 2000 m) | 1971–2010 | 0.1 [0 to 0.2] | Objective mapping of historical temperature data (Levitus et al., 2012) | 5-Year averages |
| | 1993–2010 | 0.2 [0.1 to 0.3] | Objective mapping of historical temperature data (Levitus et al., 2012) | 5-Year averages |
| Thermosteric Component (below 2000 m) | 1992–2005 | 0.11 [0.01 to 0.21][b] | Deep hydrographic sections (Purkey and Johnson, 2010) | Trend only |
| Thermosteric Component (whole depth) | 1971–2010 | 0.8 [0.5 to 1.1][c] | Combination of estimates from 0 to 700 m, 700 to 2000 m, and below 2000 m[c] | Trend only |
| | 1993–2010 | 1.1 [0.8 to 1.4][c] | Combination of estimates from 0–700 m, 700 to 2000 m, and below 2000 m[c] | Trend only |

Notes:

[a] Uncertainty estimated from fit to Nerem et al. (2010) time series and includes potential systematic error owing to drift of altimeter, estimated to be ±0.4 mm $yr^{-1}$ (Beckley et al., 2010; Nerem et al., 2010), applied as the root-sum-square (RSS) with the least squares error estimate. The uncertainty in drift contains uncertainty in the reference frame, orbit and instrument.

[b] Trend value taken from Purkey and Johnson (2010), Table 1. Uncertainty represents the 2.5–97.5% confidence interval.

[c] Assumes no trend below 2000 m before 1 January 1992, then value from Purkey and Johnson (2010) afterwards. Uncertainty for 0 to 700 m, 700 to 2000 m and below 2000 m is assumed to be uncorrelated, and uncertainty is calculated as RSS of the uncertainty for each layer.

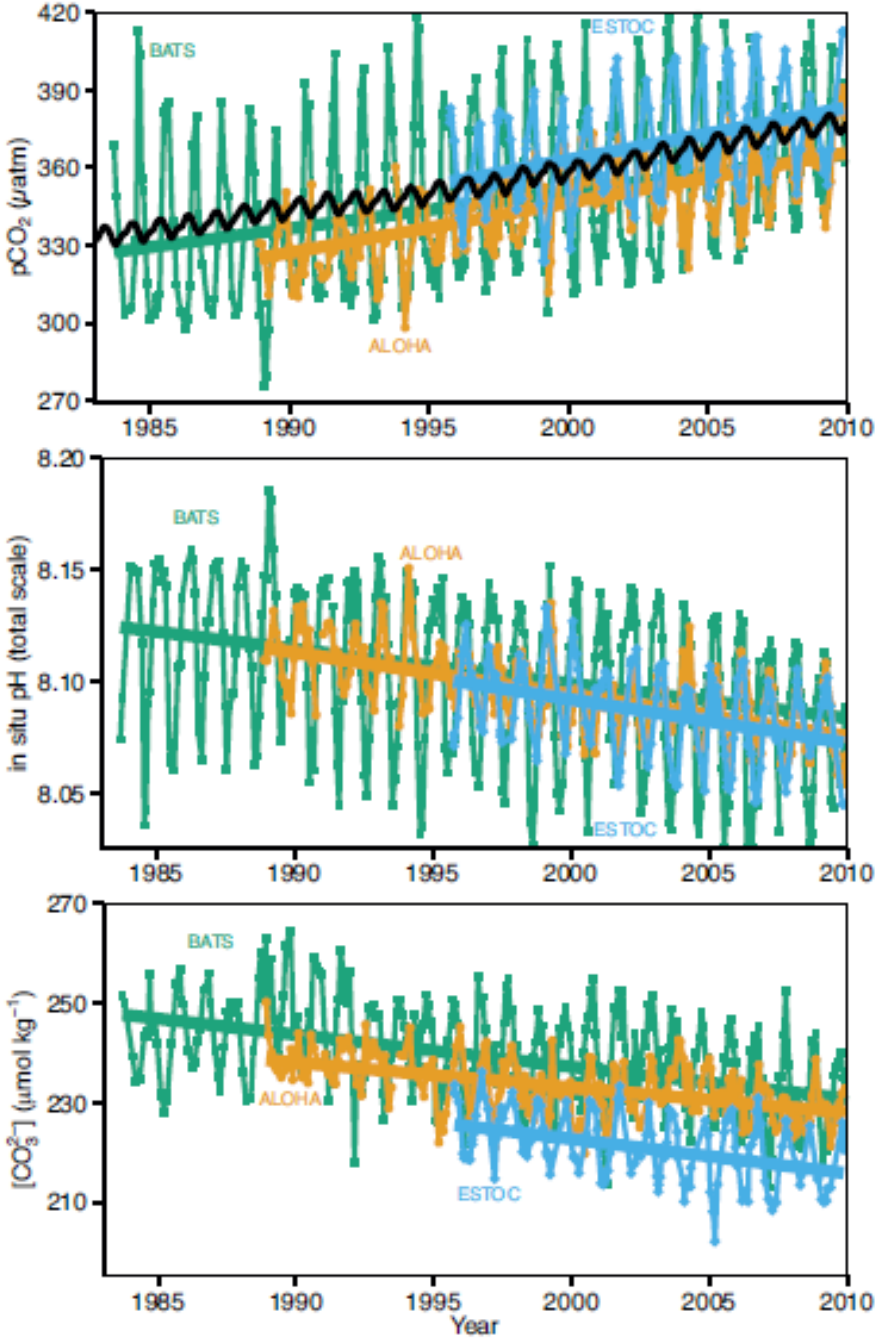


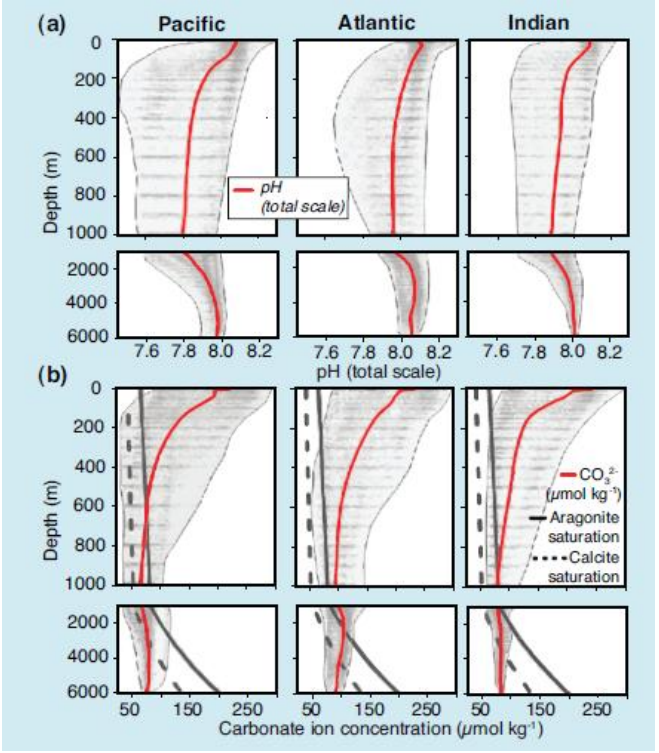


**Figure 3.18 |** Long-term trends of surface seawater $pCO_2$ (top), pH (middle) and carbonate ion (bottom) concentration at three subtropical ocean time series in the North Atlantic and North Pacific Oceans, including (a) Bermuda Atlantic Time-series Study (BATS, 31°40′N, 64°10′W; green) and Hydrostation S (32°10′, 64°30′W) from 1983 to present (updated from Bates, 2007); (b) Hawaii Ocean Time-series (HOT) at Station ALOHA (A Long-term Oligotrophic Habitat Assessment; 22°45′N, 158°00′W; orange) from 1988 to present (updated from Dore et al., 2009) and (c) European Station for Time series in the Ocean (ESTOC, 29°10′N, 15°30′W; blue) from 1994 to present (updated from González-Dávila et al., 2010). Atmospheric $pCO_2$ (black) from the Mauna Loa Observatory Hawaii is shown in the top panel. Lines show linear fits to the data, whereas Table 3.2 give results for harmonic fits to the data (updated from Orr, 2011).

# Zmiany w oceanie - podsumowanie

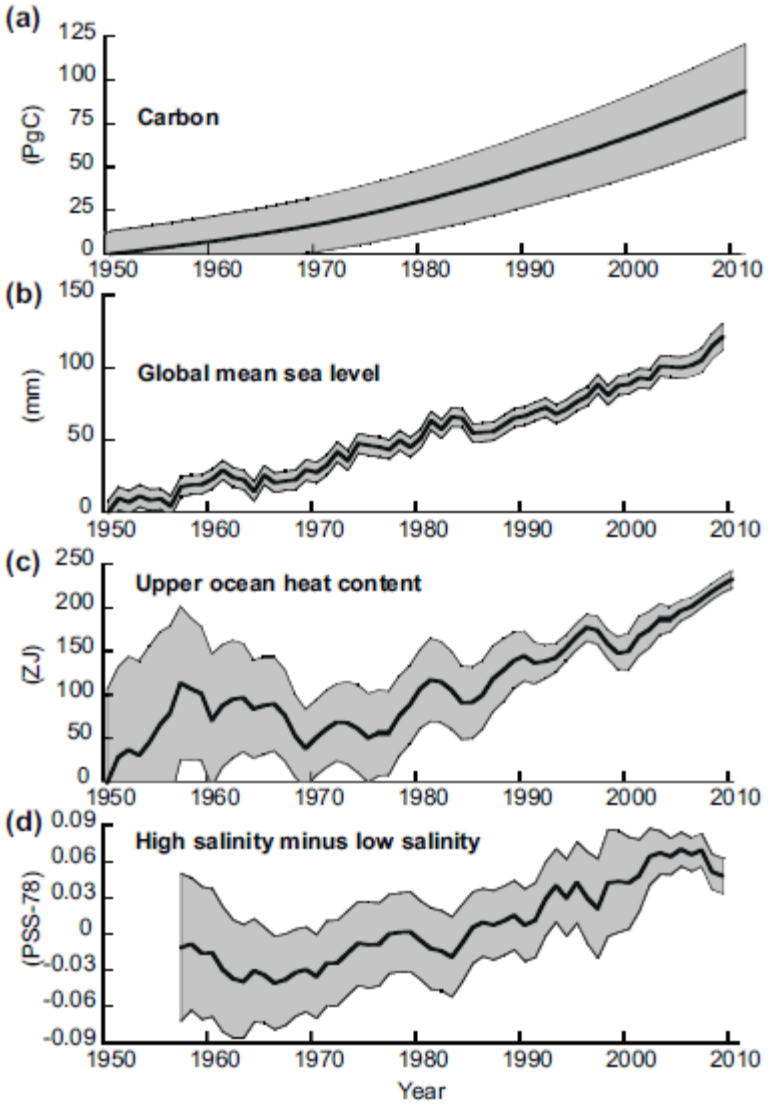


**Figure 3.21 |** Time series of changes in large-scale ocean climate properties. From top to bottom: global ocean inventory of anthropogenic carbon dioxide, updated from Khatiwala et al. (2009); global mean sea level (GMSL), from Church and White (2011); global upper ocean heat content anomaly, updated from Domingues et al. (2008); the difference between salinity averaged over regions where the sea surface salinity is greater than the global mean sea surface salinity ("High Salinity") and salinity averaged over regions values below the global mean ("Low Salinity"), from Boyer et al. (2009).

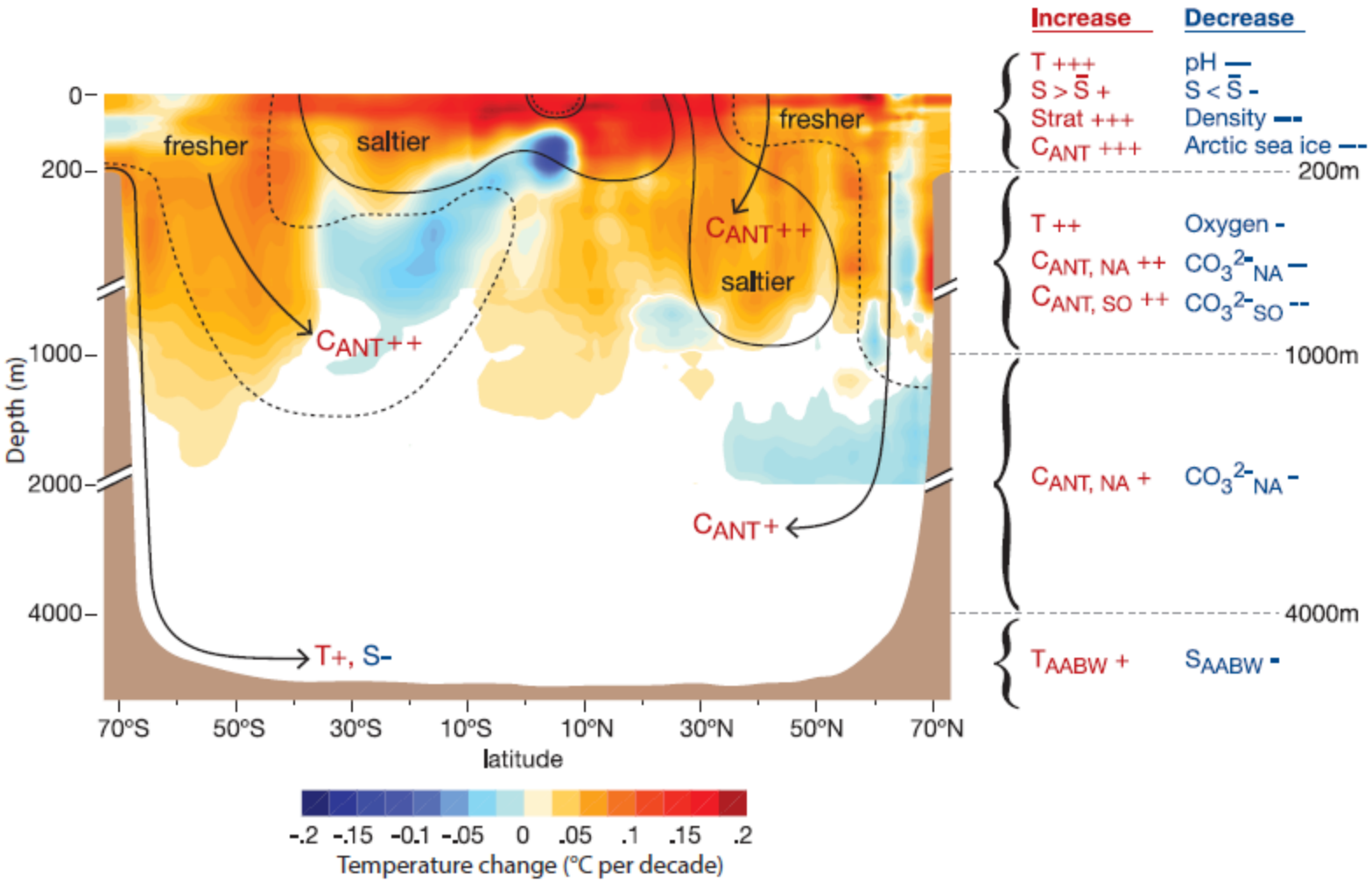


**Figure 3.22 |** Summary of observed changes in zonal averages of global ocean properties. Temperature trends (degrees Celsius per decade) are indicated in colour (red = warming, blue = cooling); salinity trends are indicated by contour lines (dashed = fresher; solid = saltier) for the upper 2000 m of the water column (50-year trends from data set of Durack and Wijffels (2010); trends significant at >90% confidence are shown). Arrows indicate primary ventilation pathways. Changes in other physical and chemical properties are summarised to the right of the figure, for each depth range (broken axes symbols delimit changes in vertical scale). Increases are shown in red, followed by a plus sign; decreases are shown in blue, followed by a minus sign; the number of + and – signs indicates the level of confidence associated with the observation of change (+++, *high confidence*; ++, *medium confidence*; +, *low confidence*). T = temperature, S = salinity, Strat = stratification, $C_{ant}$ = anthropogenic carbon, $CO_3^{2-}$ = carbonate ion, NA = North Atlantic, SO = Southern Ocean, AABW = Antarctic Bottom Water. $S > \bar{S}$ refers to the salinity averaged over regions where the sea surface salinity is greater than the global mean sea surface salinity; $S < \bar{S}$ refers to the average over regions with values below the global mean.

# Zmiany temperatury w Polsce, dane SYNOP

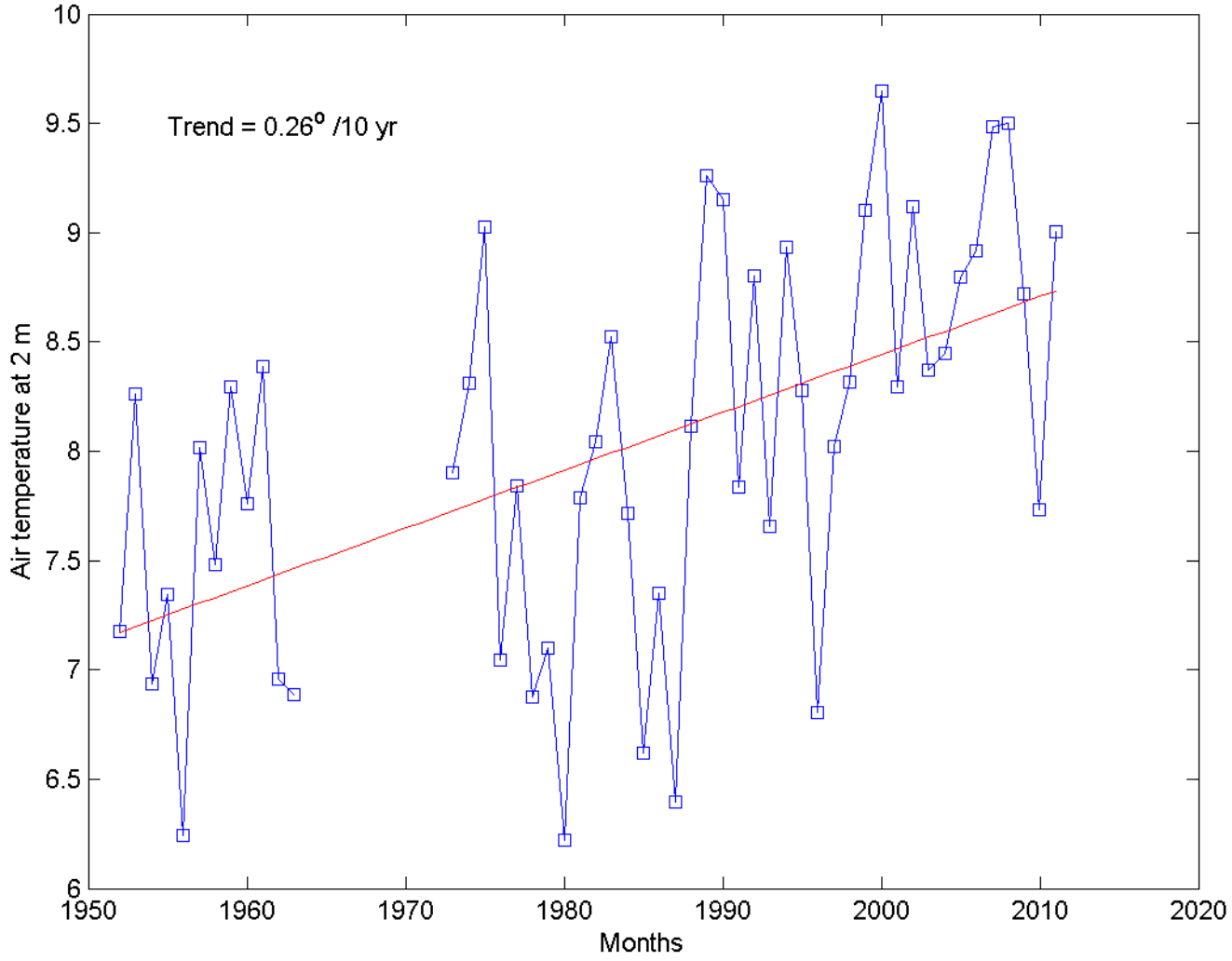

# Zmiany klimatyczne w Polsce

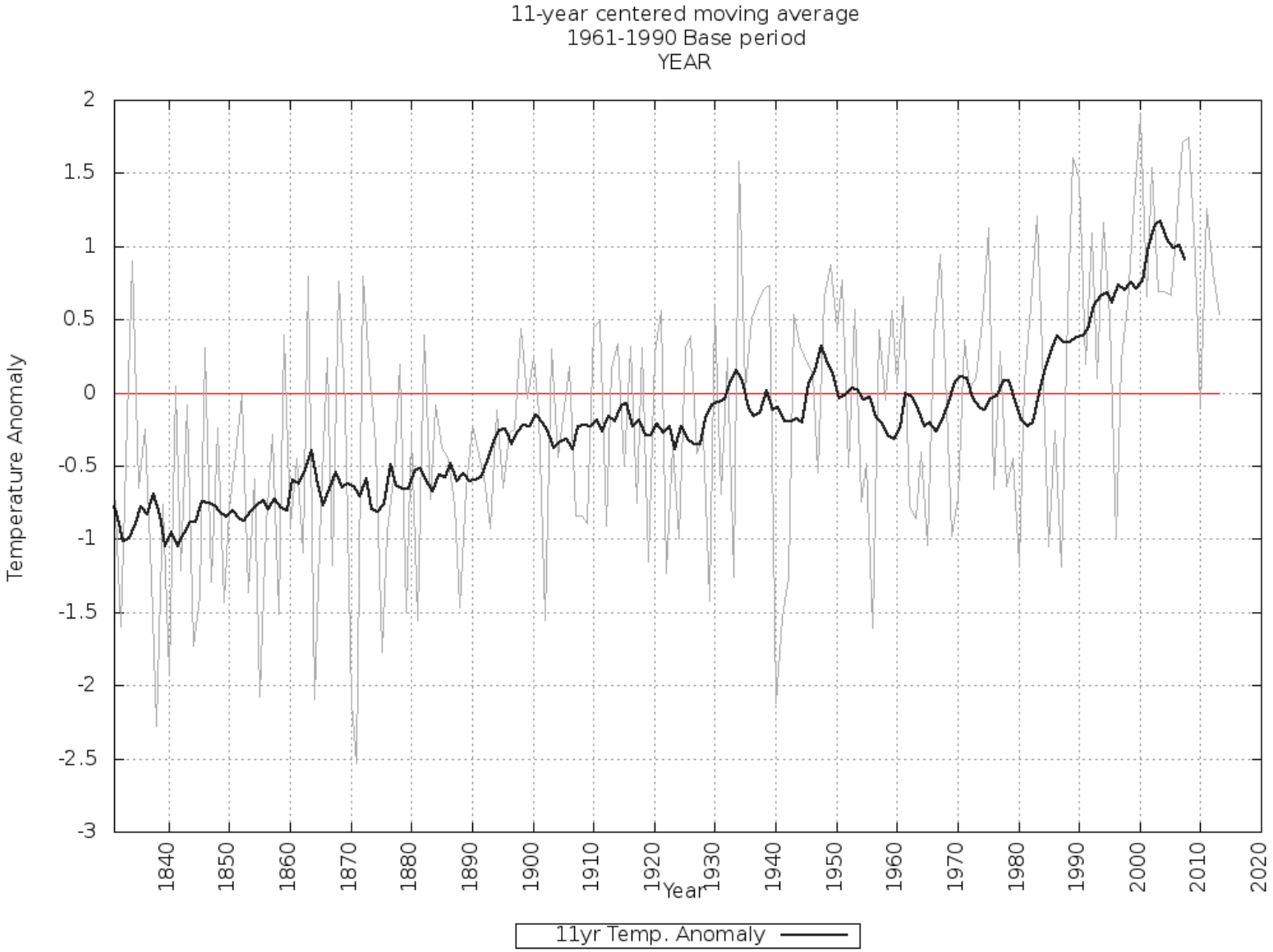


http://meteomodel.pl/klimat/poltemp/rok.png

http://meteomodel.pl/klimat/poltemp/poltemp.txt

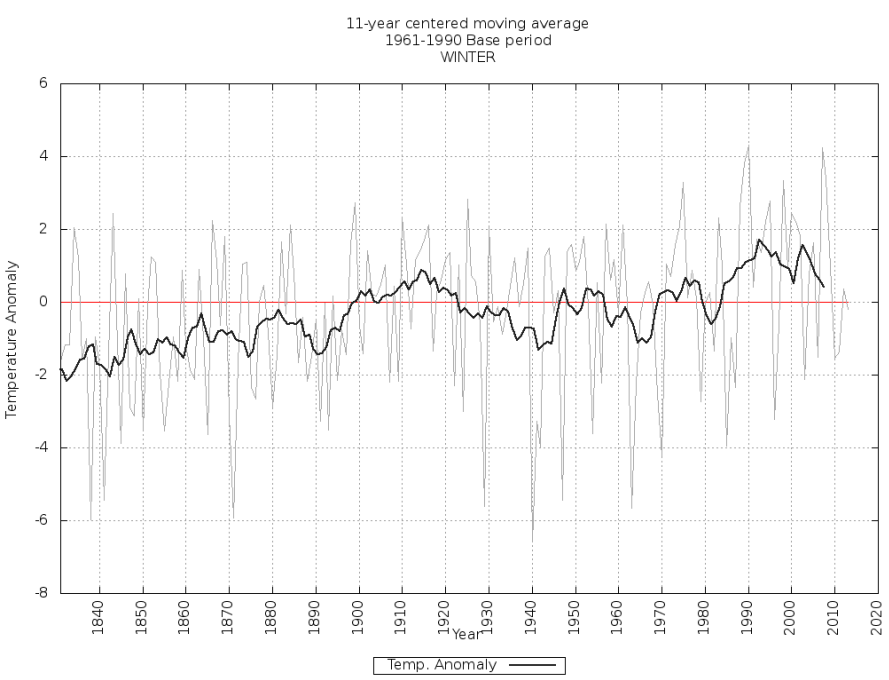


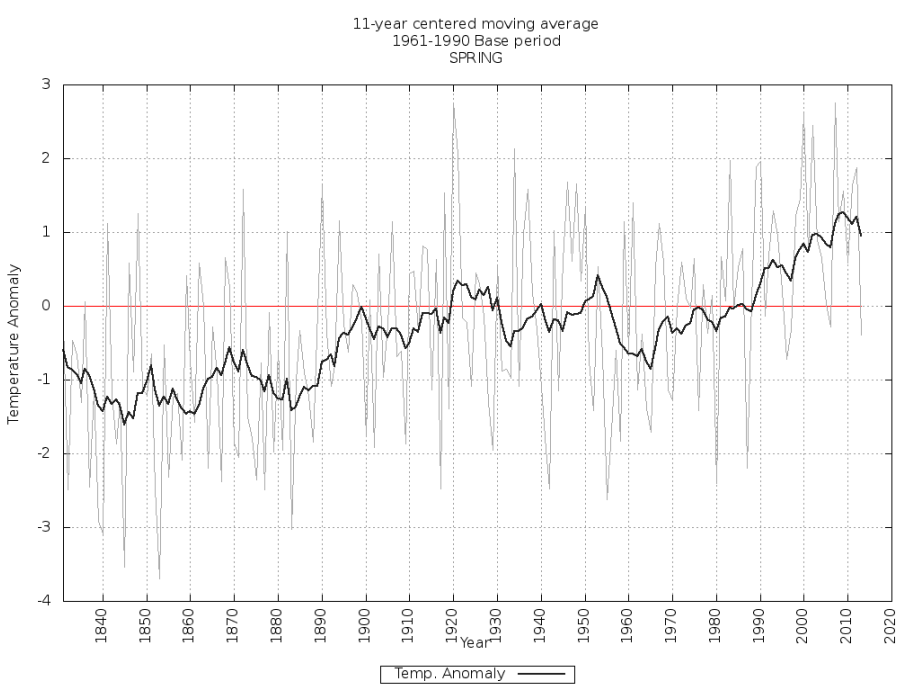


- http://meteomodel.pl/klimat/poltemp/rok.png

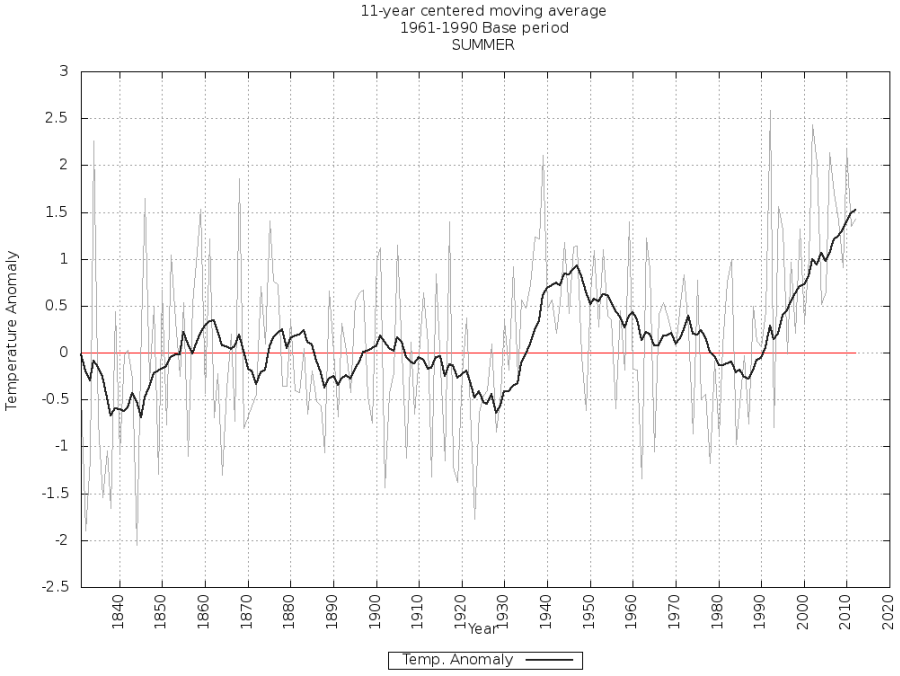


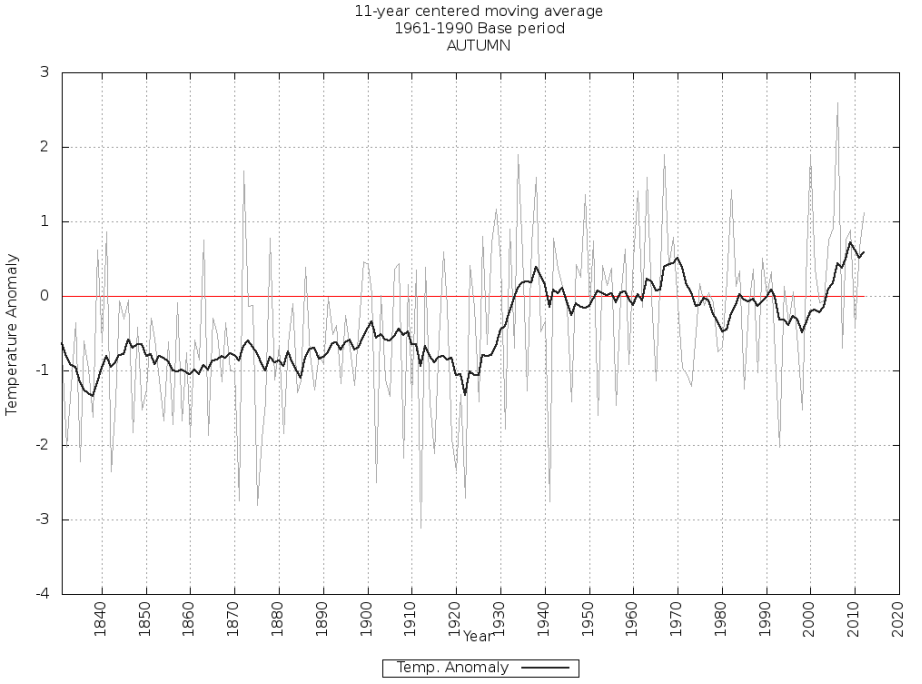

# Kriosfera

**Table 4.1 |** Representative statistics for cryospheric components indicating their general significance.

| Ice on Land | Percent of Global Land Surface[a] | Sea Level Equivalent[b] (metres) |
|---|---|---|
| Antarctic ice sheet[c] | 8.3 | 58.3 |
| Greenland ice sheet[d] | 1.2 | 7.36 |
| Glaciers[e] | 0.5 | 0.41 |
| Terrestrial permafrost[f] | 9–12 | 0.02–0.10[g] |
| Seasonally frozen ground[h] | 33 | Not applicable |
| Seasonal snow cover (seasonally variable)[i] | 1.3–30.6 | 0.001–0.01 |
| Northern Hemisphere freshwater (lake and river) ice[j] | 1.1 | Not applicable |
| **Total[k]** | **52.0–55.0%** | **~66.1** |
| **Ice in the Ocean** | **Percent of Global Ocean Area[a]** | **Volume[l] ($10^3$ km$^3$)** |
| Antarctic ice shelves | 0.45[m] | ~380 |
| Antarctic sea ice, austral summer (spring)[n] | 0.8 (5.2) | 3.4 (11.1) |
| Arctic sea ice, boreal autumn (winter/spring)[n] | 1.7 (3.9) | 13.0 (16.5) |
| Sub-sea permafrost[o] | ~0.8 | Not available |
| **Total[p]** | **5.3–7.3** | |

Notes:

[a] Assuming a global land area of 147.6 Mkm$^2$ and ocean area of 362.5 Mkm$^2$.

[b] See Glossary. Assuming an ice density of 917 kg m$^{-3}$, a seawater density of 1028 kg m$^{-3}$, with seawater replacing ice currently below sea level.

[c] Area of grounded ice sheet not including ice shelves is 12.295 Mkm$^2$ (Fretwell et al., 2013).

[d] Area of ice sheet and peripheral glaciers is 1.801 Mkm$^2$ (Kargel et al., 2012). SLE (Bamber et al., 2013).

[e] Calculated from glacier outlines (Arendt et al., 2012), includes glaciers around Greenland and Antarctica. For sources of SLE see Table 4.2.

[f] Area of permafrost excluding permafrost beneath the ice sheets is 13.2 to 18.0 Mkm$^2$ (Gruber, 2012).

[g] Value indicates the full range of estimated excess water content of Northern Hemisphere permafrost (Zhang et al., 1999).

[h] Long-term average maximum of seasonally frozen ground is 48.1 Mkm$^2$ (Zhang et al., 2003); excludes Southern Hemisphere.

[i] Northern Hemisphere only (Lemke et al., 2007).

[j] Areas and volume of freshwater (lake and river ice) were derived from modelled estimates of maximum seasonal extent (Brooks et al., 2012).

[k] To allow for areas of permafrost and seasonally frozen ground that are also covered by seasonal snow, total area excludes seasonal snow cover.

[l] Antarctic austral autumn (spring) (Kurtz and Markus, 2012); and Arctic boreal autumn (winter) (Kwok et al., 2009). For the Arctic, volume includes only sea ice in the Arctic Basin.

[m] Area is 1.617 Mkm$^2$ (Griggs and Bamber, 2011).

[n] Maximum and minimum areas taken from this assessment, Sections 4.2.2 and 4.2.3.

[o] Few estimates of the area of sub-sea permafrost exist in the literature. The estimate shown, 2.8 Mkm$^2$, has significant uncertainty attached and was assembled from other publications by Gruber (2012).

[p] Summer and winter totals assessed separately.

# Składniki kriosfery

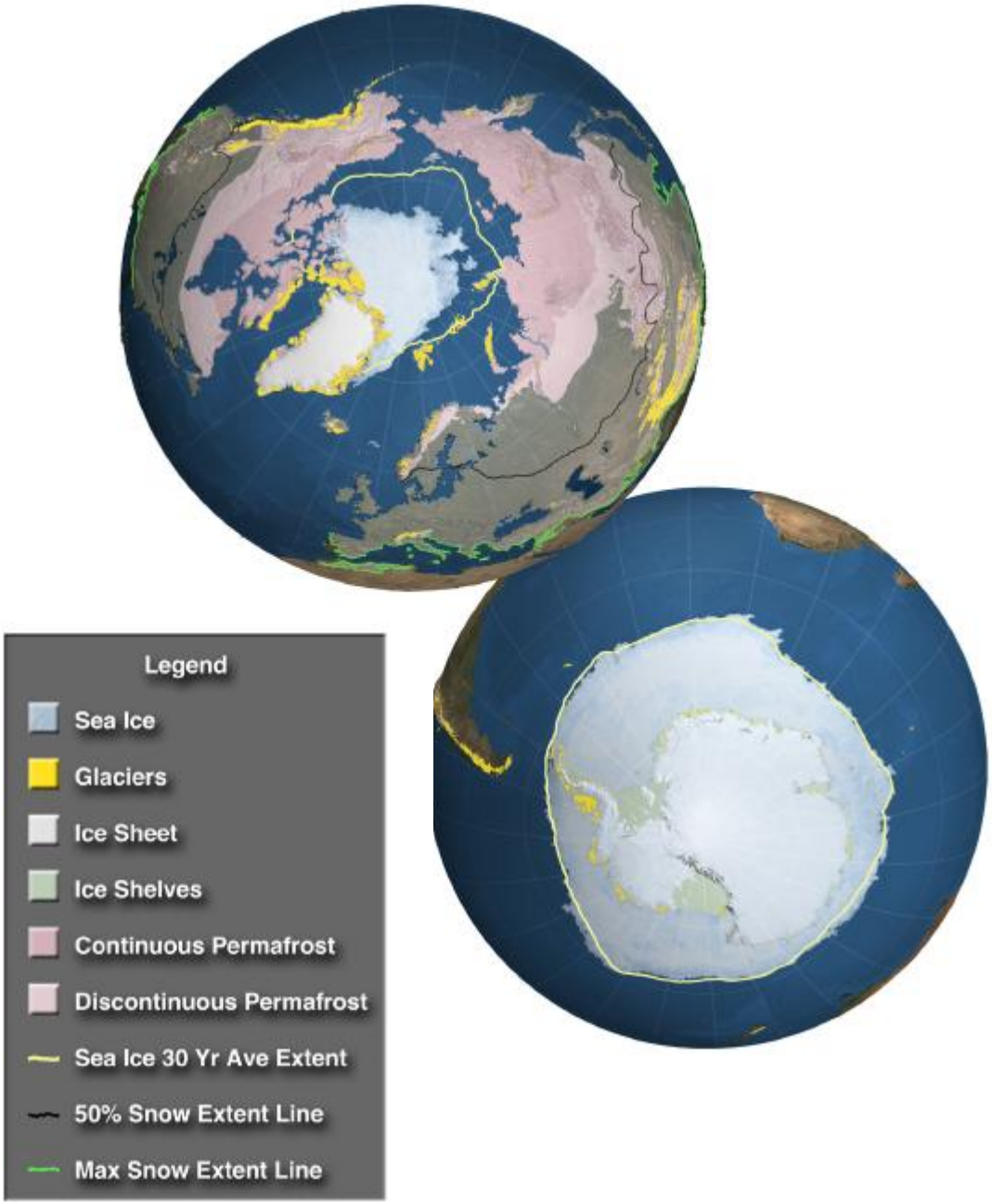

# Zmiany zasięgu lodu w Arktyce

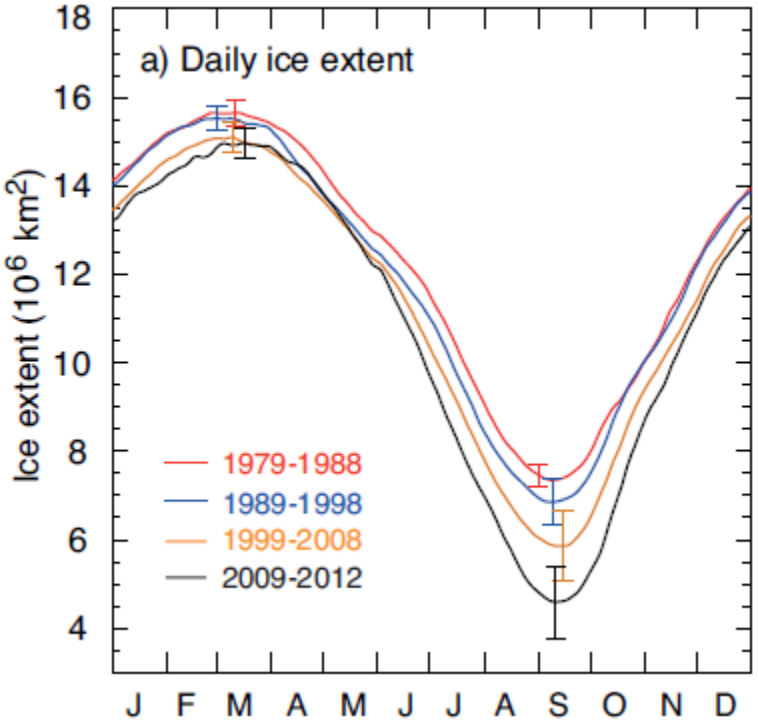


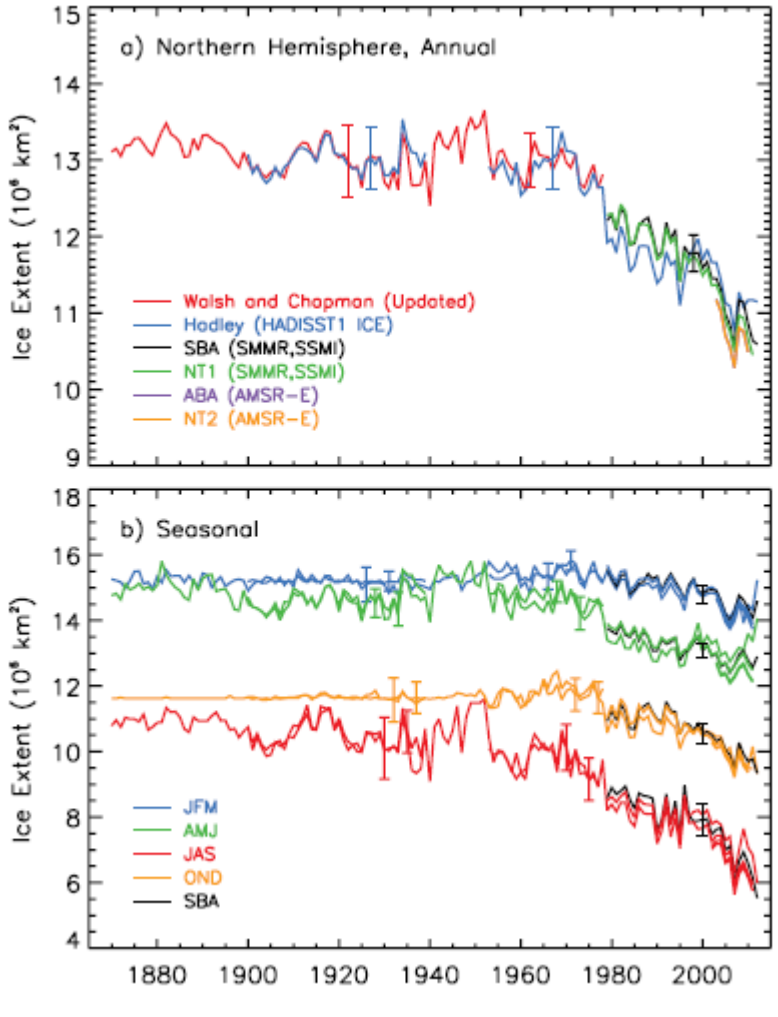

# Trendy w Arktyce

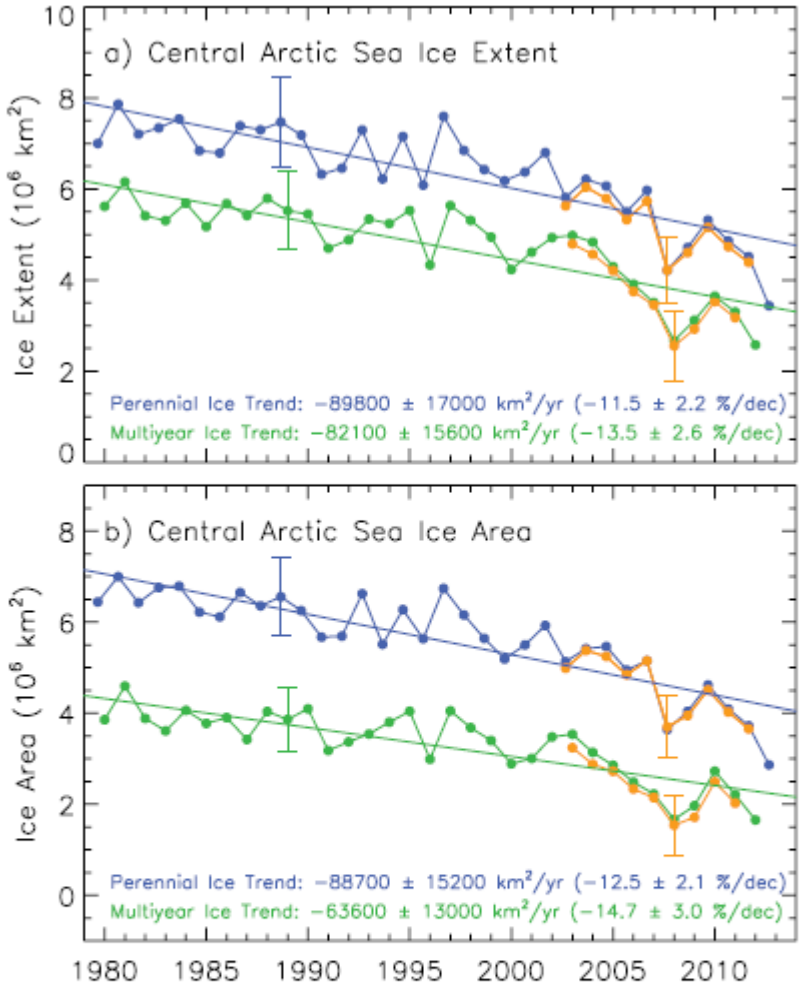


**Figure 4.4 |** Annual perennial (blue) and multi-year (green) sea ice extent (a) and sea ice area (b) in the Central Arctic from 1979 to 2012 as derived from satellite passive microwave data (updated from Comiso, 2012). Perennial ice values are derived from summer minimum ice extent, while the multi-year ice values are averages of those from December, January and February. The gold lines (after 2002) are from AMSR-E data. Uncertainties in the observations (*very likely* range) are indicated by representative error bars, and uncertainties in the trends are given (*very likely* range).

# Zmiany grubości arktycznego lodu na podstawie pomiarów z altymetrii satelitarnej.

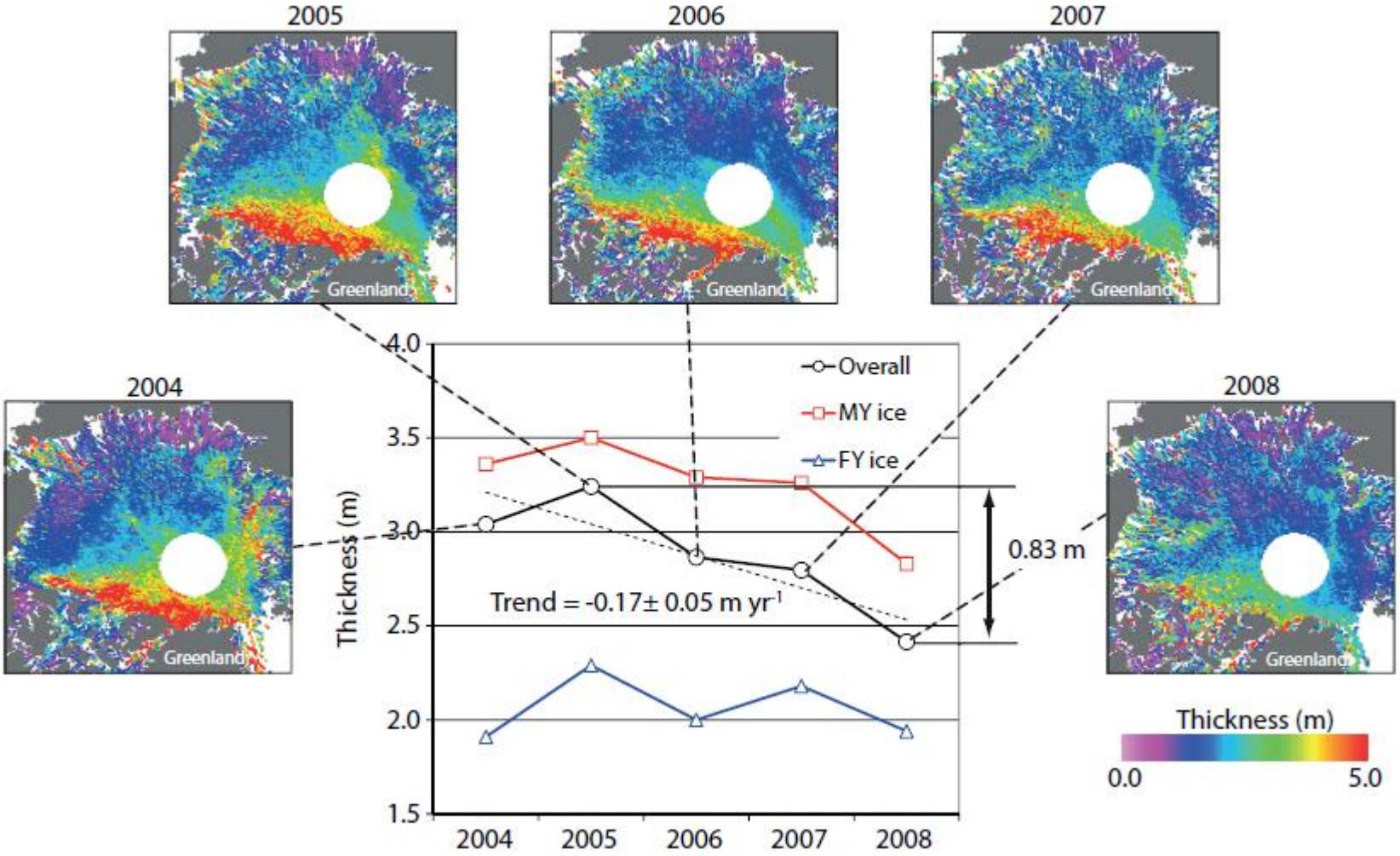


**Figure 4.5 |** The distribution of winter sea ice thickness in the Arctic and the trends in average, first-year (FY and multi-year (MY) ice thickness derived from ICESat data between 2004 and 2008 (Kwok, 2009).

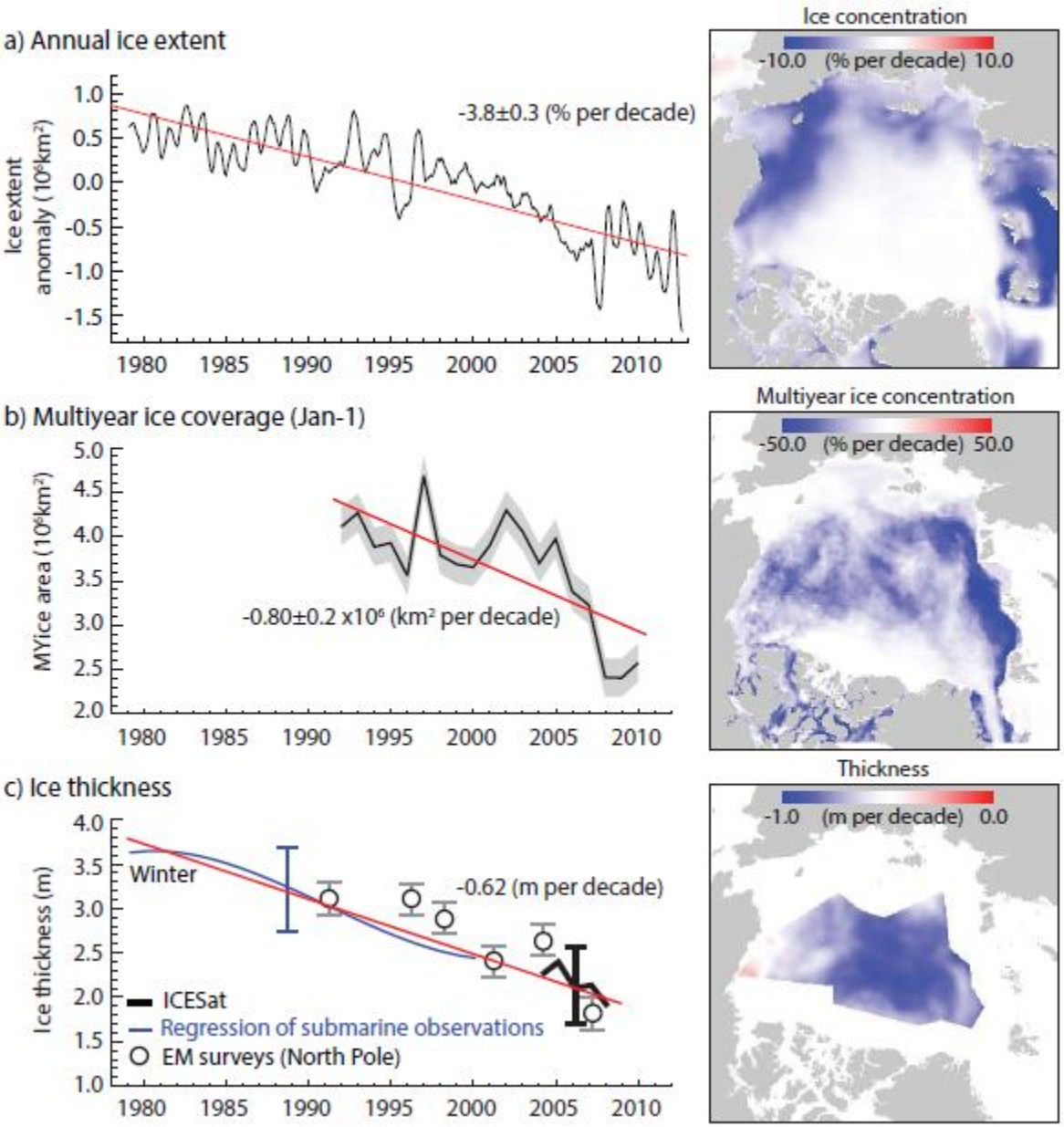
a) Annual ice extent
Ice extent anomaly ($10^6$km$^2$)
1.0
0.5
0.0
-0.5
-1.0
-1.5
1980
1985
1990
1995
2000
2005
2010
-3.8±0.3 (% per decade)
Ice concentration
-10.0 (% per decade) 10.0
b) Multiyear ice coverage (Jan-1)
MYice area ($10^6$km$^2$)
5.0
4.5
4.0
3.5
3.0
2.5
2.0
-0.80±0.2 x$10^6$ (km$^2$ per decade)
Multiyear ice concentration
-50.0 (% per decade) 50.0
c) Ice thickness
Ice thickness (m)
4.0
3.5
3.0
2.5
2.0
1.5
1.0
Winter
-0.62 (m per decade)
ICESat
Regression of submarine observations
EM surveys (North Pole)
Thickness
-1.0 (m per decade) 0.0

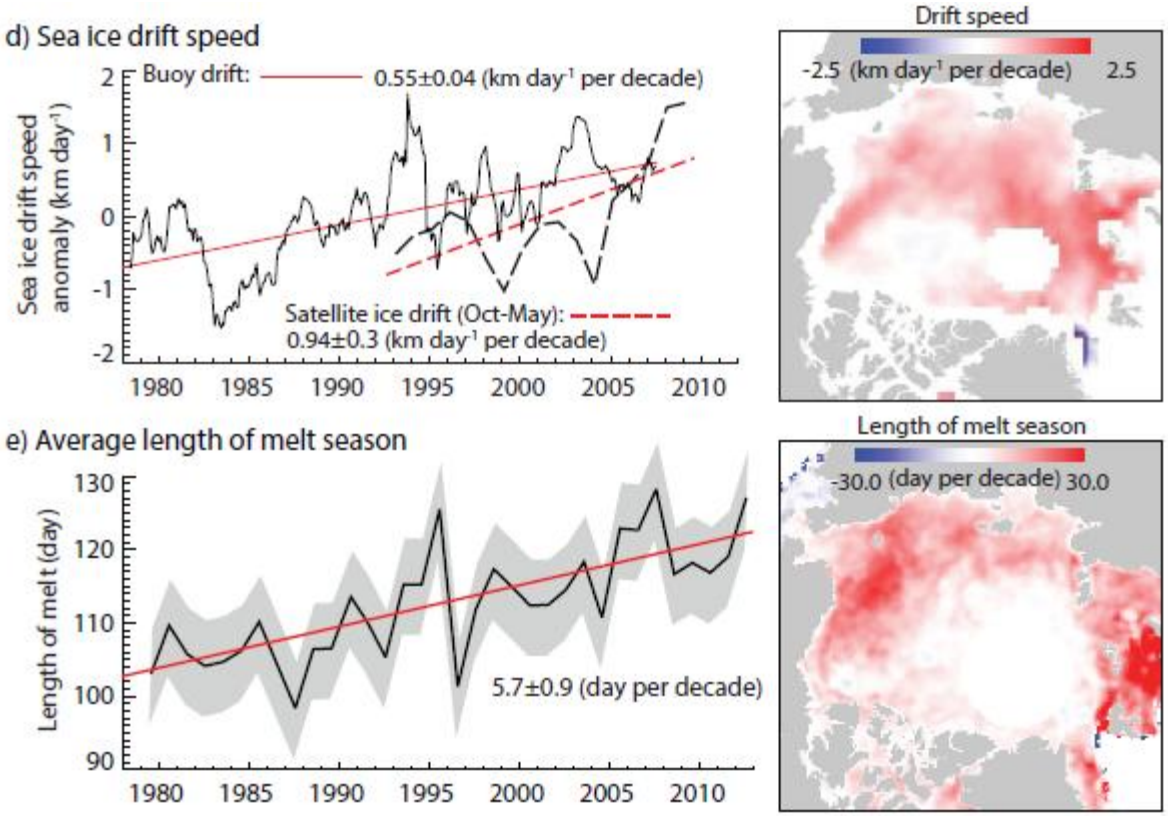


**Figure 4.6 |** Summary of linear decadal trends (red lines) and pattern of changes in the following: (a) Anomalies in Arctic sea ice extent from satellite passive microwave observations (Comiso and Nishio, 2008, updated to include 2012). Uncertainties are discussed in the text. (b) Multi-year sea ice coverage on January 1st from analysis of the QuikSCAT time series (Kwok, 2009); grey band shows uncertainty in the retrieval. (c) Sea ice thickness from submarine (blue), satellites (black) (Kwok and Rothrock, 2009), and *in situ*/electromagnetic (EM) surveys (circles) (Haas et al., 2008); trend in submarine ice thickness is from multiple regression of available observations within the data release area (Rothrock et al., 2008). Error bars show uncertainties in observations. (d) Anomalies in buoy (Rampal et al., 2009) and satellite-derived sea ice drift speed (Spreen et al., 2011). (e) Length of melt season (updated from Markus et al., 2009); grey band shows the basin-wide variability.

# Zmiany w Arktyce - podsumowanie

- The rate of Arctic sea ice extent decrease was very likely between 3.5 and 4.1% per decade (0.45 to 0.51 million km2 per decade). The average decrease in decadal extent of Arctic sea ice has been most rapid in summer and autumn, but the extent has decreased in every season, and in every successive decade since 1979
- The multi-year sea ice extent (summer minimum) decreased between 1979 and 2012 at 11.5 ± 2.1% per decade (0.73 to 1.07 million km2 per decade) (very likely).
- The average winter sea ice thickness within the Arctic Basin decreased between 1980 and 2008 (high confidence). The average decrease was likely between 1.3 and 2.3 m.
- It is likely that the annual period of surface melt on Arctic perennial sea ice lengthened by 5.7 ± 0.9 days per decade over the period 1979–2012

# Zmiany na Antarktydzie

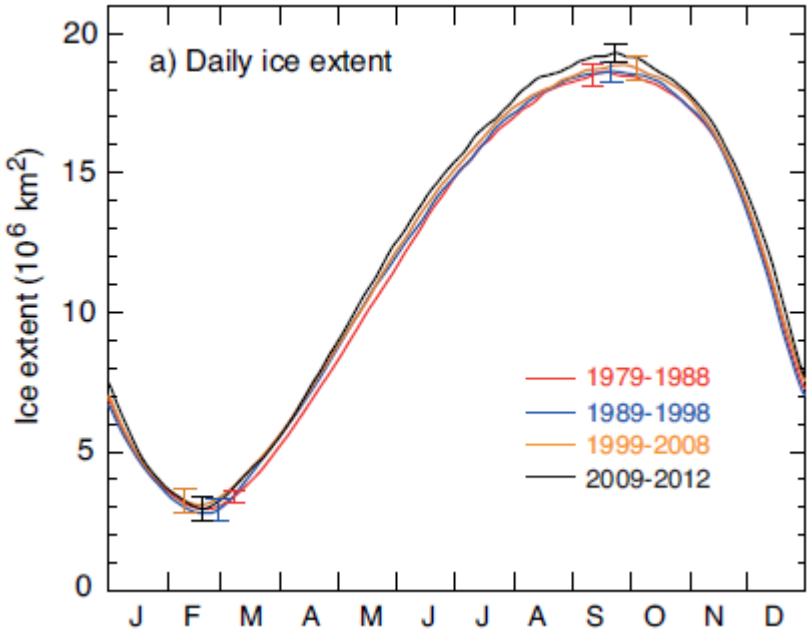


It is very likely that the annual Antarctic sea ice extent increased at a rate of between 1.2 and 1.8% per decade (0.13 to 0.20 million km2 per decade) between 1979 and 2012. There was a greater increase in sea ice area, due to a decrease in the percentage of open water within the ice pack. There is high confidence that there are strong regional differences in this annual rate, with some regions increasing in extent/area and some decreasing

There are large differences in the physical environment and processes that affect the state of Arctic and Antarctic sea ice cover and contribute to their dissimilar responses to climate change. The long, and unbroken, record of satellite observations have provided a clear picture of the decline of the Arctic sea ice cover, but available evidence precludes us from making robust statements about overall changes in Antarctic sea ice and their causes.

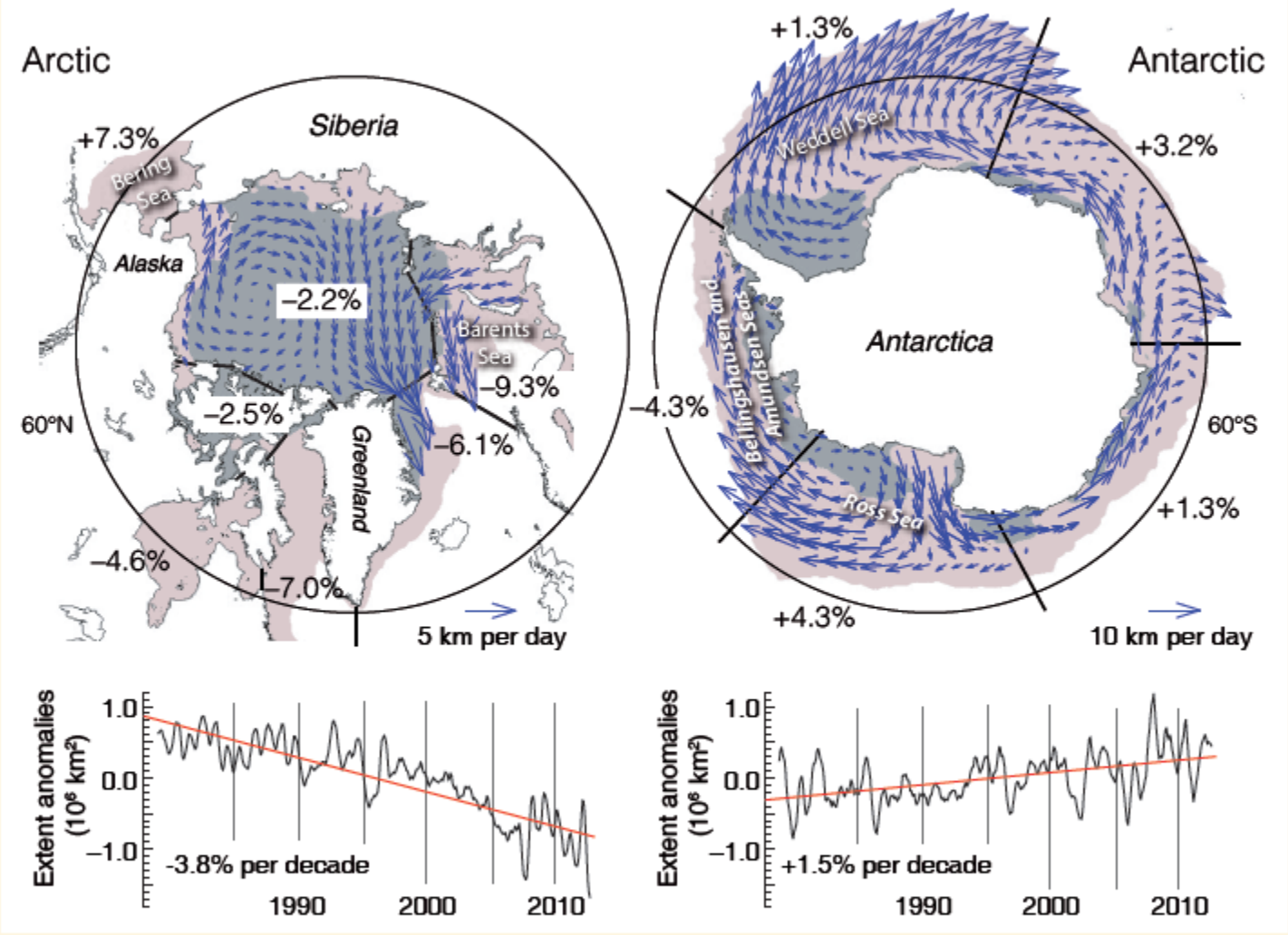


**FAQ 4.1, Figure 1 |** The mean circulation pattern of sea ice and the decadal trends (%) in annual anomalies in ice extent (i.e., after removal of the seasonal cycle), in different sectors of the Arctic and Antarctic. Arrows show the average direction and magnitude of ice drift. The average sea ice cover for the period 1979 through 2012, from satellite observations, at maximum (minimum) extent is shown as orange (grey) shading.

# Lodowce

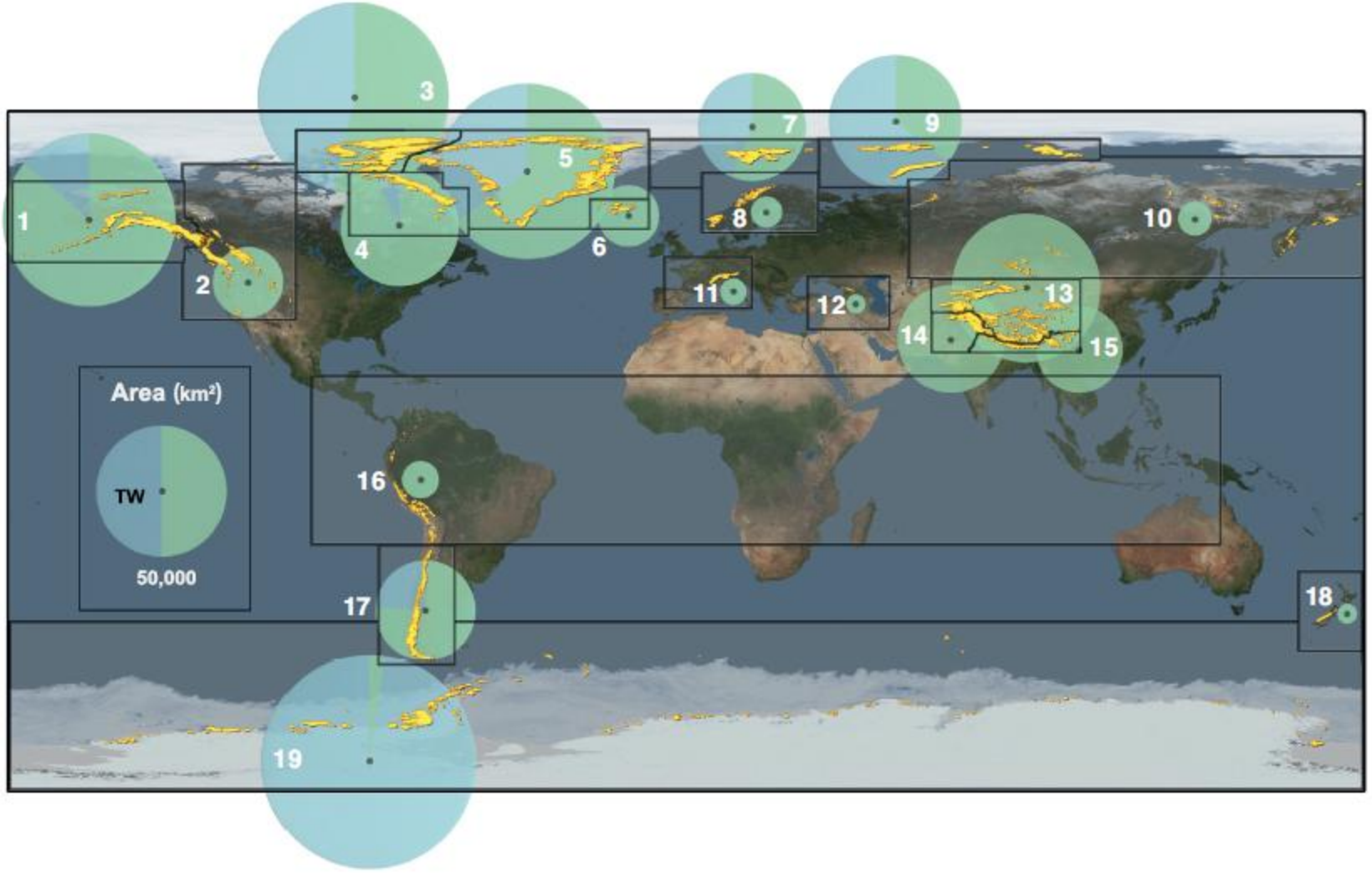


**Figure 4.8 |** Global distribution of glaciers (yellow, area increased for visibility) and area covered (diameter of the circle), sub-divided into the 19 RGI regions (white number) referenced in Table 4.2. The area percentage covered by tidewater (TW) glaciers in each region is shown in blue. Data from Arendt et al. (2012) and Gardner et al. (2013).

**Table 4.2 |** The 19 regions used throughout this chapter and their respective glacier numbers and area (absolute and in percent) are derived from the RGI 2.0 (Arendt et al., 2012); the tidewater fraction is from Gardner et al. (2013). The minimum and maximum values of glacier mass are the minimum and maximum of the estimates given in four studies: Grinsted (2013), Huss and Farinotti (2012), Marzeion et al. (2012) and Radić et al. (2013). The mean sea level equivalent (SLE) of the mean glacier mass is the mean of estimates from the same four studies, using an ocean area of $362.5 \times 10^6$ km$^2$ for conversion. All values were derived with globally consistent methods; deviations from more precise national data sets are thus possible. Ongoing improvements may lead to revisions of these (RGI 2.0) numbers in future releases of the RGI.

| Region | Region Name | Number of Glaciers | Area ( km$^2$) | Percent of total area | Tidewater fraction (%) | Mass (minimum) (Gt) | Mass (maximum) (Gt) | Mean SLE (mm) |
|---|---|---|---|---|---|---|---|---|
| 1 | Alaska | 23,112 | 89,267 | 12.3 | 13.7 | 16,168 | 28,021 | 54.7 |
| 2 | Western Canada and USA | 15,073 | 14,503.5 | 2.0 | 0 | 906 | 1148 | 2.8 |
| 3 | Arctic Canada North | 3318 | 103,990.2 | 14.3 | 46.5 | 22,366 | 37,555 | 84.2 |
| 4 | Arctic Canada South | 7342 | 40,600.7 | 5.6 | 7.3 | 5510 | 8845 | 19.4 |
| 5 | Greenland | 13,880 | 87,125.9 | 12.0 | 34.9 | 10,005 | 17,146 | 38.9 |
| 6 | Iceland | 290 | 10,988.6 | 1.5 | 0 | 2390 | 4640 | 9.8 |
| 7 | Svalbard | 1615 | 33,672.9 | 4.6 | 43.8 | 4821 | 8700 | 19.1 |
| 8 | Scandinavia | 1799 | 2833.7 | 0.4 | 0 | 182 | 290 | 0.6 |
| 9 | Russian Arctic | 331 | 51,160.5 | 7.0 | 64.7 | 11,016 | 21,315 | 41.2 |
| 10 | North Asia[a] | 4403 | 3425.6 | 0.4 | 0 | 109 | 247 | 0.5 |
| 11 | Central Europe | 3920 | 2058.1 | 0.3 | 0 | 109 | 125 | 0.3 |
| 12 | Caucasus | 1339 | 1125.6 | 0.2 | 0 | 61 | 72 | 0.2 |
| 13 | Central Asia | 30,200 | 64,497 | 8.9 | 0 | 4531 | 8591 | 16.7 |
| 14 | South Asia (West) | 22,822 | 33,862 | 4.7 | 0 | 2900 | 3444 | 9.1 |
| 15 | South Asia (East) | 14,006 | 21,803.2 | 3.0 | 0 | 1196 | 1623 | 3.9 |
| 16 | Low Latitudes[a] | 2601 | 2554.7 | 0.6 | 0 | 109 | 218 | 0.5 |
| 17 | Southern Andes[a] | 15,994 | 29,361.2 | 4.5 | 23.8 | 4241 | 6018 | 13.5 |
| 18 | New Zealand | 3012 | 1160.5 | 0.2 | 0 | 71 | 109 | 0.2 |
| 19 | Antarctic and Sub-Antarctic | 3274 | 13,2267.4 | 18.2 | 97.8 | 27,224 | 43,772 | 96.3 |
| | Total | 168,331 | 726,258.3 | | 38.5 | 113,915 | 191,879 | 412.0 |

# Zmiany długości lądowców

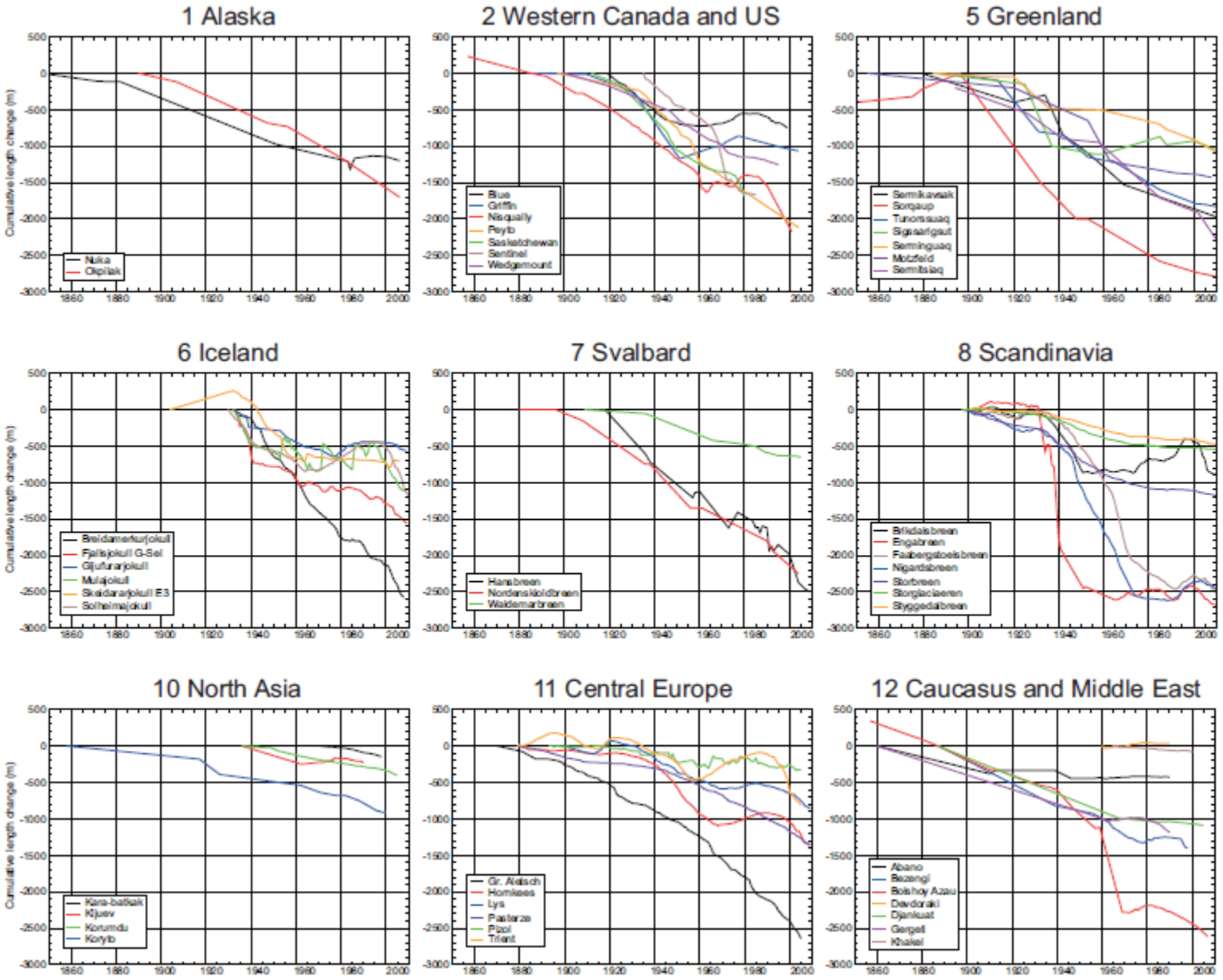

**Table 4.4 |** Regional mass change rates in units of kg $m^{-2}$ $yr^{-1}$ and Gt $y^{-1}$ for the period 2003–2009 from Gardner et al. (2013). Central Asia (region 13), South Asia West (region14), and South Asia East (region 15) are merged into a single region. For the division of regions see Figure 4.8.

| No. | Region Name | (kg $m^{-2}$ $yr^{-1}$) | (Gt $yr^{-1}$) |
|---|---|---|---|
| 1 | Alaska | −570 ± 200 | −50 ± 17 |
| 2 | Western Canada and USA | −930 ± 230 | −14 ± 3 |
| 3 | Arctic Canada North | −310 ± 40 | −33 ± 4 |
| 4 | Arctic Canada South | −660 ± 110 | −27 ± 4 |
| 5 | Greenland periphery | −420 ± 70 | −38 ± 7 |
| 6 | Iceland | −910 ± 150 | −10 ± 2 |
| 7 | Svalbard | −130 ± 60 | −5 ± 2 |
| 8 | Scandinavia | −610 ± 140 | −2 ± 0 |
| 9 | Russian Arctic | −210 ± 80 | −11 ± 4 |
| 10 | North Asia | −630 ± 310 | −2 ± 1 |
| 11 | Central Europe | −1060 ± 170 | −2 ± 0 |
| 12 | Caucasus and Middle East | −900 ± 160 | −1 ± 0 |
| 13–15 | High Mountain Asia | −220 ± 100 | −26 ± 12 |
| 16 | Low Latitudes | −1080 ± 360 | −4 ± 1 |
| 17 | Southern Andes | −990 ± 360 | −29 ± 10 |
| 18 | New Zealand | −320 ± 780 | 0 ± 1 |
| 19 | Antarctic and Sub-Antarctic | −50 ± 70 | −6 ± 10 |
| | **Total** | **−350 ± 40** | **−259 ± 28** |

- Since AR4, almost all glaciers worldwide have continued to shrink as revealed by the time series of measured changes in glacier length, area, volume and mass (very high confidence).
- Between 2003 and 2009, most of the ice lost was from glaciers in Alaska, the Canadian Arctic, the periphery of the Greenland ice sheet, the Southern Andes and the Asian Mountains (very high confidence). Together these regions account for more than 80% of the total ice loss.

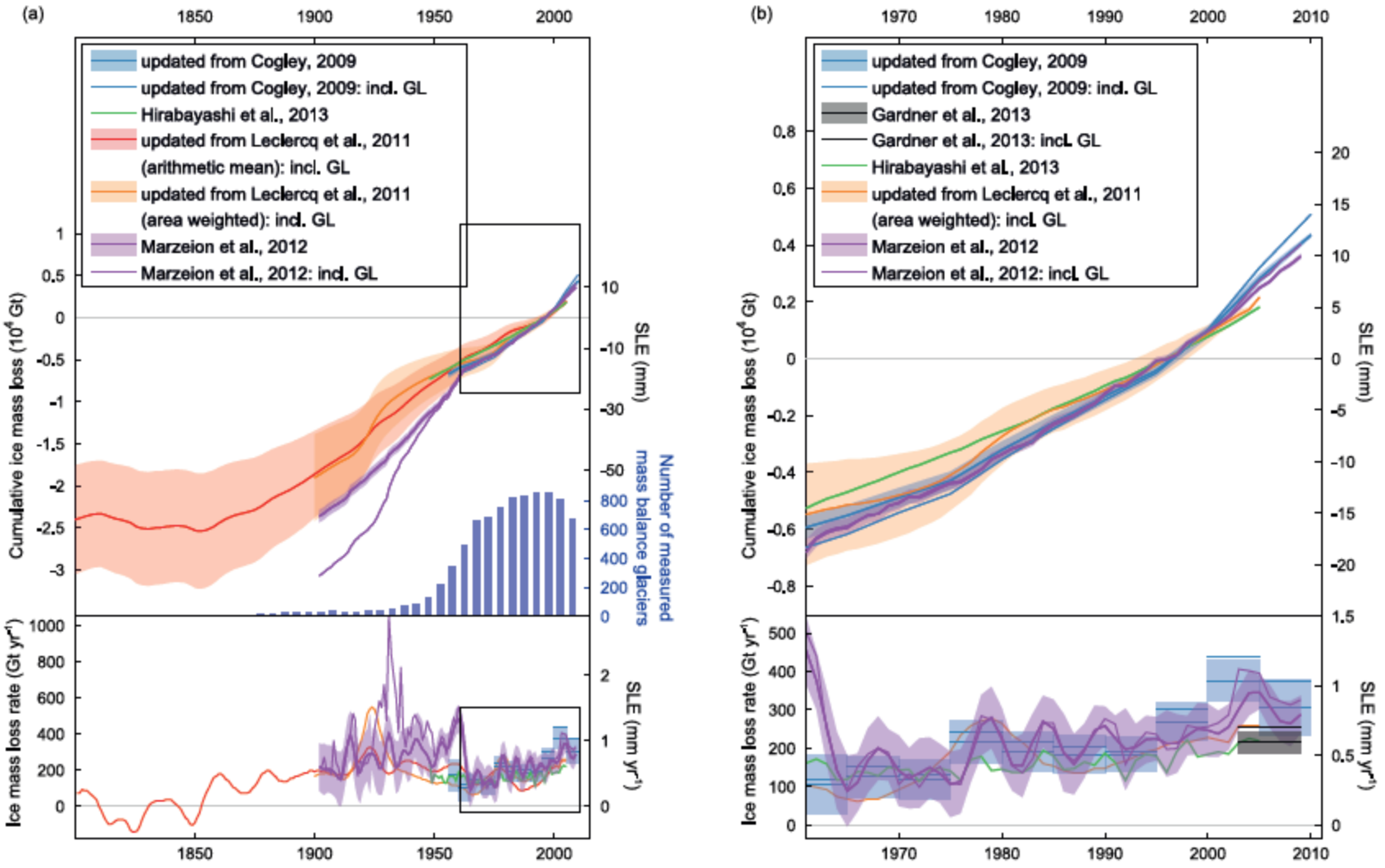


**Figure 4.12 |** Global cumulative (top graphs) and annual (lower graphs) glacier mass change for (a) 1801–2010 and (b) 1961–2010. The cumulative estimates are all set to zero mean over 1986–2005. Estimates are based on glacier length variations (updated from Leclercq et al., 2011), from area-weighted extrapolations of individual directly and geodetically measured glacier mass budgets (updated from Cogley, 2009b), and from modelling with atmospheric variables as input (Marzeion et al., 2012; Hirabayashi et al., 2013). Uncertainties are based on comprehensive error analyses in Cogley (2009b) and Marzeion et al. (2012) and on assumptions about the representativeness of the sampled glaciers in Leclercq et al. (2011). Hirabayashi et al. (2013) give a bulk error estimate only. For clarity in the bottom panels, uncertainties are shown only for the Cogley and Marzeion curves excluding Greenland (GL). The blue bars (a, top) show the number of measured single-glacier mass balances per pentad in the updated Cogley (2009b) time series. The mean 2003–2009 estimate of Gardner et al. (2013) is added to b, bottom.

# Składowe do budżetu masy lodu

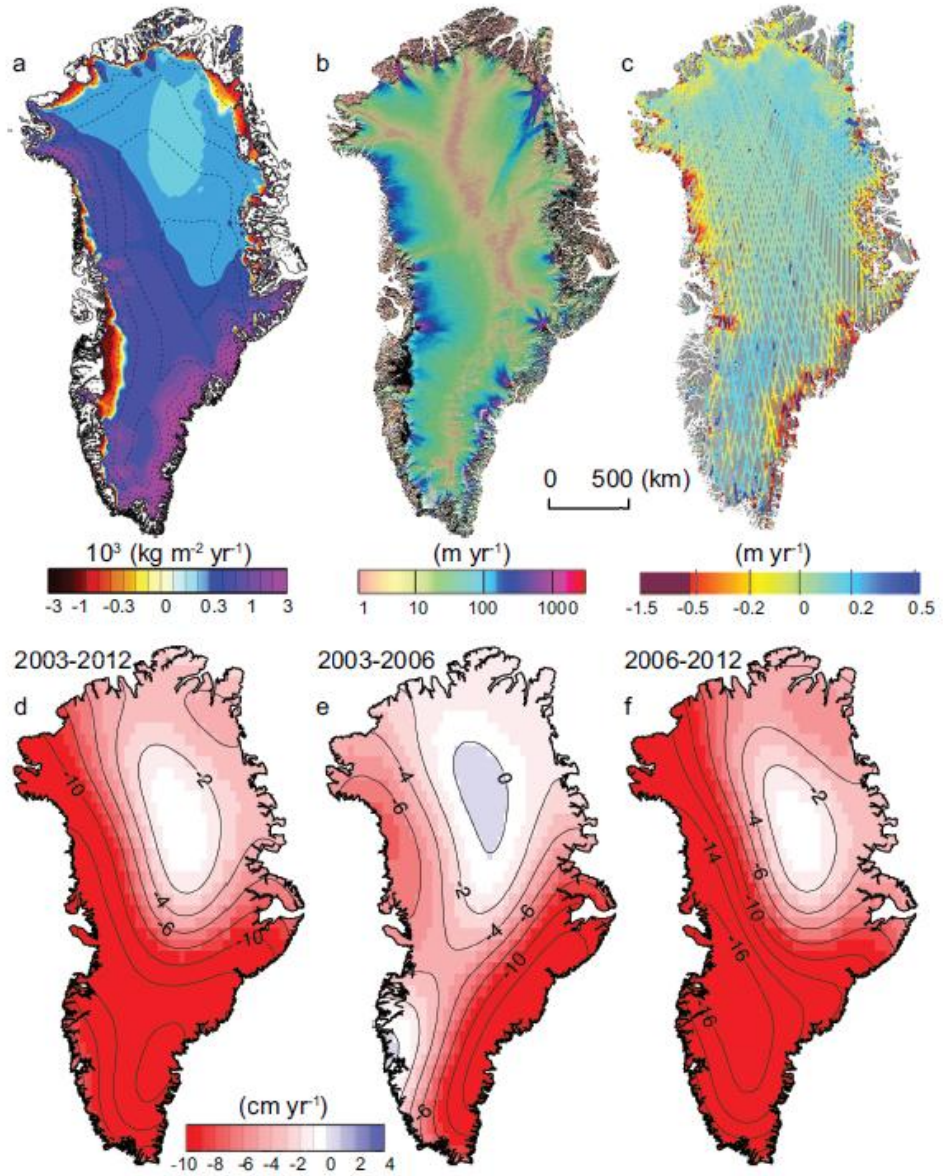


**Figure 4.13 |** Key variable related to the determination of the Greenland ice sheet mass changes. (a) Mean surface mass balance for 1989–2004 from regional atmospheric climate modelling (Ettema et al., 2009). (b) Ice sheet velocity for 2007–2009 determined from satellite data, showing fastest flow in red, fast flow in blue and slower flow in green and yellow (Rignot and Mouginot, 2012). (c) Changes in ice sheet surface elevation for 2003–2008 determined from ICESat altimetry, with elevation decrease in red to increase in blue (Pritchard et al., 2009). (d, e) Temporal evolution of ice loss determined from GRACE time-variable gravity, shown in centimetres of water per year for the periods (a) 2003–2012, (b) 2003–2006 and (c) 2006–2012, colour coded red (loss) to blue (gain) (Velicogna, 2009). Fields shown in (a) and (b) are used together with ice thickness (see Figure 4.18) in the mass budget method.

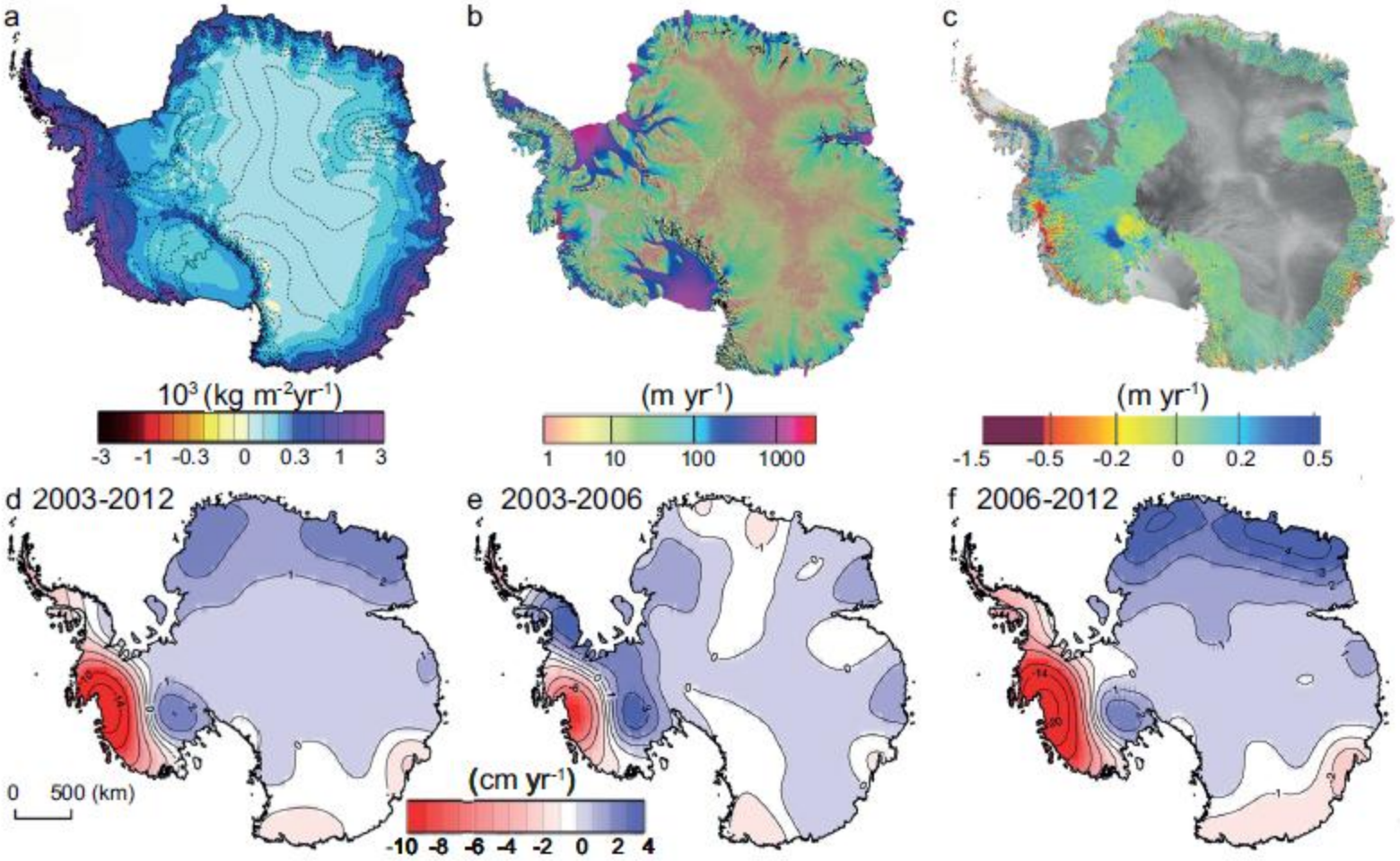


**Figure 4.14 |** Key fields relating to the determination of Antarctica ice sheet mass changes. (a) Mean surface mass balance for 1989–2004 from regional atmospheric climate modelling (van den Broeke et al., 2006). (b) Ice sheet velocity for 2007–2009 determined from satellite data, showing fastest flow in red, fast flow in blue, and slower flow in green and yellow (Rignot et al., 2011a). (c) Changes in ice sheet surface elevation for 2003–2008 determined from ICESat altimetry, with elevation decrease in red to increase in blue (Pritchard et al., 2009). (d, e) Temporal evolution of ice loss determined from GRACE time-variable gravity, shown in centimetres of water per year for the periods (a) 2003–2012, (b) 2003–2006 and (c) 2006–2012, colour coded red (loss) to blue (gain) (Velicogna, 2009). Fields shown in (a) and (b) are used together with ice thickness (see Figure 4.18) in the mass budget method.

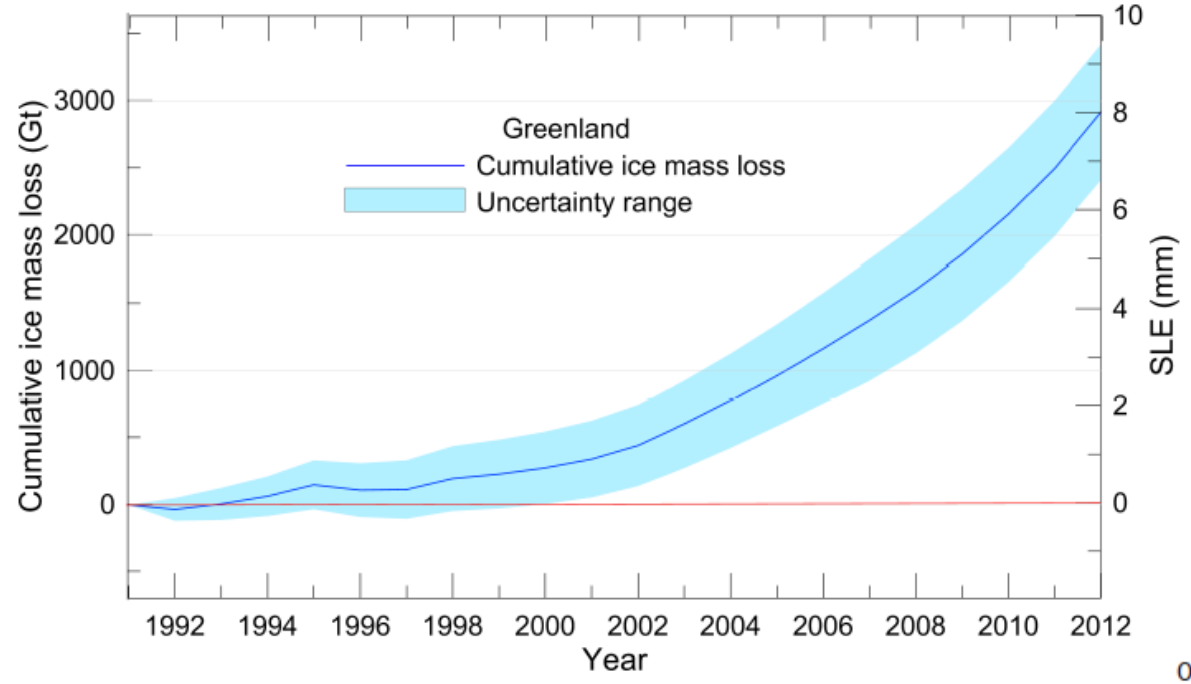


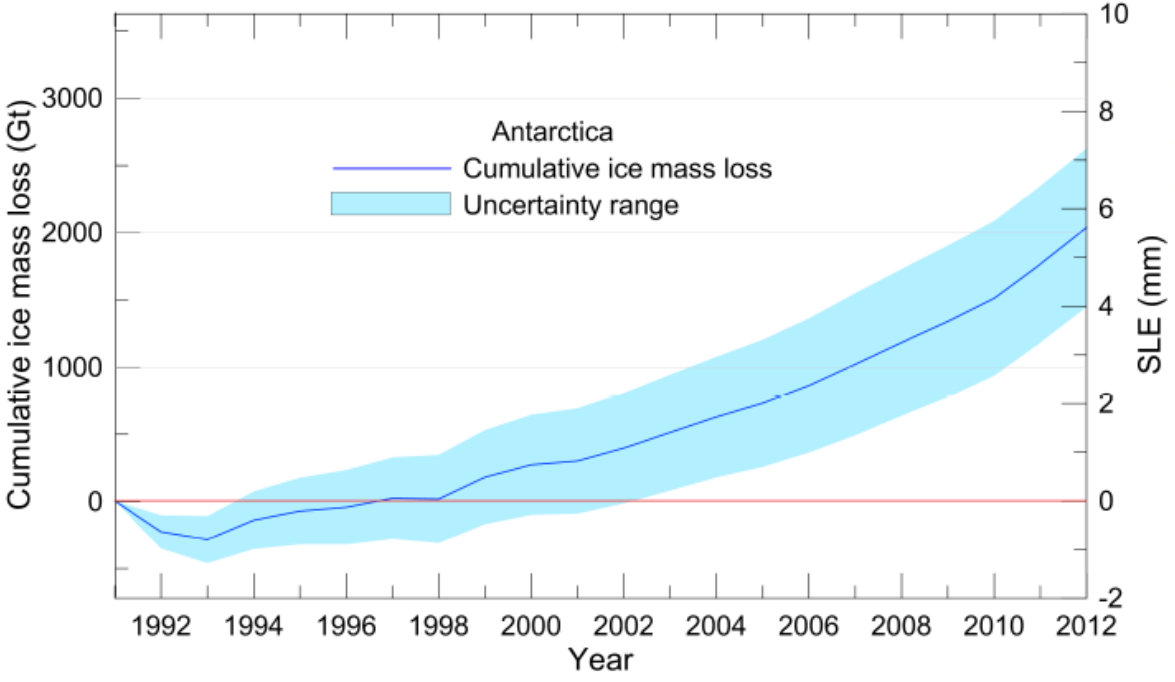


Overall, there is *high confidence* that the Antarctic ice sheet is currently losing mass. The average ice mass change to Antarctica from the present assessment has been –97 [–135 to –58] Gt $yr^{-1}$ (a sea level equivalent of 0.27 mm $yr^{-1}$ [0.37 to 0.16] mm $yr^{-1}$) over the period 1993–2010, and –147 [–221 to –74] Gt $yr^{-1}$ (0.41 [0.61 to 0.20] mm $yr^{-1}$) over the period 2005–2010. These assessments include the Antarctic peripheral glaciers.

# Porywa lodowa

- The rate of ice loss from the Greenland ice sheet has accelerated since 1992. The average rate has very likely increased from 34 [–6 to 74] Gt yr–1 over the period 1992–2001 (sea level equivalent, 0.09 [–0.02 to 0.20] mm yr–1), to 215 [157 to 274] Gt yr–1 over the period 2002–2011 (0.59 [0.43 to 0.76] mm yr–1).
- The Antarctic ice sheet has been losing ice during the last two decades (high confidence). There is very high confidence that these losses are mainly from the northern Antarctic Peninsula and the Amundsen Sea sector of West Antarctica, and high confidence that they result from the acceleration of outlet glaciers.
- The average rate of ice loss from Antarctica likely increased from 30 [–37 to 97] Gt yr–1 (sea level equivalent, 0.08 [–0.10 to 0.27] mm yr–1) over the period 1992–2001, to 147 [72 to 221] Gt yr–1 over the period 2002–2011 (0.40 [0.20 to 0.61] mm yr–1).

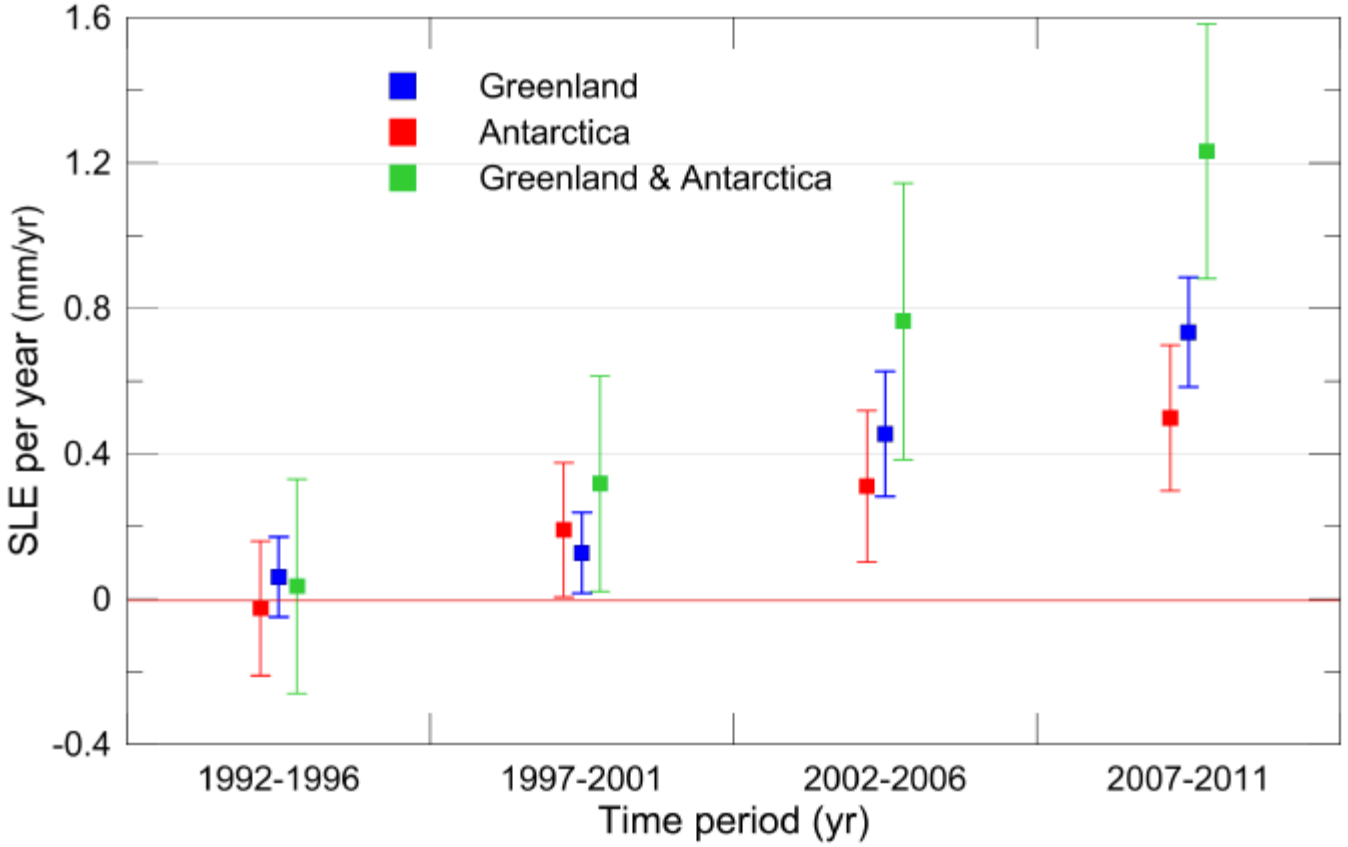


**Figure 4.17 |** Rate of ice sheet loss in sea level equivalent averaged over 5-year periods between 1992 and 2011. These estimates are derived from the data in Figures 4.15 and 4.16.

# Zmiany głębokości zamarzania gruntu

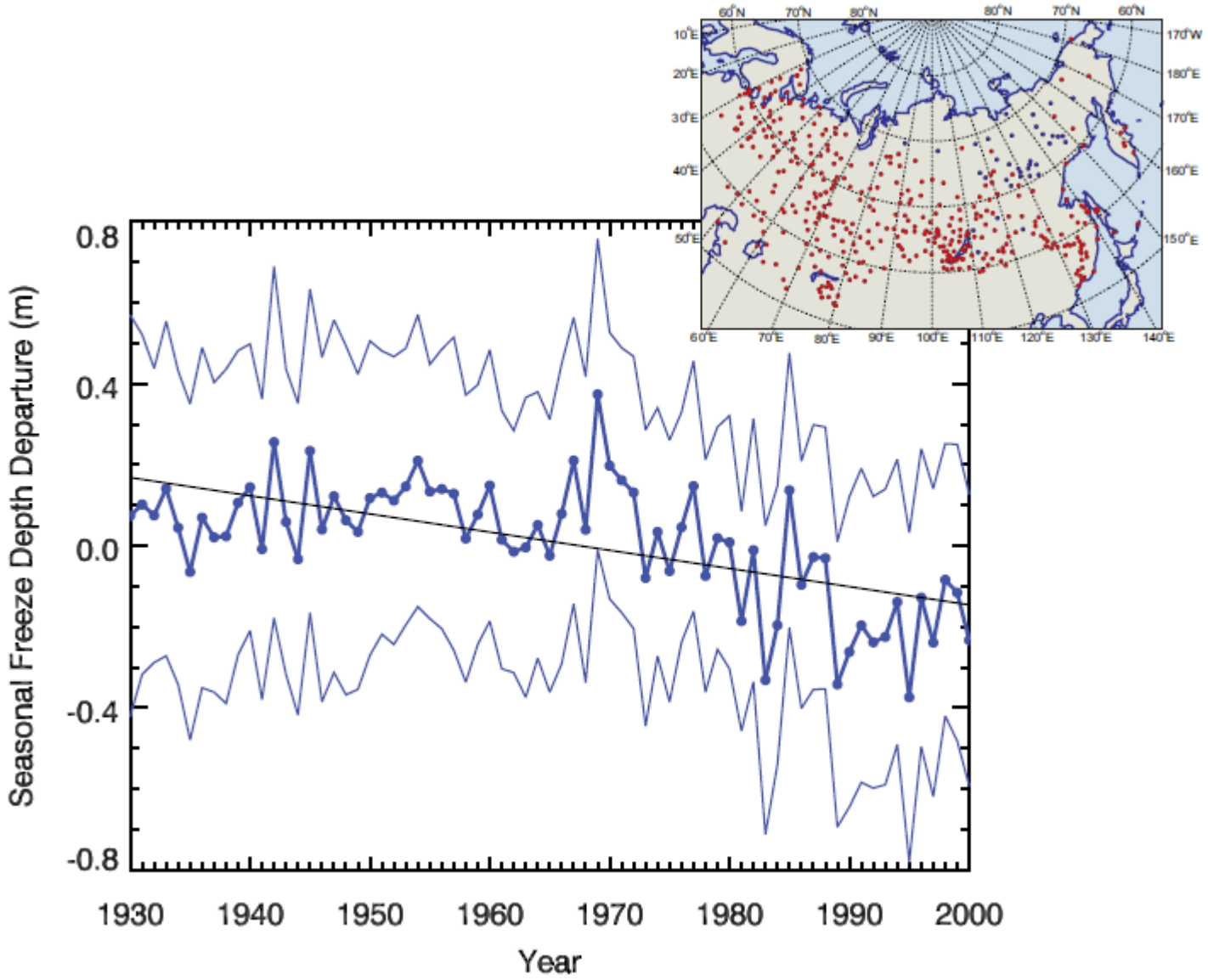

# Pokrywa śnieżna

- Snow cover extent has decreased in the Northern Hemisphere, especially in spring (very high confidence). Satellite records indicate that over the period 1967–2012, annual mean snow cover extent decreased with statistical significance; the largest change, –53% [very likely, –40% to –66%], occurred in June. No months had statistically significant increases. Over the longer period, 1922–2012, data are available only for March and April, but these show a 7% [very likely, 4.5% to 9.5%] decline and a strong negative [–0.76] correlation with March–April 40°N to 60°N land temperature.

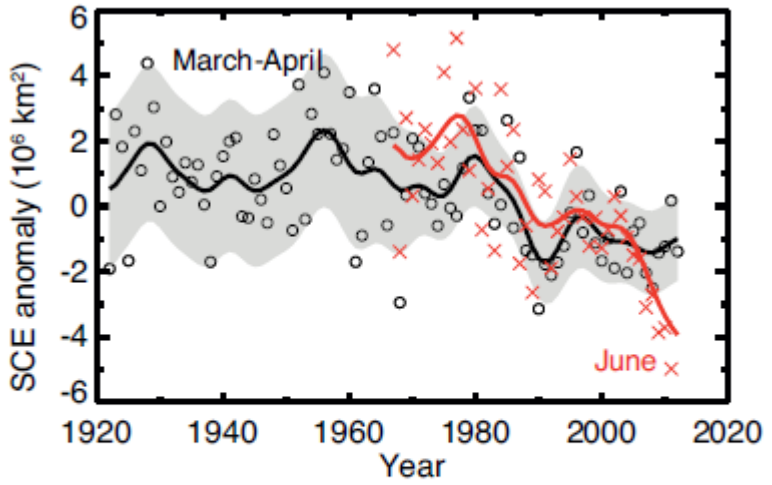


**Figure 4.19** | March–April NH snow cover extent (SCE, circles) over the period of available data, filtered with a 13-term smoother and with shading indicating the 95% confidence interval; and June SCE (red crosses, from satellite data alone), also filtered with a 13-term smoother. The width of the smoothed 95% confidence interval is influenced by the interannual variability in SCE. Updated from Brown and Robinson (2011). For both time series the anomalies are calculated relative to the 1971–2000 mean.

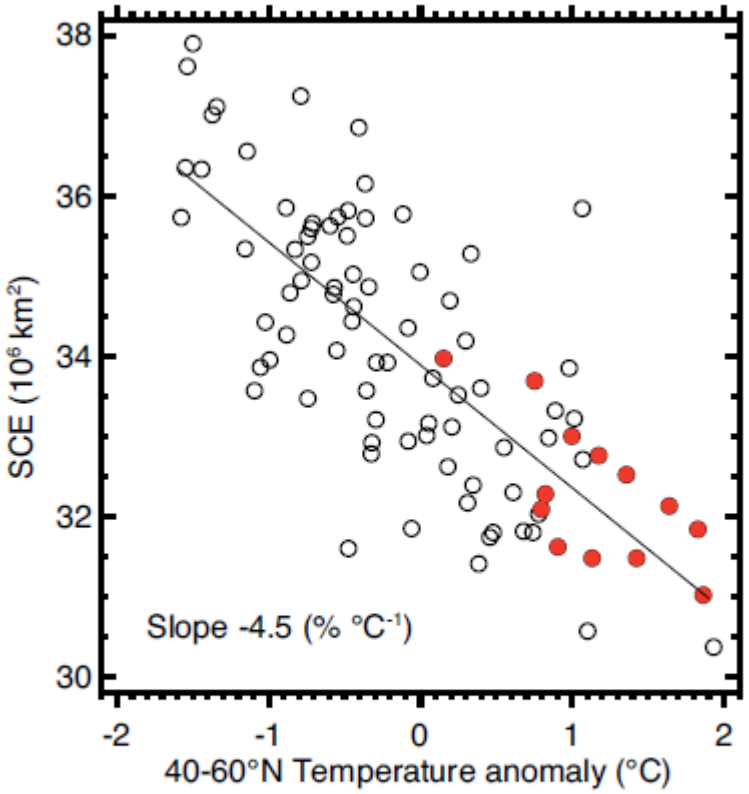


**Figure 4.20 |** Relationship between NH April SCE and corresponding land air temperature anomalies over 40°N to 60°N from the CRUtem4 data set (Jones et al., 2012). Red circles indicate the years 2000–2012. The correlation is 0.76. Updated from Brown and Robinson (2011).

**Table 4.7 |** Least-squares linear trend in Northern Hemisphere snow cover extent (SCE) in $10^6$ km$^2$ per decade for 1967–2012. The equivalent trends for 1922–2012 (available only for March and April) are –0.19* March and –0.40* April.

| Annual | Jan | Feb | March | April | May | June | July | Aug | Sep | Oct | Nov | Dec |
|---|---|---|---|---|---|---|---|---|---|---|---|---|
| –0.40* | 0.03 | –0.13 | –0.50* | –0.63* | –0.90* | –1.31* | n/a | n/a | n/a | n/a | 0.17 | 0.34 |

Notes:
*Denotes statistical significance at $p = 0.05$.

# Changes in the Cryosphere

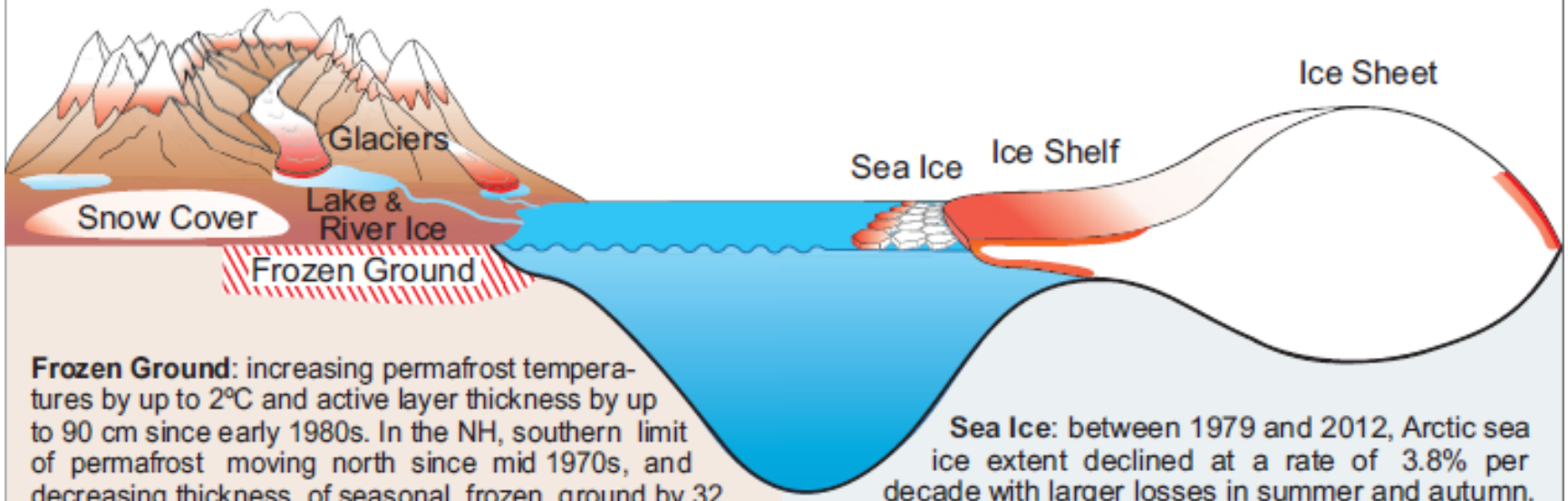


**Frozen Ground**: increasing permafrost temperatures by up to 2ºC and active layer thickness by up to 90 cm since early 1980s. In the NH, southern limit of permafrost moving north since mid 1970s, and decreasing thickness of seasonal frozen ground by 32 cm since 1930s.

**Snow cover**: between 1967 and 2012, satellite data show decreases through the year, with largest decreases (53%) in June. Most stations report decreases in now especially in spring.

**Lake and river ice**: contracting winter ice duration with delays in autumn freeze-up proceeding more slowly than advances in spring break-up, with evidence of recent acceleration in both across the NH.

**Glaciers**: are major contributors to sea level rise. Ice mass loss from glaciers has increased since the 1960s. Loss rates from glaciers outside Greenland and Antarctica were 0.76 mm $yr^{-1}$ SLE during the 1993 to 2009 period and 0.83 mm $yr^{-1}$ SLE over the 2005 to 2009 period.

**Sea Ice**: between 1979 and 2012, Arctic sea ice extent declined at a rate of 3.8% per decade with larger losses in summer and autumn. Over the same period, the extent of thick multiyear ice in the Arctic declined at a higher rate of 13.5% per decade. Mean sea ice thickness decreased by 1.3 - 2.3 m between 1980 and 2008.

**Ice Shelves and ice tongues**: continuing retreat and collapse of ice shelves along the Antarctic Peninsula. Progressive thinning of some other ice shelves/ice tongues in Antarctica and Greenland.

**Ice Sheets**: both Greenland and Antarctic ice sheets lost mass and contributed to sea level change over the last 20 years. Rate of total loss and discharge from a number of major outlet glaciers in Antarctica and Greenland increased over this period.

# Wpływ zmian w kriosferze na poziom oceanu